University of Modena and Reggio Emilia

Department of Engineering Enzo Ferrari

PhD Course in
Information and Communication Technologies

High Dynamic Full Digital Control of IPM Motors Based on Magnetic Models

First thesis supervisor:
Prof. Giovanni Franceschini

Candidate:
Matteo Frigieri

PHD course supervisor:
Prof. Luigi Rovati

Academic Year 2022/2023

Abstract

New power devices, like wide band gap SiC and GaN Mosfets can bring conversion efficiency to higher levels. Their use in topologies like the Current Source Inverter (CSI) in fields like grid connected power conversion, Electric Vehicles traction and other motor control applications can potentially overcome the factors that limited the adoption of this architecture [1]. One key benefit is the reduction of iron losses in permanent magnet synchronous motors, which are dependent on ripple current. The CSI topology can mitigate this ripple compared to traditional VSI (Voltage Source Inverter) systems. Wide bandgap VSIs also achieve high conversion efficiency due to the very fast turn-on and turn-off speeds of the power devices. However, the resulting high dv/dt can induce significant stress on motor windings, potentially leading to insulation failure, and can also impact the motor's ball bearings. Moreover, VSIs are voltage-limited, necessitating motor control in MTPV (Maximum Torque Per Voltage) mode. MTPV is a challenging operational curve to follow due to its inherent nonlinearities, as discussed in the following work. Thanks to its intrinsic boost capability, the CSI can bypass the need for MTPV, allowing for greater utilization of the inverter's kVA rating.

Chapter 1 presents a comprehensive comparison of Current Source Inverters (CSIs) and Voltage Source Inverters (VSIs) for power conversion applications. The focus is on the innovative CSI7 topology, which offers improved efficiency and performance compared to traditional CSIs. The study provides a detailed analysis of the CSI7 topology, including its operating principles, advantages, and limitations. A comparison with VSIs is conducted, considering factors such as efficiency, reliability, and control complexity. Simulation and experimental results demonstrate the superior efficiency of the CSI7 topology, particularly in high-power applications. The innovative architecture reduces conduction losses and improves the overall performance of the converter. The chapter also discusses the challenges and considerations associated with implementing CSI7 topologies, such as the need for careful thermal management and control strategies. Overall, the findings presented in this paper highlight the potential benefits of CSI7 technology for various power conversion applications, offering a promising alternative to traditional VSI architectures.

Chapter 2 presents a comprehensive analysis of Current Source Inverter (CSI) topologies for photovoltaic (PV) grid-connected systems. The focus is on the innovative CSI7 topology, which offers several advantages over traditional CSI and Voltage Source Inverter (VSI) architectures.

The chapter provides a detailed comparison of CSI and VSI topologies, highlighting the unique characteristics and benefits of CSIs in PV applications. The CSI7 topology is presented, including its operating principles, advantages, and limitations. Simulation and experimental results demonstrate the superior performance of the CSI7 topology in terms of efficiency, power density, and grid integration capabilities. The proposed topology offers a promising solution for addressing the challenges associated with traditional PV inverter architectures, such as high-voltage operation, reduced component count, and improved reliability. The study also discusses the potential applications of CSI7 topologies in various PV system configurations, including modular systems and large-scale installations. Overall, the findings presented in this paper highlight the promising future of CSI technology for enhancing the efficiency and cost-effectiveness of PV power generation.

Chapter 3 presents a comprehensive analysis of the importance of accurate machine modeling for the development of optimal control strategies for Interior Permanent Magnet (IPM) synchronous machines. The focus is on incorporating nonlinear magnetic effects, such as saturation, into the machine model to improve the accuracy of control trajectory predictions. The chapter reviews existing approaches for modeling IPM machines, highlighting the limitations of linear models and the benefits of nonlinear models. A new approach based on Finite Element Analysis (FEA) is proposed to generate accurate maps of equivalent inductances, capturing the nonlinear magnetic behavior of the machine. Two different methods were adopted to model the magnetic nonlinearities and obtain equivalent inductances' maps: a standard magnetostatic method and Frozen Permeability (FP) method. Then, the two methods were compared in terms of control trajectories, Voltage Limit Ellipses (VLE) and Constant Torque Hyperbolas (CTH) also with the ones obtained from 2-D FEA FEMM (via the Maxwell's stress tensor). The proposed model was validated numerically and good results were obtained, especially for the FP method.

Chapter 4 presents a comprehensive analysis of flux-weakening control strategies for Internal Permanent Magnet (IPM) machines in electric vehicle applications. IPM machines are widely used due to their high torque density, efficiency, and flux-weakening capability. Flux-weakening is essential for operating in a wide speed range beyond the constant torque region. The work discusses the challenges associated with achieving optimal flux-weakening control, particularly during fast torque transitions and braking. Existing control strategies often struggle to maintain stable operation and prevent undesirable torque generation during these events. This research proposes improved flux-weakening control algorithms that address these limitations. By incorporating feed-forward actions and anti-wind-up techniques, the proposed methods enhance the robustness and performance of the system, ensuring smooth transitions and controlled braking behavior. Experimental results validate the effectiveness of the proposed strategies, demonstrating significant improvements in torque generation, efficiency, and overall system performance. The optimized control algorithms provide a valuable solution for achieving optimal flux-weakening control in IPM machines for electric vehicles.

Chapter 5 presents a comprehensive comparison of Interior Permanent Magnet (IPM) synchronous machines driven by Voltage Source Inverters (VSIs) and Current Source Inverters (CSIs). The focus is on high-speed applications requiring flux-weakening control. In this chapter a new extended Maximum Torque per Ampere (MTPA)-flux-weakening control strategy for CSIs, enabling improved performance and efficiency. A detailed model of the IPM machine, including its parameters and geometry, is established. The performance of both VSI and CSI configurations is evaluated under various operating conditions, considering factors such as torque, speed, and efficiency. The results demonstrate that CSIs offer several advantages, including higher torque, wider speed range, and reduced current ripple. The proposed extended MTPA-flux-weakening control strategy for CSIs further enhances their performance, particularly in high-speed regions. Overall, the paper provides valuable insights into the comparative performance of VSIs and CSIs for IPM machines, highlighting the potential benefits of CSI technology in high-performance electric vehicle applications.

Contents

List of Figures

List of Tables

1. Current Source Inverter

The inverter is a static DC-AC converter. Multiple inverter's topologies are currently used in the static conversion field. In this chapter the Current Source Inverter topology (CSI) will be presented with its main advantages and drawbacks with respect to the more traditional Voltage Source Inverter (VSI). VSIs are widely used because of their high efficiency and simplicity.

1.1 CSI topology

The Current Source Inverter (CSI), unlike the more traditional Voltage Source Inverter (VSI), uses an inductor as a component to decouple the input and the output power. The CSI converter needs the inductor to store magnetic energy and obtain, ideally, a constant current source in steady state conditions. This current source must be commuted properly on the three phases of the output stage, in fact the functioning of the converter is based on the current which goes through it.

In this case the condition which is forbidden for the VSI, is a normal operating condition: the leg short circuit is necessary to store power in the inductor. Addressing the current to the load, the energy stored in the inductor is reduced (which means that the current is reduced), so the leg short circuit condition is necessary to increment again the current.

The Insulated Gate Bipolar Transistor (IGBT) presents in an unique device the advantages of MOS, namely the high switching speed and the high input impedance, and BJT, so the low saturation voltage. Nevertheless, their drawback is that they do not tolerate high voltage in reverse, which in this architecture must be taken into account because they will be subjected to this condition periodically. For this reason, power diodes must be introduced in series to IGBT, with the purpose of tolerate the reverse voltage, as shown in Fig. 1 where the traditional architecture of a CSI is represented.

In most cases, storing energy in an inductor poses a higher risk compared to a capacitor, as a continuous loop is required for the current to flow through it. This means that also for the CSI there are some forbidden configurations, that are the ones in which all the devices high or

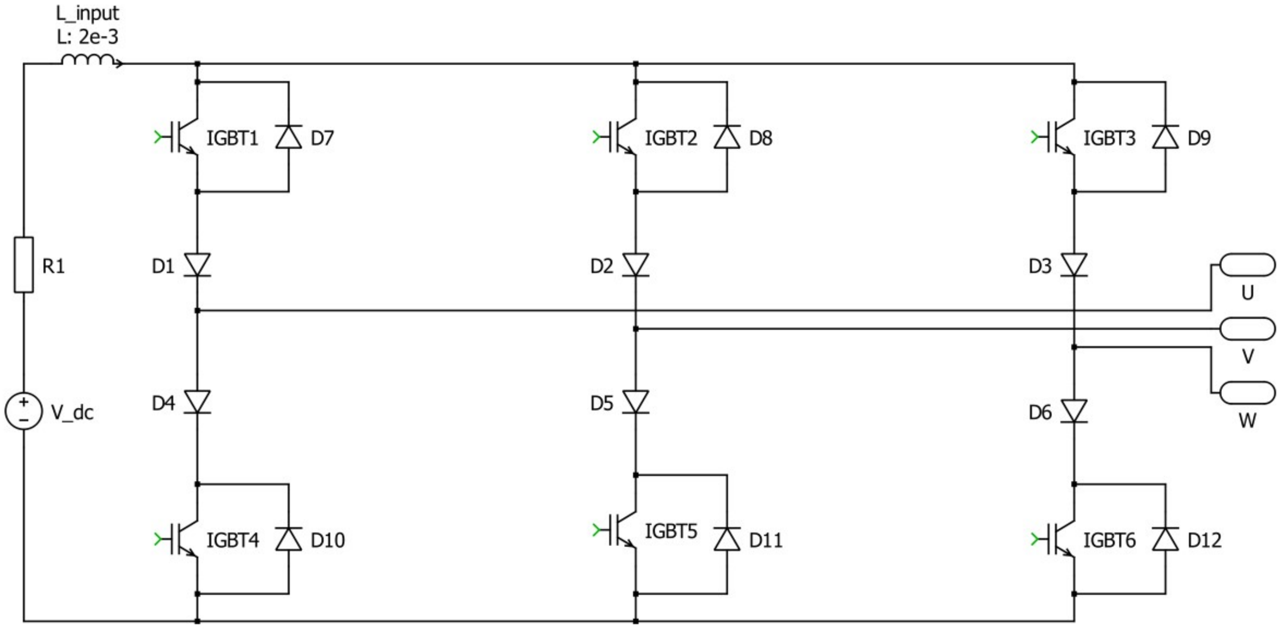

Figure 1: Traditional CSI architecture.

low of the bridge are off; otherwise, the inductor would generate a high over voltage that could break the devices.

Nevertheless, the inductor energy storage has an important advantage since this converter has intrinsecally the capability to boost in voltage; this is possible because the inductor generates the voltage needed to grant the continuity of the current. So, after the charging period with the leg short circuit when the couple of the turned on devices is changed and the current is directed to the load, an over voltage is generated, allowing the current keeping flowing through the new loop, which is characterized by an higher impedance with respect to the previous one. The working cycle and the architecture reminds the ones of the boost converter shown in Fig. 2.

1.2 Comparison between CSI and VSI

After the description of the topology and the main working principles of the CSI, hereafter a comparison with the more traditional VSI topology is proposed. The VSI is considered connected in series with a boost converter (BC+VSI), in order to introduce the possibility to boost in voltage also for the VSI. The series boost converter and VSI is represented in Fig. 3.

- Even if the BC+VSI is obtained from the series of two converters, the overall efficiency is still better than the one of the CSI in the majority of the working conditions [2]. This

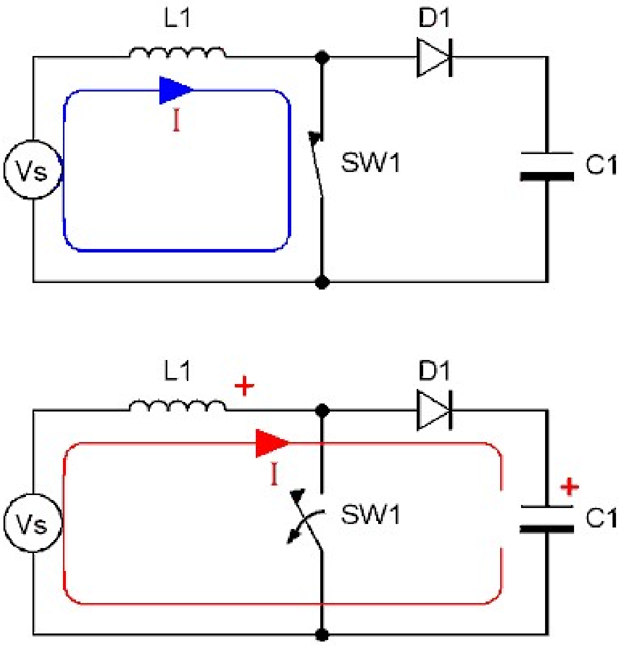

Figure 2: Electrical and operating scheme of the boost converter.

happens because the conduction losses generated by the series of four devices (two IGBTs and two diodes) are very high. An improvement of the CSI efficiency could be obtained with IGBT devices which support reverse voltage (Reverse Blocking IGBT) and capable of switching at high frequency.

- The CSI is more resilient than the VSI. In fact the electrolytic capacitor of the VSI is the most fragile device, since it is composed by a liquid electrolyte which has a limited life time. Furthermore, this component cannot handle with high temperature, easily reachable in some environments as photovoltaic or industrial applications. Additional

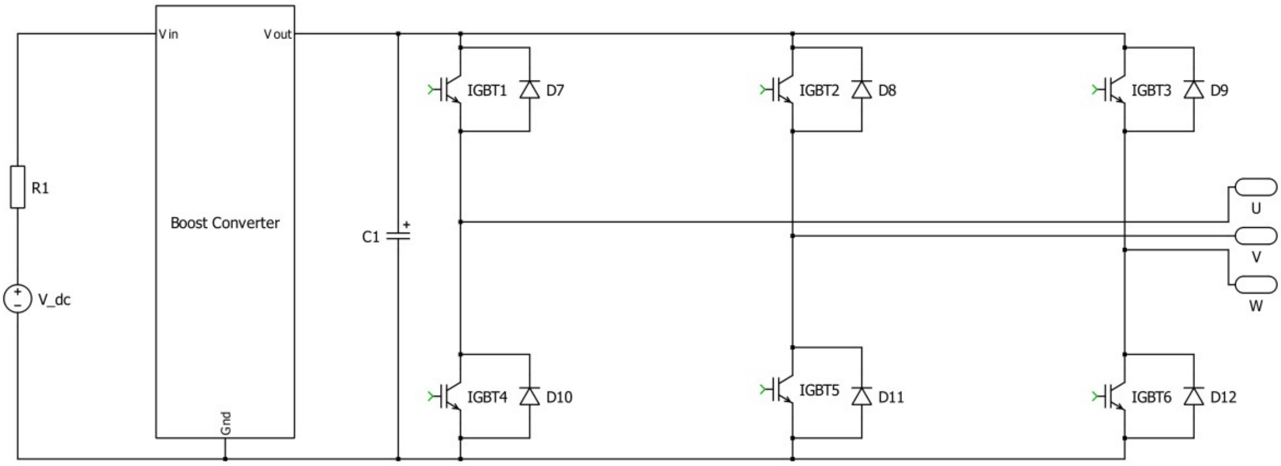

Figure 3: Electrical scheme of the BC+VSI.

heat is generated from the current flowing on the internal series resistance, causing an additional temperature increase. On the other side, the inductor used for the CSI is much more robust both electrically and mechanically.

- Considering the control of electrical machines in flux weakening conditions, if a fault occurs, the anti-parallel diodes connected to the IGBTs of the VSI would work as an uncontrolled rectifier bridge and could generate over voltages not tolerable from the bus capacitors or power devices. Furthermore, they could not be able to let such high currents to flow, causing the destruction of the devices. The CSI is way more reliable and, considering that the parallel- connected diodes have been sized correctly, they should sustain the reverse voltages imposed by the load [3].
- One of the main drawbacks of the VSI topology is the high dv/dt that comes from the pulse width modulated (PWM) output voltages, which can cause motor insulation degradation, bearing failure and unacceptable electromagnetic interference effects upon the control circuits and acoustic noise. The CSI allows reducing the output voltages dv/dt and therefore the stress on the insulation [4].

1.3 CSI7

The main drawback of the CSI is the lower efficiency with respect to the VSI. So, an innovative topology proposal was made with the purpose of reducing the losses of the converter [5], [6]. Section 1.1 highlighted that during the modulation the CSI requires leg short circuit to grant the continuity of the current flow through the inductor(this time interval will be called T_{off}).

Referring to Fig. 4, during T_{off} the current can flow through IGBT1, D1, D4, IGBT4 and the total voltage drop on the four devices is obtained according to

$$V_{drop} = 2V_{CE_{sat}} + 2V_{\gamma} \tag{1.1}$$

Where $V_{CE_{sat}}$ is the voltage drop on the single IGBT and V_{γ} is the voltage drop on the single diode. Assuming that the current is constant, which is coherent if the input inductance is high and the switching frequency is high, the instant power dissipated on these four devices is given by

$$P = I\left(2V_{CE\_sat} + 2V_{\gamma}\right) \tag{1.2}$$

This is true if the time slot considered is not a transient between two different modulation coefficients. During this time slot the power generated is not transferred to the load but stored in the inductor; so, a more efficient method to obtain less losses could be adopted. Here is why an additional controlled switch was introduced in the converter; with the additional IGBT in the additional leg, a loop with a minor voltage drop is introduced during the T_{off}, so the energy stored in the inductor is maximized. In Fig. 4 the electrical scheme with the modified architecture is represented.

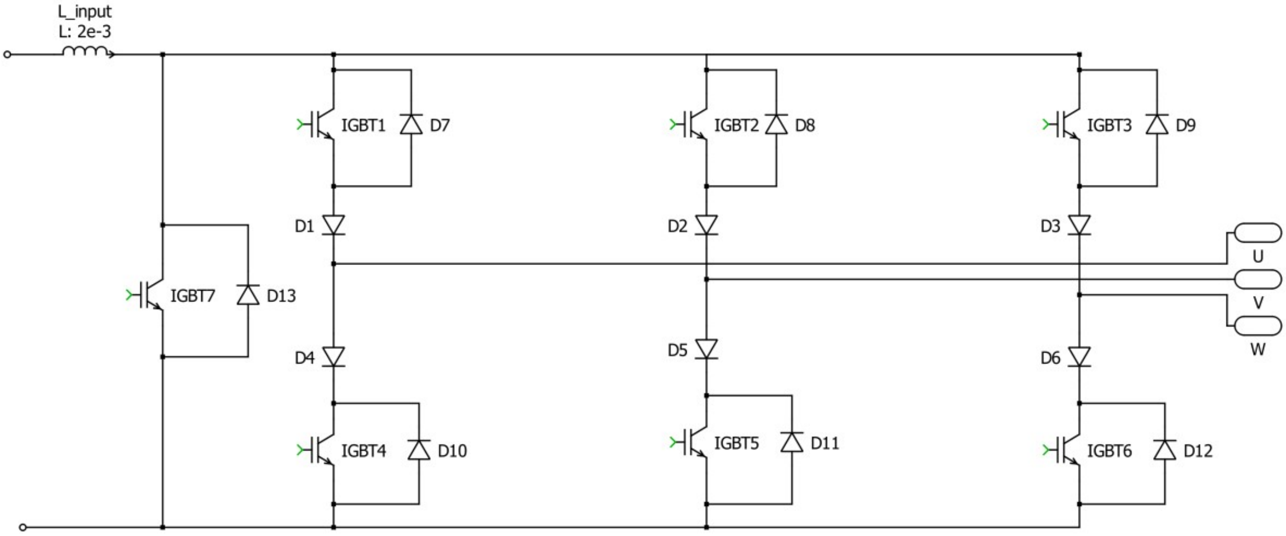

Figure 4: Electrical scheme of the CSI7.

With the proposed topology, the conduction losses during the leg short circuits are much lower than the ones obtained with the traditional architecture, in fact the voltage drop is now reduced to $V_{CE_{sat}}$, so the dissipated power is

$$P = IV_{CE\_sat} \tag{1.3}$$

Obviously this is just a portion of the total dissipated power, but it helps to improve the overall efficiency, which is the main weakness of the CSI.

The main advantages of the proposed innovative topology are listed below.

- The higher efficiency of the new configuration , which becomes more and more important when the boost action is more intense. This happens because to increment the output voltage an higher amout of time during the PWM period must be spent in leg short circuit condition, in order to store more energy into the inductor.
- There is not anymore the problem due to the non perfect synchronization during the switching on of the two devices that had to generate the leg short circuit. This grants a better behaviour from the point of view of the harmonic distorsion of the output current.
- The new loop has a lower resistance with respect to the others, so when more devices are turned on it is correct to presume that the current is passing through the new leg (the one with IGBT7).

1.4 Space Vector Modulation for CSI

Differently from traditional modulation techniques, the space vector modulation does not adopt the separate control of the different phases and it fits perfectly for the implementation with micro-controller. Considering the three phase inverter and a star-connected three phase resistive load (as shown in Fig. 5), the on state of different device couples will lead to different operating states.

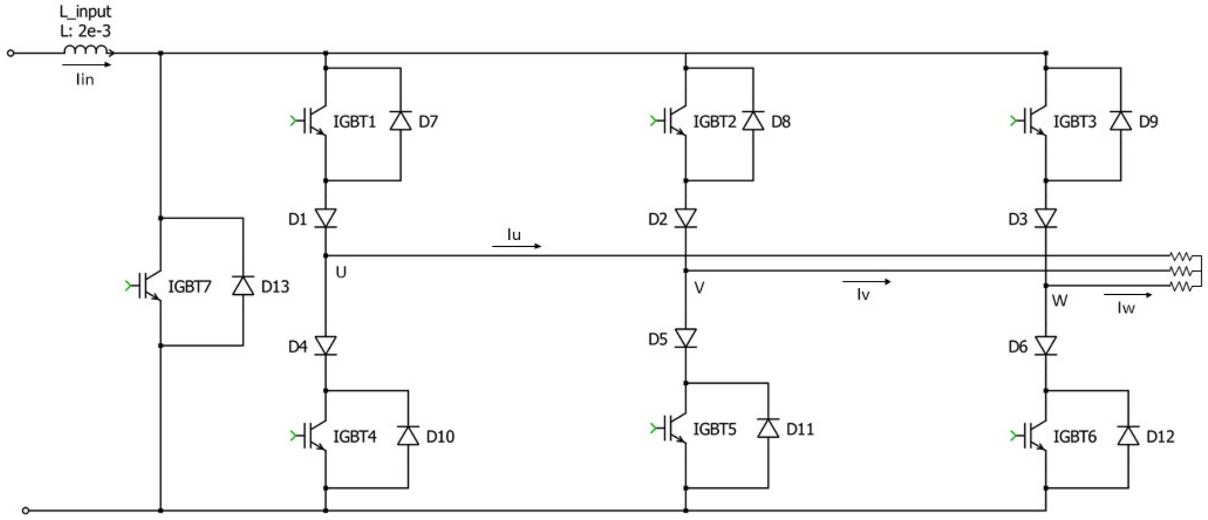

Figure 5: CSI7 architecture with current convention.

In the alfa-beta plane (Fig. 6), the operating region of the plane is divided into six regions that are called sextants and each vector I_{ref} into the circumference can be obtained as a sum of the two nearest vectors. So the correct time to stay in the states of the vectors adjacent to I_{ref} can be computed, when a switching period T_s is chosen. The remaining period time will be left for the off state, during which the current does not pass through the load but through IGBT7, which is associated to the state I_0.

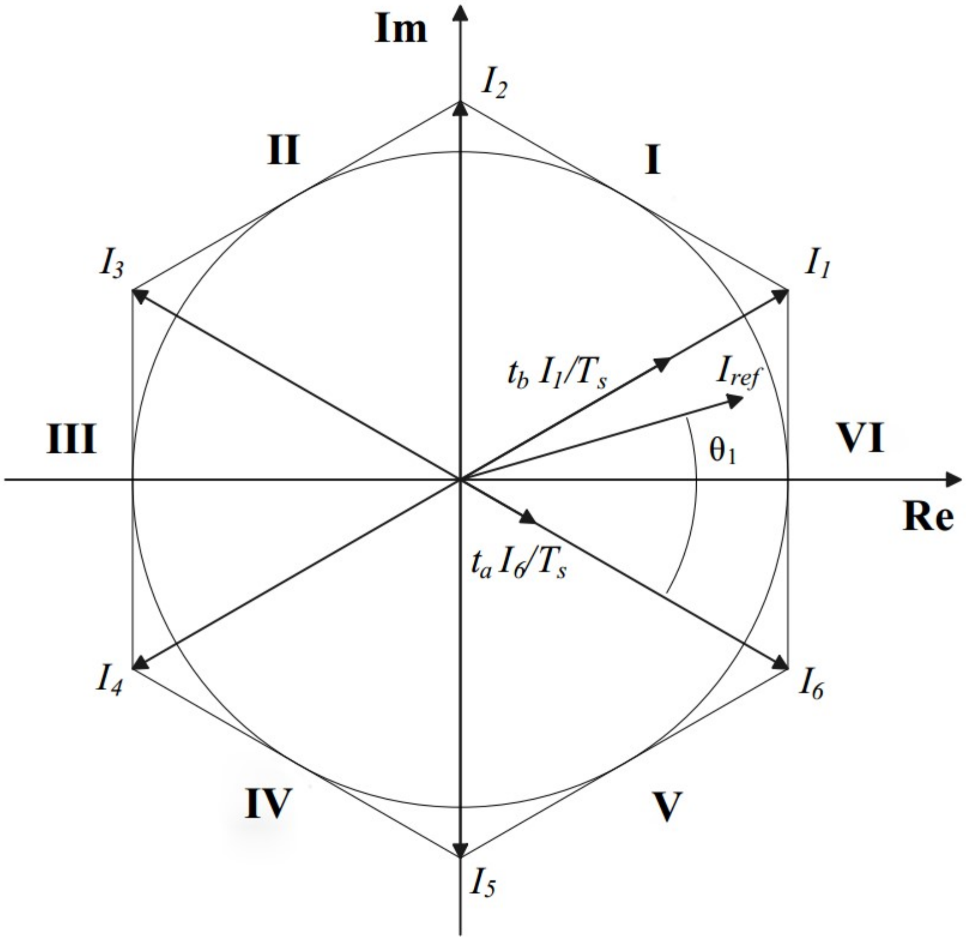

Figure 6: Current vectors on $\alpha\beta$ plane.

From i_α and i_β it is possible to determine in which sextant the current vector is. Firstly, from the sign of i_α and i_β the quadrant can be determined:

- If both are positives, the vector belongs to the first quadrant;
- If i_α is negative and i_β is positive, the vector belongs to the second quadrant;
- If both are negatives, the vector belongs to the third quadrant;

- If i_α is positive and i_β is negative, the vector belongs to the fourth quadrant.

Then it is possible to compute the conditions for every sextant and they are reported in the following table.

Table 1: Conditions for each sextant.

First quadrant	$i_\alpha <= i_\beta\sqrt{3}$	Sextant 1
	$i_\alpha > i_\beta\sqrt{3}$	Sextant 6
Second quadrant	$-i_\alpha <= i_\beta\sqrt{3}$	Sextant 2
	$-i_\alpha > i_\beta\sqrt{3}$	Sextant 3
Third quadrant	$-i_\alpha <= -i_\beta\sqrt{3}$	Sextant 4
	$-i_\alpha > -i_\beta\sqrt{3}$	Sextant 3
Fourth quadrant	$i_\alpha <= -i_\beta\sqrt{3}$	Sextant 5
	$i_\alpha > -i_\beta\sqrt{3}$	Sextant 6

Considering that the period of the PWM signal is much smaller than the rotating period of I_{ref}, it can be considered constant during the time computation. This allows to simplify the computations that the micro-controller has to perform in a time smaller than T_s. Nevertheless the switching frequency cannot be increased over certain values, because the switching losses can become too high and also the distortion of the output signal can increase when the overlap time is not tuned correctly.

The period of the PWM signal is given by the sum of the time spent in the two states adjacent to the desired current vector and the time T_0, during which the current flow through IGBT7.

$$T_s = T_k + T_{k+1} + T_0 \tag{1.4}$$

Applying the vectors of the discrete states it is possible to find the necessary times to obtain the desired current vector.

$$\int_0^{T_s} \left(\bar{I}_{ref}\right) dt = \int_0^{T_k} \left(\bar{I}_k\right) dt + \int_{T_k}^{T_k+T_{k+1}} \left(\bar{I}_{k+1}\right) dt + \int_{T_k+T_{k+1}}^{T_s} \left(\bar{I}_0\right) dt \tag{1.5}$$

Since I_0 is the state of null current, the following equation can be obtained from Eq. 1.5.

$$\bar{I}_{ref}T_s = \bar{I}_k T_k + \bar{I}_{k+1}T_{k+1} \tag{1.6}$$

$$\begin{bmatrix} i_\alpha \\ i_\beta \end{bmatrix} T_s = \frac{2}{\sqrt{3}} i_{in} \left(\begin{bmatrix} \cos\left(\frac{1}{6}+\frac{k-1}{3}\right)\pi \\ \sin\left(\frac{1}{6}+\frac{k-1}{3}\right)\pi \end{bmatrix} T_k + \begin{bmatrix} \cos\left(\frac{1}{6}+\frac{k}{3}\right)\pi \\ \sin\left(\frac{1}{6}+\frac{k}{3}\right)\pi \end{bmatrix} T_{k+1} \right) \tag{1.7}$$

$$\begin{bmatrix} i_\alpha \\ i_\beta \end{bmatrix} T_s = \frac{2}{\sqrt{3}} i_{in} \begin{bmatrix} \cos\left(\frac{1}{6}+\frac{k-1}{3}\right)\pi & \cos\left(\frac{1}{6}+\frac{k}{3}\right)\pi \\ \sin\left(\frac{1}{6}+\frac{k-1}{3}\right)\pi & \sin\left(\frac{1}{6}+\frac{k}{3}\right)\pi \end{bmatrix} \begin{bmatrix} T_k \\ T_{k+1} \end{bmatrix} \tag{1.8}$$

Resolving for T_k and T_{k+1} the following equation can be obtained.

$$\begin{bmatrix} T_k \\ T_{k+1} \end{bmatrix} = \frac{3}{4}\frac{T_s}{I_{in}} \begin{bmatrix} \sin\left(\frac{1}{6}+\frac{k}{3}\right)\pi & -\cos\left(\frac{1}{6}+\frac{k}{3}\right)\pi \\ -\sin\left(\frac{1}{6}+\frac{k-1}{3}\right)\pi & \cos\left(\frac{1}{6}+\frac{k-1}{3}\right)\pi \end{bmatrix} \begin{bmatrix} i_\alpha \\ i_\beta \end{bmatrix} \tag{1.9}$$

Remembering that

$$\begin{bmatrix} i_\alpha \\ i_\beta \end{bmatrix} = \bar{I}_{ref} = \left|\bar{I}_{ref}\right| e^{j\omega t} = \left|\bar{I}_{ref}\right| (\cos\omega t + j\sin\omega t) \tag{1.10}$$

Eq. 1.9 can be rewritten as follows.

$$\begin{bmatrix} T_k \\ T_{k+1} \end{bmatrix} = \frac{3}{4}\frac{\left|\bar{I}_{ref}\right|}{I_{in}} T_s \begin{bmatrix} \sin\left(\frac{1}{6}+\frac{k}{3}\right)\pi & -\cos\left(\frac{1}{6}+\frac{k}{3}\right)\pi \\ -\sin\left(\frac{1}{6}+\frac{k-1}{3}\right)\pi & \cos\left(\frac{1}{6}+\frac{k-1}{3}\right)\pi \end{bmatrix} \begin{bmatrix} \cos\omega t \\ \sin\omega t \end{bmatrix} \tag{1.11}$$

Defining the modulation factor as:

$$m = \frac{\left|\bar{I}_{ref}\right|}{I_{in}} \tag{1.12}$$

The final equation is:

$$\begin{bmatrix} T_k \\ T_{k+1} \end{bmatrix} = \frac{3}{4} m T_s \begin{bmatrix} \sin\left(\frac{1}{6}+\frac{k}{3}\right)\pi & -\cos\left(\frac{1}{6}+\frac{k}{3}\right)\pi \\ -\sin\left(\frac{1}{6}+\frac{k-1}{3}\right)\pi & \cos\left(\frac{1}{6}+\frac{k-1}{3}\right)\pi \end{bmatrix} \begin{bmatrix} \cos\omega t \\ \sin\omega t \end{bmatrix} \tag{1.13}$$

The modulation factor m states how much current will be sent to the load: since $\bar{I_{ref}}$ is limited to the circumference inscribed into the exagon of the sextants, the modulation coefficient has a maximum limit of $\frac{\sqrt{3}}{2}$.

Now the on and off times of the devices can be computed in order to obtain a specific current vector. In order to grant the presence of a loop for the current flowing through the bus inductance an overlap time (where I_0 is applied) must be introduced between two active states.

Furthermore, to delete the glitch due to the transition from a sextant to the next one, the order of application of the vectors must be reversed whether the sextant is even or odd, as shown in Fig. 7.

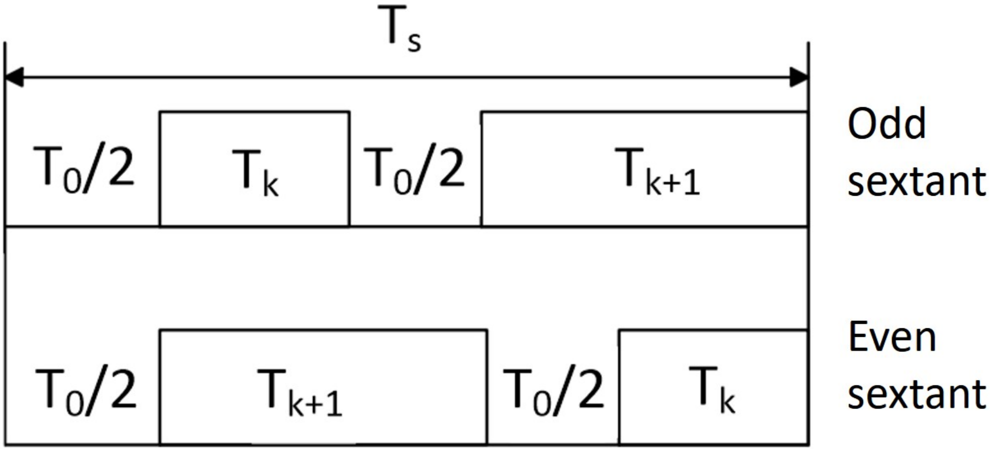

Figure 7: Switch on order of the devices.

1.5 Simulation of the Architectures and Comparison of Results

This chapter shows how simulations of the converter were performed and how different modulations, both innovative and traditional, resulted in performance differences. Simulations were done in Matlab-Simulink using the Plecs toolbox. Thermal models of conduction losses for relevant devices (IGBTs and power diodes) were created to obtain conduction loss data for both modulations.

Switching losses were intentionally ignored as they are present in both cases and are likely not as decisive compared to conduction losses. Moreover, switching losses are heavily influenced by device switching frequency, which does not affect conduction losses. Hence, excluding additional variability sources was deemed the best decision, as they could obscure the results of real interest.

Figure 8 shows the converter modeled in PLECS. Black lines represent electrical connections, and green lines represent signals, some of which are control signals (e.g., those going into the IGBT gate), while others are sensor readings. R1 and R5 represent the series resistance of real inductances, and R2, R3, and R4 represent connection resistances, set to very small values (fractions of ohms) for simulation purposes. The blue rectangle represents the heat sink connected to the enclosed elements. After introducing a thermal model, it will be possible to assess losses as a function of temperature. At the end of the blue line, representing the heat flow generated by the devices, there is a constant temperature source, with a very low thermal

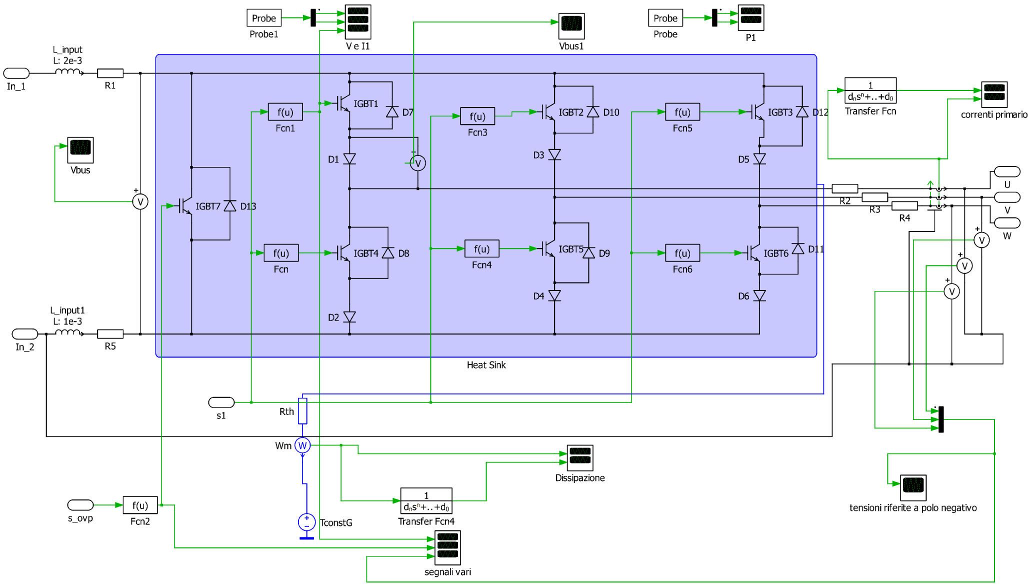

Figure 8: CSI simulation schematic.

resistance between it and the heat sink, ensuring that the sink remains at a fixed temperature. The Wm sensor measures the total thermal power produced by the devices, which corresponds to the conduction losses.

PLECS allows for thermal simulations, quantifying device losses and evaluating heat flows for correct heat sink sizing. For this simulation, components must be characterized by inputting datasheet information into the program's designated sections. Typically, for conduction losses, manufacturers provide voltage and current curves at various temperatures. In this case, key points from these graphs were selected, and the respective values were entered into tables. The program automatically interpolates the points to generate a 3D graph used in the simulation as a lookup table. Figures 9 and 10 show the values for IGBTs and diodes, respectively.

We will now list the results obtained from the simulations. First, it is useful to assess the conduction losses for the two modulation types. The input voltage in both cases is set to 240V by the control loop, making the input power the same: about 1440W in these conditions. The heat sink temperature is set to 50°C, and the dissipated thermal power is measured.

From a first comparison of conduction losses, it is clear that the innovative architecture modulation is much more efficient. With a total power of about 1.4KW, traditional modulation leads to around 50W of dissipation, compared to 35W for the innovative architecture. Therefore, the conduction losses of the innovative modulation are about 70% of those for the traditional modulation.

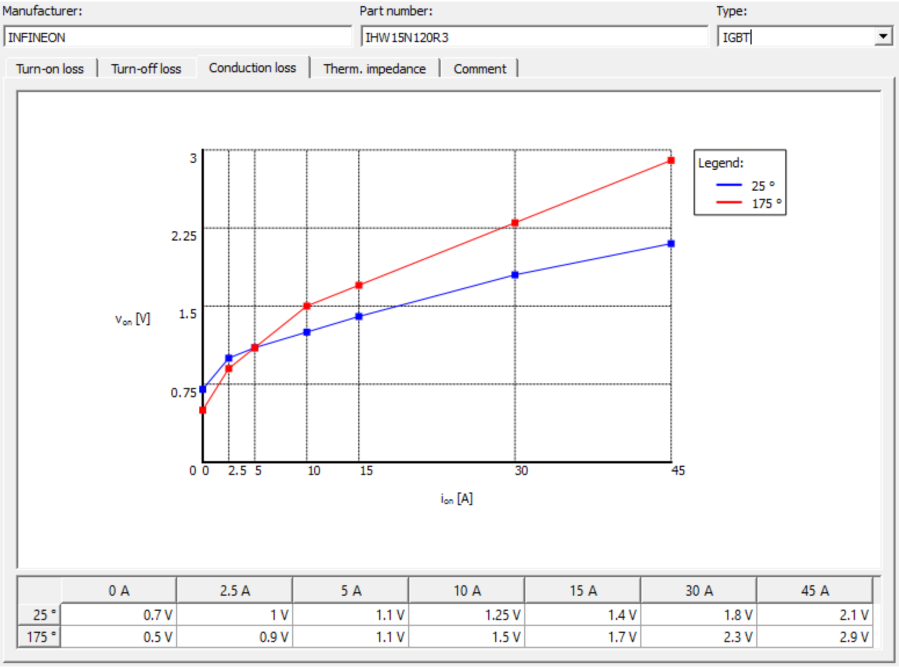

Manufacturer: INFINEON

Part number: IHW15N120R3

Type: IGBT

	0 A	2.5 A	5 A	10 A	15 A	30 A	45 A
25 °	0.7 V	1 V	1.1 V	1.25 V	1.4 V	1.8 V	2.1 V
175 °	0.5 V	0.9 V	1.1 V	1.5 V	1.7 V	2.3 V	2.9 V

Figure 9: IGBTs conduction thermal model.

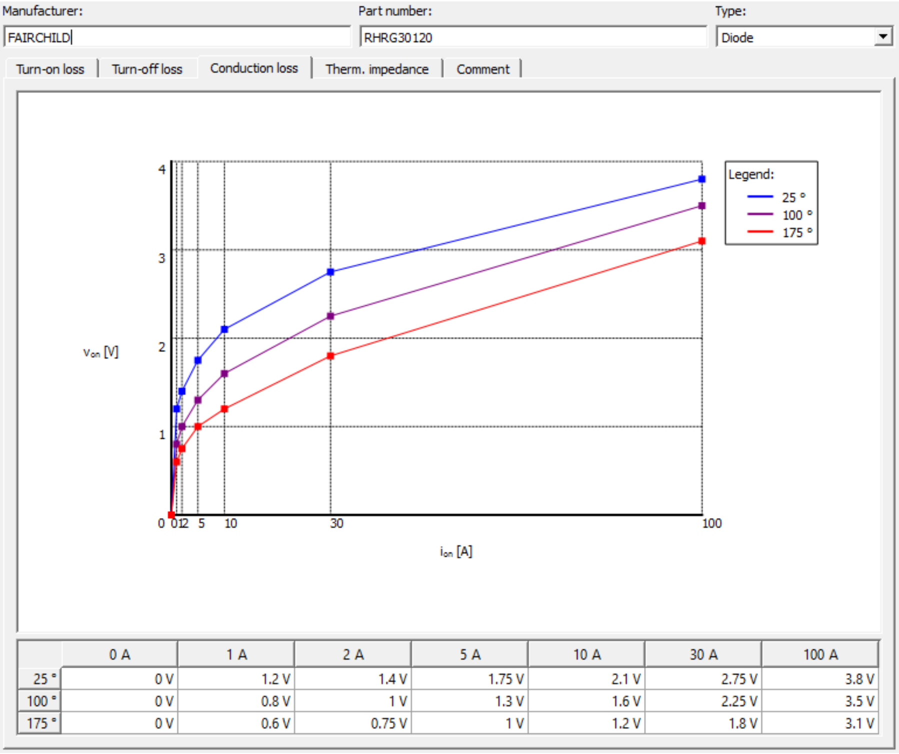

Manufacturer: FAIRCHILD

Part number: RHRG30120

Type: Diode

	0 A	1 A	2 A	5 A	10 A	30 A	100 A
25 °	0 V	1.2 V	1.4 V	1.75 V	2.1 V	2.75 V	3.8 V
100 °	0 V	0.8 V	1 V	1.3 V	1.6 V	2.25 V	3.5 V
175 °	0 V	0.6 V	0.75 V	1 V	1.2 V	1.8 V	3.1 V

Figure 10: Diodes conduction thermal model.

Modulation coefficient graphs further confirm that the innovative architecture requires a less aggressive (higher) value of "m" to achieve the desired power absorption.

The modulation coefficient has been previously defined in equation 1.12.

Reducing this value means directing a smaller portion of the input current to the load, spending more time in the inductor charging phase, thus increasing the ratio between the phase voltage and the input voltage (i.e., the voltage boost factor).

Due to higher losses, the traditional architecture requires a more significant boost factor to absorb the same power as the innovative one, but this leads to even greater losses in the leg short-circuit devices. The performance gap between the two converters increases as the boost factor rises.

For instance, by setting the input voltage to 200V (compared to the previous 240V), input power rises to 2KW, requiring both architectures to operate at a higher boost factor (thus a lower modulation coefficient). This is only possible in simulation; in reality, a source with the typical characteristics of photovoltaic devices would have a fixed maximum power point. Nonetheless, this test helps understand the architectures' behavior.

As can be seen in Figures 11 and 12, the losses nearly double, at least for the traditional architecture. The ratio of losses between the innovative and traditional architecture modulations is now about 64%. As expected, the performance difference grows as the modulation index decreases.

The analytical results are then confirmed by simulations: the innovative architecture has lower conduction losses than the traditional one.

1.6 Experimental setup and tests

A CSI7 prototype has been designed and developed. The board is reported in image 13. The functional blocks are identified from the following numbers:

1. Bus
2. Three phase bridge
3. Floating gate driver
4. Gate driver

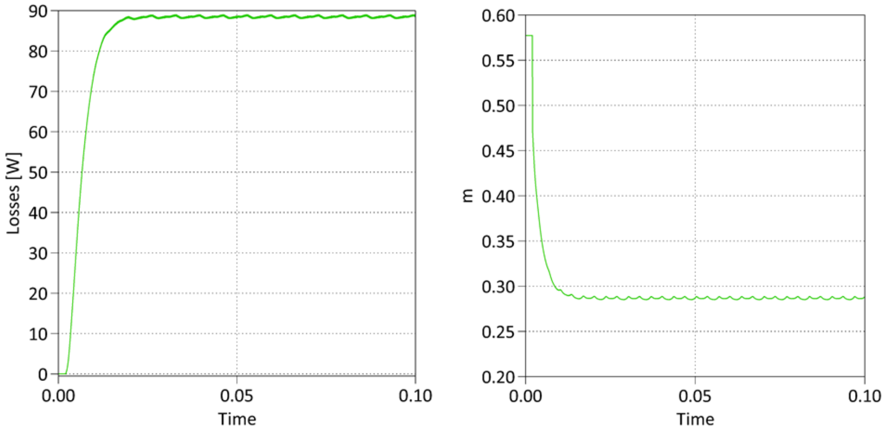

Figure 11: Simulation losses and m for the traditional modulation with Vin=200V.

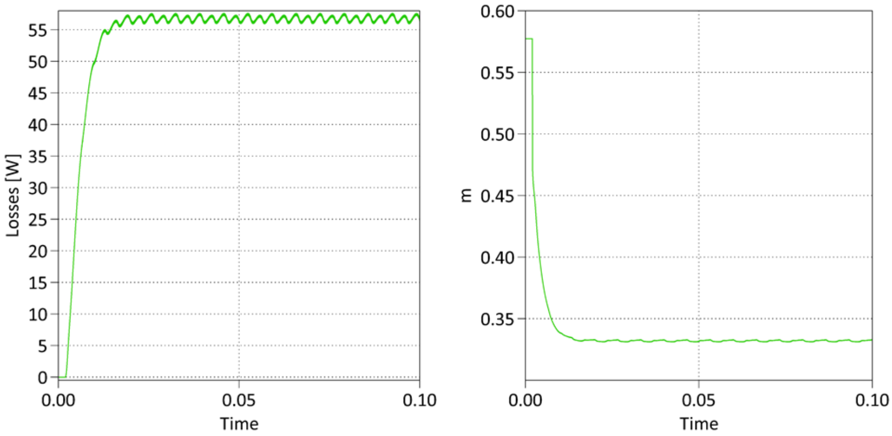

Figure 12: Simulation losses and m for the new modulation with Vin=200V.

5. PWM conditioning
6. Currents measurement
7. Voltage measurement
8. Faults sampling
9. 18V Power supply
10. Phase voltage measurement
11. 1,65V bias

Using the prototype board a set of experimental tests have been executed.

The PWM signal frequency was set to 10 kHz. The bus inductance was set to 1 mH.

A constant input voltage was provided by a 420W dual-channel bench power supply. The first channel was also used during the microcontroller programming phase to power the 5V logic board. The second channel was used for supplying power to the board.

To preserve the power supply and protect it from unwanted and potentially harmful current returns, a power diode was placed in series with it. After the diode, an additional 1 µF film capacitor was placed in parallel with the input of the CSI converter.

The quantities measured by the wattmeter are represented in Figure 15 as Am1, Vm1 (input current and voltage), and Am2, Vm2 (phase current and voltage).

In our case, the input power and the power dissipated on one of the three star-connected load impedances were measured. This choice was made because, using a balanced load, measuring the power dissipated on one of the impedances is sufficient to obtain the total power delivered to the load through simple multiplication. In addition to the powers, the input and phase voltage and current values were noted to confirm experimentally the actual voltage increase action performed by the converter.

The Total Harmonic Distortion (THD) of the phase voltage was also considered to evaluate the unwanted harmonic content introduced by the modulations of the different architectures.

The oscilloscope was used to capture the voltage and current waveforms of the phase, allowing for a visual assessment of the signal quality, which was already quantitatively expressed by the THD value provided by the wattmeter.

Tests were conducted with two different loads, both purely resistive and star-connected. The

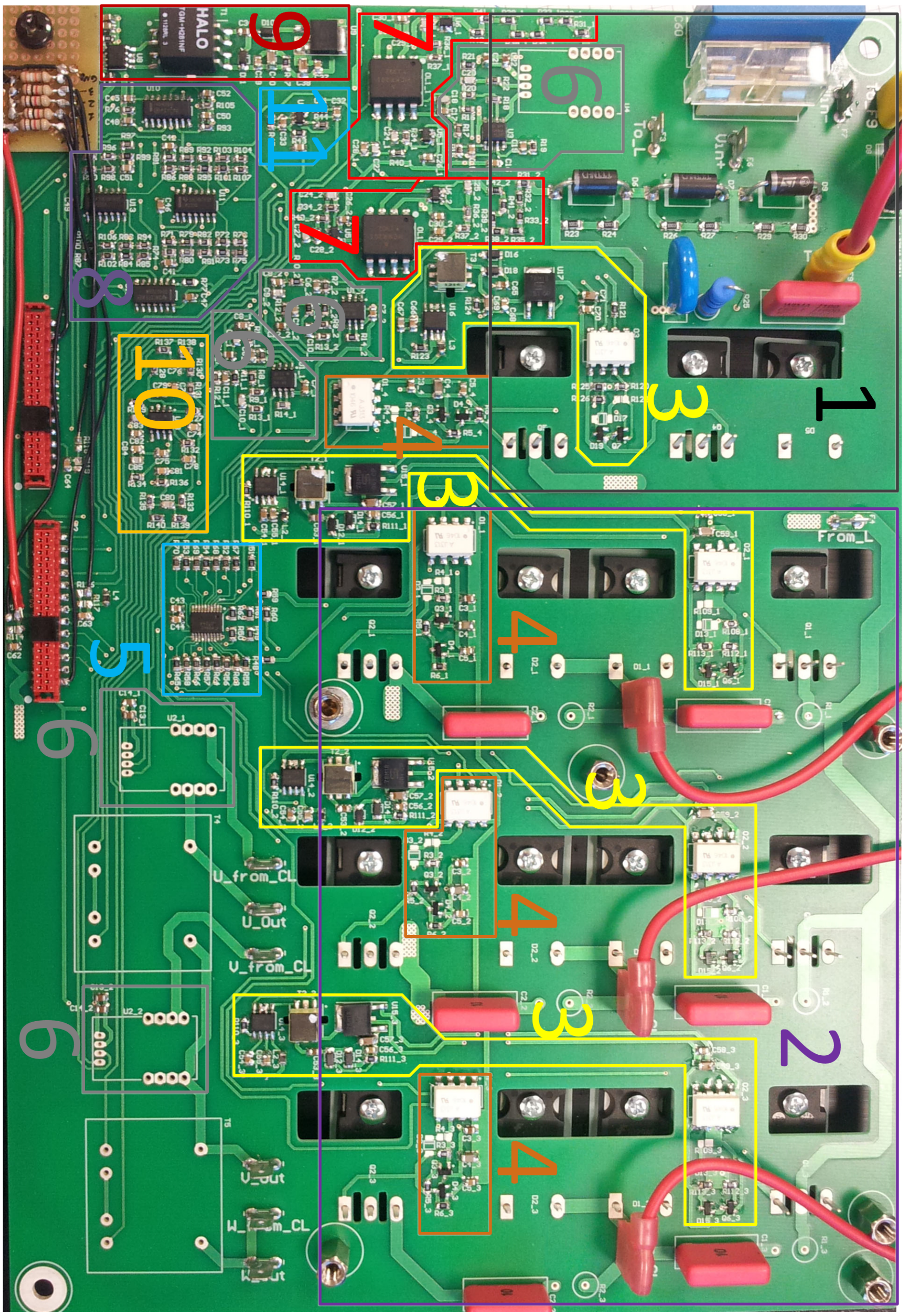

Figure 13: CSI7 board.

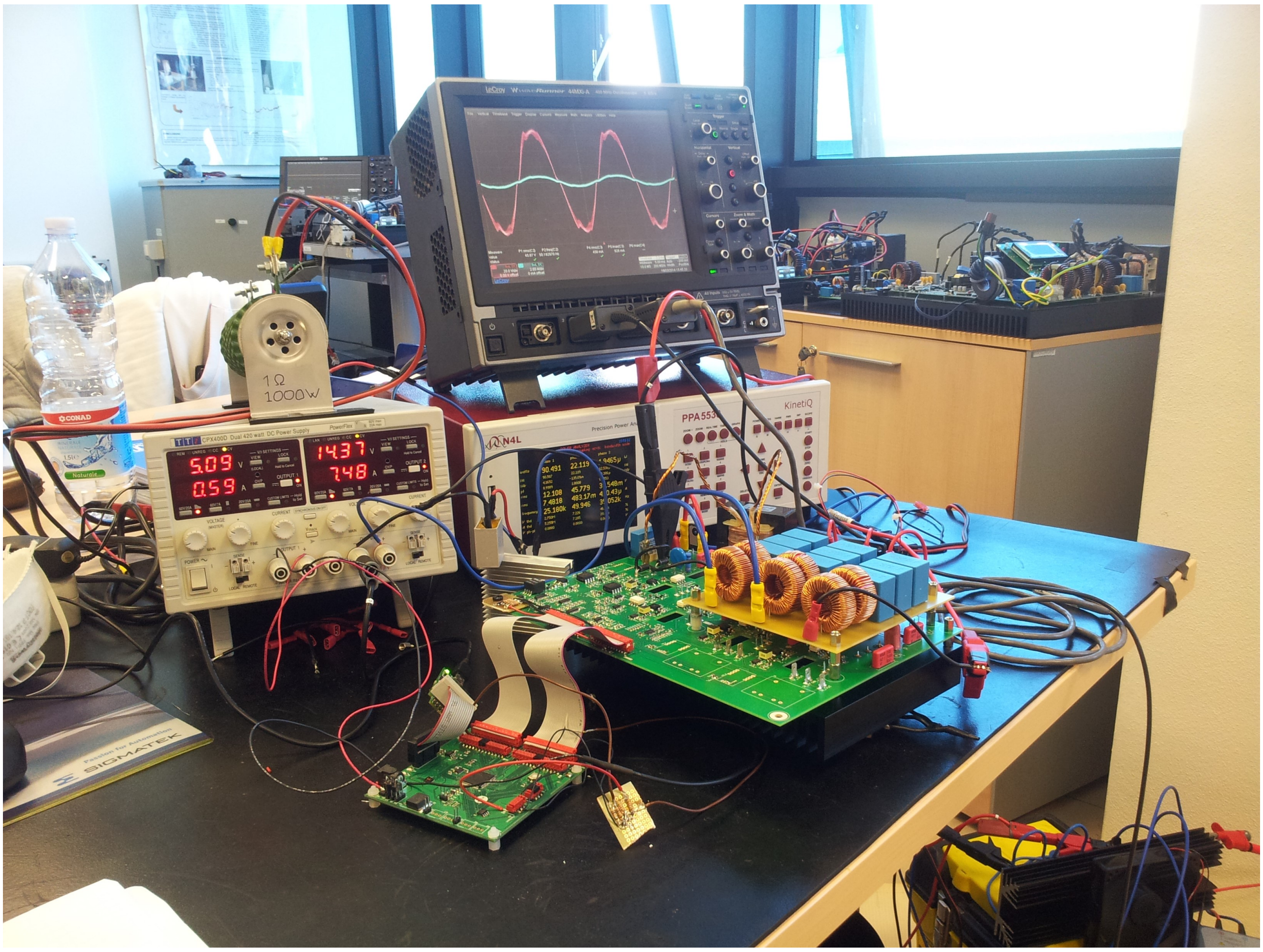

Figure 14: Bench test.

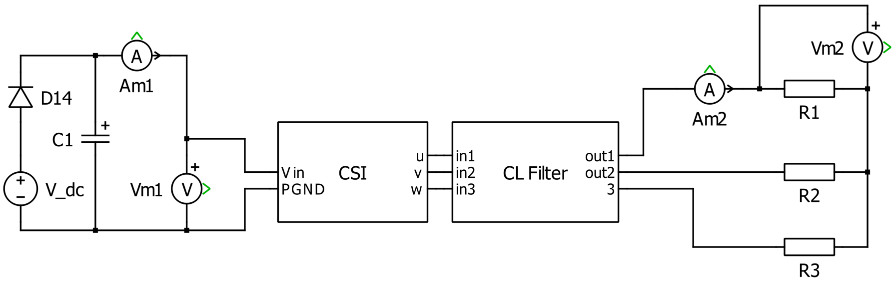

Figure 15: Bench test scheme.

resistors had to be attached to a heatsink, and for higher power tests, fans were also used to increase thermal exchange and thus heat dissipation.

The set of tests was performed using 3 resistors of 94Ω connected in a star configuration. These values were obtained with a series of two 47Ω resistors.

A factorial experiment plan was carried out on the variables:

- Input voltage (Vin)
- Modulation coefficient (m)
- Modulation type

The input voltages were varied at three levels, as was the modulation coefficient. In some cases, primarily due to the fact that some tests required a power absorption greater than what the power supply could handle, it was necessary to introduce an intermediate level for the input voltages so that some tests could be performed to provide meaningful data analysis. As mentioned previously, the load resistances were varied at two levels. The two levels of modulation type are:

- The innovative architecture, which uses IGBT7 (Figure 2-1) to perform the leg short circuit.
- The traditional architecture, which performs the short circuit by turning on two IGBTs belonging to the same leg.

1.7 Experimental tests results

The first observation that can be made is certainly regarding the better efficiency of the innovative architecture compared to the traditional one across all tests conducted (figs. 16 and 17). The experimental result is thus consistent with both the theoretical and simulation results.

Furthermore, it is observed that decreasing the modulation index, or increasing the phase voltage rise, results in a drop in efficiency. This occurs because the current values and the inductance charging time increase. As a result, focusing on a single PWM period leads to an increase in the Toff period, thereby increasing conduction losses in the devices operating the leg short circuit. For this reason, the traditional architecture is particularly disadvantaged: prolonged operation in this condition leads to increased losses in the four devices involved.

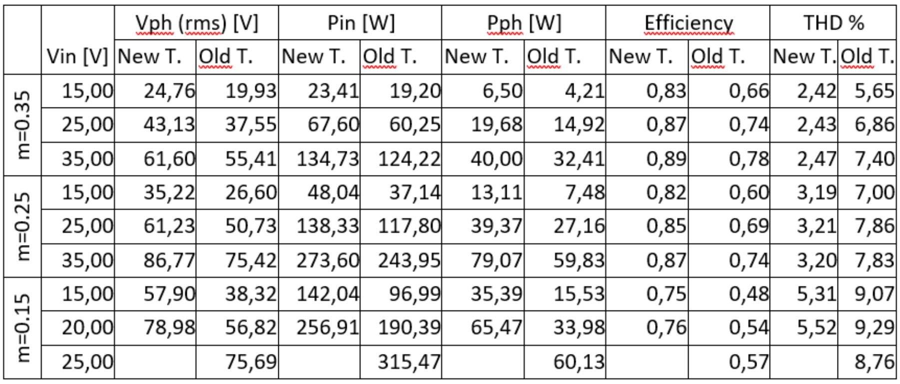

		Vph (rms) [V]		Pin [W]		Pph [W]		Efficiency		THD %	
	Vin [V]	New T.	Old T.	New T.	Old T.	New T.	Old T.	New T.	Old T.	New T.	Old T.
m=0.35	15,00	24,76	19,93	23,41	19,20	6,50	4,21	0,83	0,66	2,42	5,65
	25,00	43,13	37,55	67,60	60,25	19,68	14,92	0,87	0,74	2,43	6,86
	35,00	61,60	55,41	134,73	124,22	40,00	32,41	0,89	0,78	2,47	7,40
m=0.25	15,00	35,22	26,60	48,04	37,14	13,11	7,48	0,82	0,60	3,19	7,00
	25,00	61,23	50,73	138,33	117,80	39,37	27,16	0,85	0,69	3,21	7,86
	35,00	86,77	75,42	273,60	243,95	79,07	59,83	0,87	0,74	3,20	7,83
m=0.15	15,00	57,90	38,32	142,04	96,99	35,39	15,53	0,75	0,48	5,31	9,07
	20,00	78,98	56,82	256,91	190,39	65,47	33,98	0,76	0,54	5,52	9,29
	25,00		75,69		315,47		60,13		0,57		8,76

Figure 16: Experimental results on a three phase resistive load of 94ohm.

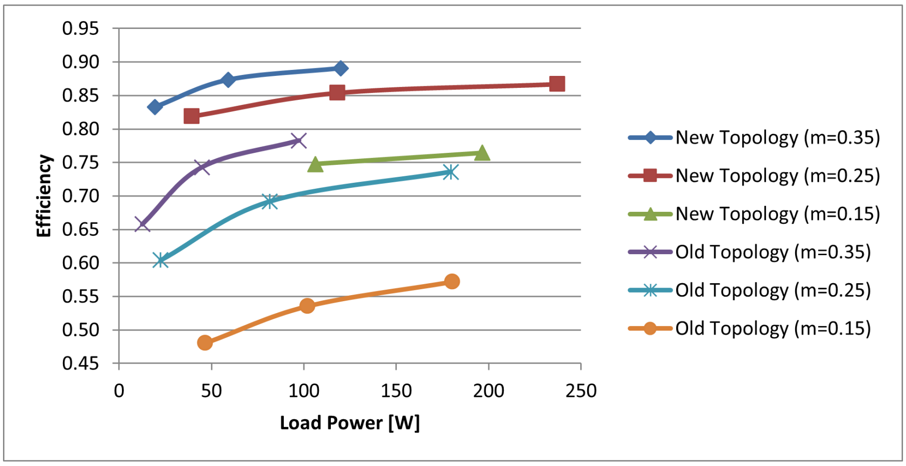

Figure 17: Efficiency.

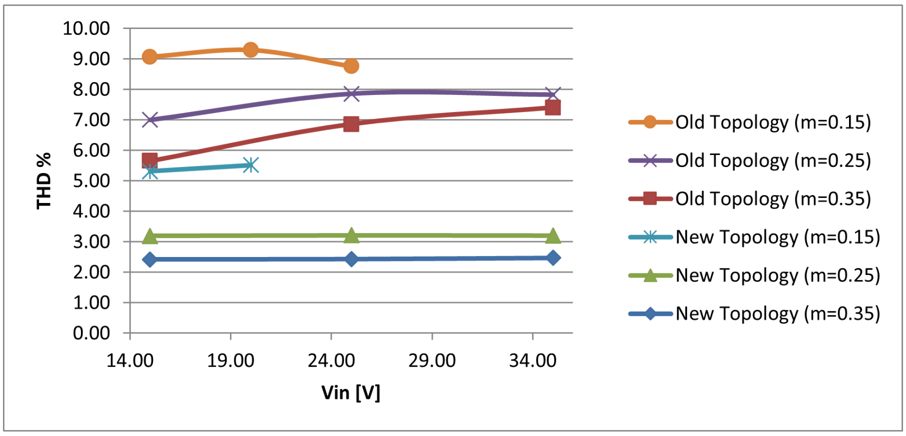

Figure 18: THD.

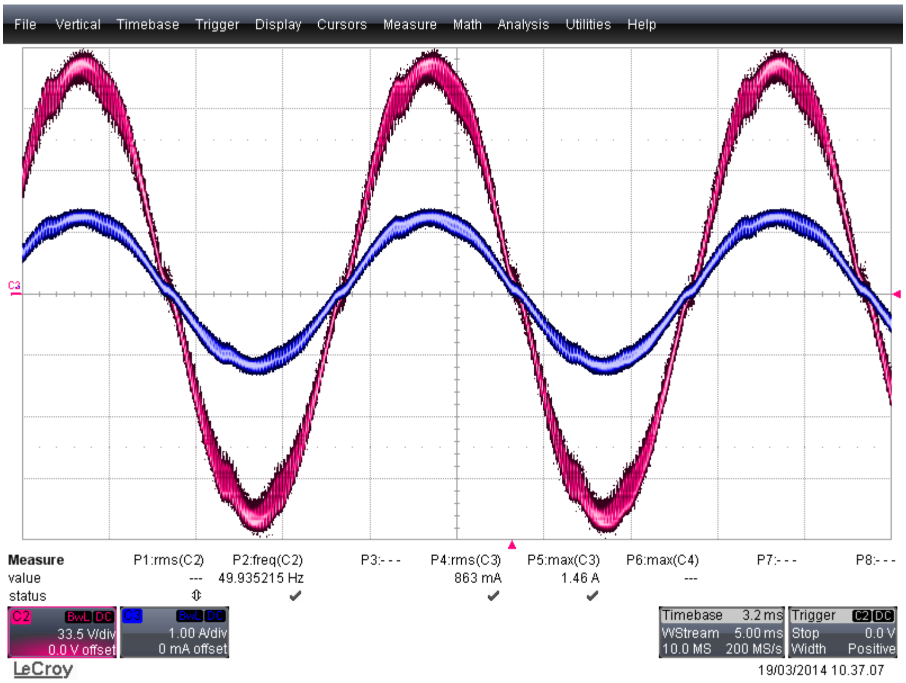

```
Measure   P1:rms(C2)  P2:freq(C2)      P3:- - -  P4:rms(C3)  P5:max(C3)  P6:max(C4)  P7:- - -  P8:- - -
value            ---  49.935215 Hz                   863 mA      1.46 A         ---
status             ⇕             ✔                       ✔           ✔
C2 BwL DC 33.5 V/div 0.0 V offset    C3 BwL DC 1.00 A/div 0 mA offset
Timebase 3.2 ms  WStream 5.00 ms  10.0 MS 200 MS/s    Trigger C2 DC  Stop 0.0 V  Width Positive
19/03/2014 10.37.07
```

Figure 19: Voltage and current waveform of the CSI7 output using the innovative modulation.

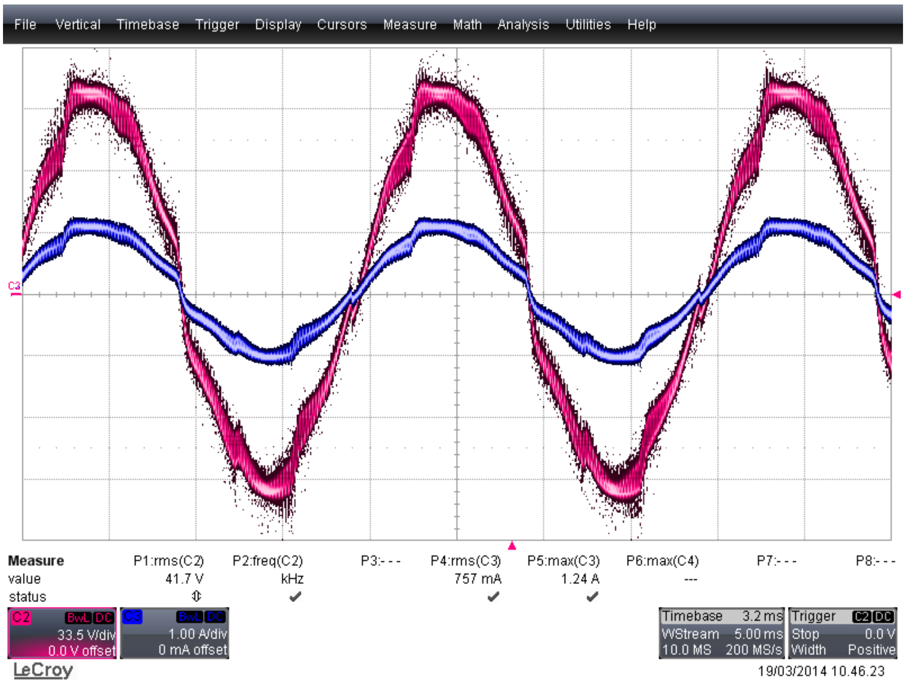

```
Measure   P1:rms(C2)  P2:freq(C2)      P3:- - -  P4:rms(C3)  P5:max(C3)  P6:max(C4)  P7:- - -  P8:- - -
value         41.7 V           kHz                   757 mA      1.24 A         ---
status             ⇕             ✔                       ✔           ✔
C2 BwL DC 33.5 V/div 0.0 V offset    C3 BwL DC 1.00 A/div 0 mA offset
Timebase 3.2 ms  WStream 5.00 ms  10.0 MS 200 MS/s    Trigger C2 DC  Stop 0.0 V  Width Positive
19/03/2014 10.46.23
```

Figure 20: Voltage and current waveform of the CSI7 output using the traditional modulation.

It is then observable that efficiency improves with an increase in input voltage. This happens because the voltage drops across the semiconductor devices remain almost constant, thus becoming less significant compared to the higher voltages involved.

Efficiency values can be improved by refining the modulation, specifically the turn-off delay introduced for each device to ensure a path always accessible to the current. Tests were conducted by setting this time to 0.75 µs. The trade-off for greater safety is a lower efficiency; in fact, the result of overlapping two adjacent states during switching causes the current to follow the path of lower impedance, which is certainly that of the leg short circuit. It should be remembered that in this configuration no power is sent to the load, but power is still dissipated due to conduction losses in the devices. Therefore, by adjusting this time, it would be possible to optimize the synchronization of the switches and ensure higher power to the load, improving efficiency.

The new topology shows less distortion compared to the traditional one (figs. 16 and 18). This aligns well with the intuitively expected result. In the traditional architecture modulation, during the transition to the leg short circuit state, the simultaneous activation of two devices must occur. The inevitable non-idealities of the devices and gate drivers lead to slightly different turn-on times, and thus a higher frequency harmonic content is expected to be more evident in the output signal. In the innovative architecture, only one device creates the leg short circuit, so it should not cause glitches or voltage spikes on the load due to imperfect synchronization during activation.

In fig 19 and 20 are reported the voltage and current waveforms acquired through the oscilloscope for the new and traditional modulation.

1.8 Conclusions

The innovative 7-device CSI architecture was developed. Two types of DC-AC converters (VSI and CSI) were presented for applications photovoltaic or electric drive control, and a comparison of their advantages and drawbacks. The 7-device CSI topology was studied from an analytical point of view, highlighting better achievable performance than the traditional topology. A Space Vector Modulation specification was identified for the particular architecture capable of minimizing dissipative losses and harmonic distortion. The behavior of the innovative architecture and the traditional architecture were simulated in the Maltlab-Simulink environment using the Plecs toolbox, showing that the former exhibits lower losses. Designs were then developed for the wiring diagrams and printed circuit board of the 7-device CSI converter, which was then been manufactured. The board was assembled by performing functional tests of the various modules. The control strategy and Space Vector Modulation were then implemented on the TI F28069 microcontroller so that it could perform both modulation for the innovative architecture as well as for the traditional architecture. Experimental tests were carried out on a resistive load to evaluate the performance of the innovative topology compared with the traditional one. From them, it was found that it provides better performance, reducing losses thus improving efficiency and harmonic distortion. Thus, full consistency of analytical, simulative and experimental results have been obtained.

2. CSI7 for PV applications

Solar photovoltaic (PV) market share grew significantly during the last decade, reaching widespread application. Because of the mass production and economies of scale that already dominate PV module fabrication, it is plausible that future developments will be focused on product standardization as well as reduction of installation and ownership costs (installation, cabling and maintenance/repair). Electronic power inverters are a key component in a PV system and their cost is becoming a bigger relative fraction of the PV system cost. Especially in large PV plants with centralized converters, the series/parallel connecting of numerous PV modules in long strings invariably led to MPP mismatch losses, mainly due to manufacturing tolerances or partial shading.

To overcome this situation different individual converters can be attached to a string with a reduced number of PV modules, to attain better MPP tracking (MPPT). A more radical approach is to integrate a minaturized dc-ac inverter into each PV module, obtaining a Module Integrated Converter (MIC). In literature, grid-tied PV plants with distributed converters were proposed, either with common DC Bus or with common AC Bus. A decentralized, modular PV installation with string inverters connected to a common three-phase distribution network has many benefits: the principal one being the use of standard, cost effective components and cables typical of industrial installations. A common DC bus on the contrary would require special expensive DC safety disconnectors and fuses, rated for DC voltages greater than 400V.

Devices currently on the market have shown that conversion efficiency and reliability are the main issues. To avoid maintenance costs and loss of production the expected lifespan of the PV String Inverter (SI) should be equal to that of the PV modules (e.g. 20+ years). This is the most challenging requisite because the electronic circuit is typically installed in a harsh environment with high operating temperature and is subjected to thermal cycling. For PV application, the dc-ac converter should also limit common-mode voltage fluctuation to prevent common-mode leakage currents on the module side, caused by the parasitic capacitance to ground inherent of PV modules construction. Moreover, SIs must comply to the same requirements in terms of grid compatibility (e.g., grid interface, electrical safety, harmonic distortion and electromagnetic compatibility) as their higher power centralized counterparts. In the framework of Smart Grid development, many countries already issued regulations requiring PV plants interfacing to the ac grid to be capable of reactive power compensation and dynamic grid support.

In the case of inverter architecture for PV grid interfacing it is possible to identify two main topologies: voltage source inverter (VSI) and current source inverter (CSI). The former one is the actual state of the art for module integrated inverters, while the latter one is a well known topology usually employed in medium-voltage high-power electric drives. A comparison of the efficiencies of VSI and CSI was presented in [7].

Because PV strings low voltage, almost all of the Voltage Source inverter architectures feature a two-stage conversion scheme: a dc-dc converter with a step-up transformer, followed by an high frequency full-bridge dc-ac inverter or an unfolding bridge. Single-stage, single-phase topologies are presented in literature, but they suffered of relatively low conversion efficiency or high harmonic distortion. [8].

All the single phase topologies require a bulky decoupling capacitor at the input. Electrolytic capacitors (ECs) are the only feasible alternative for decoupling, thanks to their high energy density, but they exhibit the shortest lifetime. In PV converters ECs represent the most important contribution to failures, accounting to 60-70 % of failures, to the point that inverters have an expected life span of only 3-7 years [9].

Current source inverter (CSI) is a topology traditionally employed in high-power electric drives. The present work concerns the performance analysis of this topology applied to three-phase grid-connected converters for PV power generation.

Photovoltaic CSI architecture has been proposed for full-sized array (several kW) both in single phase [10] and three-phase [11] architectures. Because the power decoupling component is an inductor, this architecture poses some critical issues during shut-down, as the current can't be instantaneously set to zero. Care must be taken especially in case of sudden power outages: some countermeasures to avoid dangerous voltage spikes on the DC link are suggested in [11]. Alternatively, in the proposed modular installation, the photovoltaic CSI string inverter can short circuit the PV input indefinitely as close to the PV modules as possible, thus reducing virtually to zero the string voltage. This feature could prove useful in case of emergency, such as in the event of fire: in case of a centralized inverter, opening the DC disconnector located at the inverter input would leave the full generator voltage still active on the DC line between the PV modules and the inverter, posing shock hazard to the emergency response teams.

Apart from this, CSI topology can offer some advantage when employed in PV applications: it is a single stage architecture, thanks to its inherent boost capability; it draws a smooth DC current from the PV modules, reducing their stresses; injected current is directly controlled; the energy storage component is an inductor, with a superior ruggedness and longer lifetime, especially when compared to electrolytic capacitors.

The design exploits CSI inherent step-up capability to obtain a single stage power interfacing between the low voltage PV input and the high voltage output, fed into the distribution grid. Compared to traditional VSI architecture, the investigated architecture allows for a greater input voltage range in a single stage topology, also allowing for a wide power range operation with given devices.

The use of space vector modulation for grid-tied CSI converters was presented in [12]. Modeling of CSI converters for PV applications is reported in [13] and the effect of common mode voltage was analyzed in [14]. The CSI topology applied to MICs has been previously investigated in [7], [15], suggesting the use in conjunction with dedicated high voltage solar modules, as well as adopting various solutions to overcome undesired common mode voltage variations. The well established method to reduce common-mode voltage variations in traditional CSI topology concerns the unused of the zero vectors (at the price to modulation index limitation and presence of output bipolar current pulses) or the use of a proper selection of the zero states [15].

Multilevels current source inverters solutions was recently analized in [16] and [17] and also with the possibility of a FPGA control [18], but the cost and complexity of this solutions do not seem to be adapted for low power applications. In addition to that, no output common-mode voltage variations are taken into account in these works in order to limit the ground leakage current.

The present work presents the implementation of a CSI topology named CSI7, particularly suitable to operate with high step-up voltage ratio, and hence with low-voltage, low-module count strings. A suitable SVM strategy was developed in order to minimize the THD of the injected grid-current and conduction power losses. Moreover a simple loop control was proposed to control the PV power converter in MPPT operation.

The CSI topology with an additional leg was first introduced in [19] to allow PWM modulation of SCRs converters: the additional GTO switch on the fourth leg was used to switch off the SCRs. Recent works investigated the potential to add a four leg in the traditional CSI topology constituted of a simple series of two reverse blocking switches. In [20] the four leg was used to provide a fourth switch configuration able to produce a zero vector in order to reduce the common-mode voltage variations. In [21] the mid point of the four leg was connected to the neutral of the three-phase grid and to mid point of voltage divider made of two capacitors in series. In this way the ground voltage across the PV parasitic capacitances is theoretically constant and no ground leakage current arises. However this solution present some disadvantages, such as the current circulation in the neutral connection wire and therefore an inferior performance in terms of efficiency and THD of the phase currents. In addition, the balancing of the capacitor voltage divider is not guaranteed. The CSI7 topology was presented in [22] and with a different SVM strategy aimed at reducing the switching commutations count in [23]. With respect to the previous work, this chapter presents an improved description of the CSI7 solution highligthing the ability to operate without the use of the blocking diode on the additional switch and the impact on reducing ground leakage current. In particular the experimental validation assesses the proposed CSI7 architecture and SVM in terms of injected currents distortion, efficiency and ground leakage current mitigation.

The following sections detail the research work and the experimental assessment that was carried out for the CSI7 topology in the present work. After a brief recall of the standard space vector (SV) modulation for CSI converters, Section II presents the proposed topology and associated PWM switching strategy together with the power converter control. Section III reports the simulation results for the proposed topology in Matlab/Simulink environment. Section IV details the experimental setup and the results obtained on a full-size laboratory prototype during grid-tied operation.

2.1 Proposed Current Source Inverter for PV grid-connected systems

2.1.1 CSI Topology

Figure 21 shows the proposed topology for the three phase CSI for PV String Converter applications. With respect to the classic CSI topology, in the proposed topology there is an additional power switch: S_7. This additional power switch, together with a suitable PWM strategy, allows to strongly decrease the conduction power losses of the main power switches and also limit the distortion due to commutation glitches, as it will be explained in the following. In the meantime also the ground leakage current can be reduced thanks to the presence of this additional switch.

The CSI topology is characterized by higher semiconductor power losses with respect to VSI topologies [24], especially in the case of high step-up voltage operation. In fact the six power switches (made by series connected mosfets + diodes, Fig. 21) constituting the classic CSI topology must withstand both the DC output current of the PV Panel and the high voltage of the grid. The resulting conduction power losses are quite high since at any given time the input DC Link current flows always through 2 power switches and 2 diodes. Therefore efficiency of the CSI improves as the DC input voltage increase. Semiconductor power losses remain virtually unchanged in presence of a very large variation of the input DC voltage, depending only on the DC input current value.

Since in this work the CSI is used in a PV String Converter application, the conduction power losses would be intrinsically very high. The introduction of the power switch S_7 allows to reduce the number of power semiconductors in series during the short circuit of the input DC inductance from four devices to only one. If a high step-up voltage ratio is required, this short-circuit time is a very large fraction of the total PWM period.

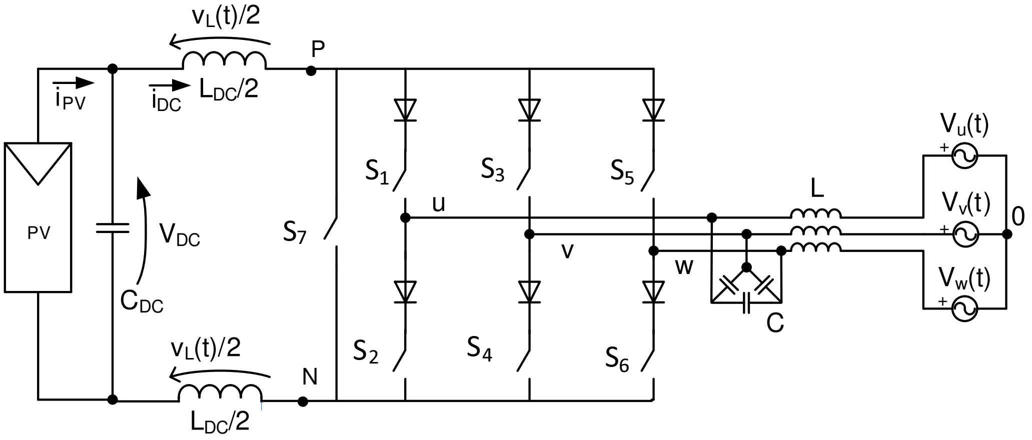

Figure 21: Three-phase CSI7 topology.

The six power switches S_1–S_6 can be driven as a classic CSI. Table 2 summarizes the permissible switching combinations for the CSI: nine space vectors (SV) of the bridge phase currents are obtained for the normal mode of operation [25]. Six SV are non-zero vectors (active state vectors) and three are zero (or null) vectors. Null vectors are traditionally obtained by short-circuiting the DC-link through a leg short-circuit. In the proposed solution these null vectors are not employed: the null state is created by switching on the additional power switch S_7.

All the switching states are defined by the switches configuration $S_1 - S_6$ of the bridge (where

Table 2: Switching states of a classic CSI .

State	**Switch Configuration** $(S_1S_2S_3S_4S_5S_6)$	**Output Vector**
1	1 0 0 0 0 1	$I_1 = \frac{2}{\sqrt{3}} e^{j\frac{\pi}{6}} I_{DC}$
2	0 0 1 0 0 1	$I_2 = \frac{2}{\sqrt{3}} e^{j\frac{\pi}{2}} I_{DC}$
3	0 1 1 0 0 0	$I_3 = \frac{2}{\sqrt{3}} e^{j\frac{5\pi}{6}} I_{DC}$
4	0 1 0 0 1 0	$I_4 = \frac{2}{\sqrt{3}} e^{-j\frac{5\pi}{6}} I_{DC}$
5	0 0 0 1 1 0	$I_5 = \frac{2}{\sqrt{3}} e^{-j\frac{\pi}{2}} I_{DC}$
6	1 0 0 1 0 0	$I_6 = \frac{2}{\sqrt{3}} e^{-j\frac{\pi}{6}} I_{DC}$
7	1 1 0 0 0 0	$I_7 = 0$ not employed
8	0 0 1 1 0 0	$I_8 = 0$ not employed
9	0 0 0 0 1 1	$I_9 = 0$ not employed

1 = conducting). Figure 22 shows the corresponding switching space vector. Any given current reference vector I_{ref} is obtained as a time weighted linear combination of the switching vectors of the corresponding sector: t_a and t_b for the two active state vectors and t_z for the null state vector (d_a and d_b represent simply the normalized time intervals with respect to the switching period T_s).

$$\begin{cases} t_a = d_a T_s \\ t_b = d_b T_s \\ t_z = T_S - (t_a + t_b) \end{cases} \tag{2.1}$$

The angle $\theta 1$ is used for the computation of the dwell time intervals t_a and t_b, while θ_{SVI} is the angle of the current space vector I_{ref} which is used to compare it with the angle of grid voltage space vector $\vec{V_g}$, named θ_g.

The phase voltage of the grid are considered:

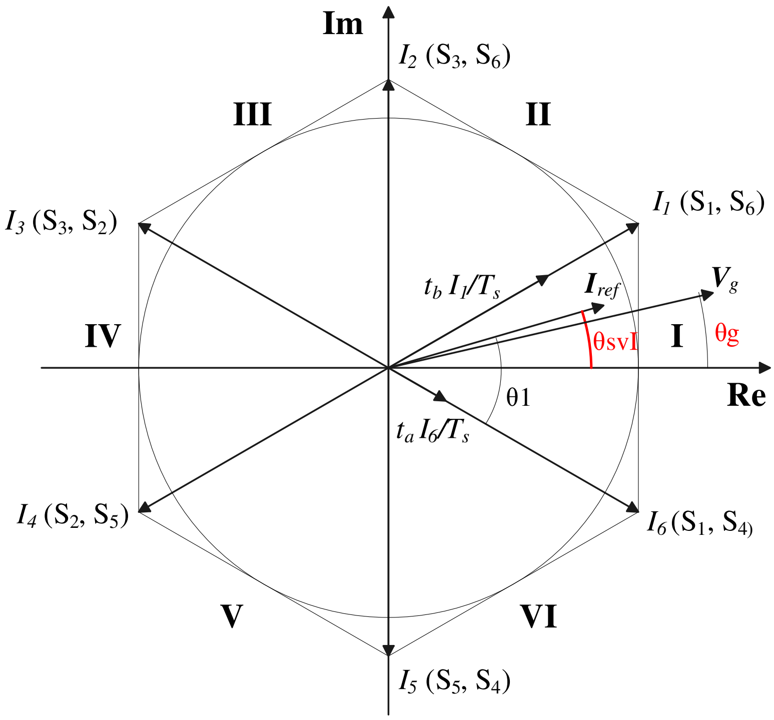

Figure 22: Space vector representation.

$$\begin{cases} v_u = V_g cos(\omega t) \\ v_v = V_g cos(\omega t + 2/3\pi) \\ v_w = V_g cos(\omega t + 2/3\pi) \end{cases} \tag{2.2}$$

The space vector of the grid voltage is $\vec{V_g} = V_g e^{j\omega t = j\theta_g}$, while the space vector of the injected current is $I_r\vec{e}f = V_g e^{j\theta_{SVI}}$. When the converter works in unity power factor operation $\theta_g = \theta_{SVI}$.

In the proposed topology, shown in Fig. 21, a simple power switch (Mosfet or IGBT) without a diode in series for S7 can be adopted only if the voltage across it is always positive from drain (collector) to source (emitter). Figure 23 shows the instantaneous phase voltages and the respective SV sectors of current space vector when the the CSI7 operates at unity power factor ($\theta_g = \theta_{SVI}$). Figure 24 details the instantaneous values of the line-to-line voltages, v_{uv} e v_{uw} for Sector I. The following analysis is conducted for Sector I, but the assumptions are valid also for the others SV sectors.

The evolution of line-to-line voltages during Sector I of the space vector current is fundamental in order to understand the circumstances leading to a negative voltage applied across switch S7, whereas a diode must be inserted in series.

During the sector I, with PF=1, when the two active vectors applied are I1 (S1 and S6 ON) and I6 (S1 and S4 ON). During the application of these two switches configuration, the voltage across the switch S7 is respectively equal to voltages v_{uv} (I1) e v_{uw} (I6) plus two voltage drops across the inductive part (L) of the output filter. It is important to point out that during the active vectors the inductive voltage drops determine a positive incremental contribution of the voltage across S7 and therefore neglecting these voltage drops represents a worst condition in order to find the operating condition range in which this condition is satisfied.

Figure 24 not only shows that the line-to-line voltages v_{uv} e v_{uw} are positive in case of unity power factor but also that there is a phase margin equal to $+\pi/6$ and $-\pi/6$ between the space vector of the grid voltage and the injected grid current, $\phi = \theta_g - \theta_{SVI}$, in which the voltage across S7 is still positive. This implies that the CSI7 converter can operate with a simple switch for S7 (without the diode in series) with a PF that can decrease down to 0.866, thus giving the capability for a reasonable amount of inductive and capacitive reactive power injection.

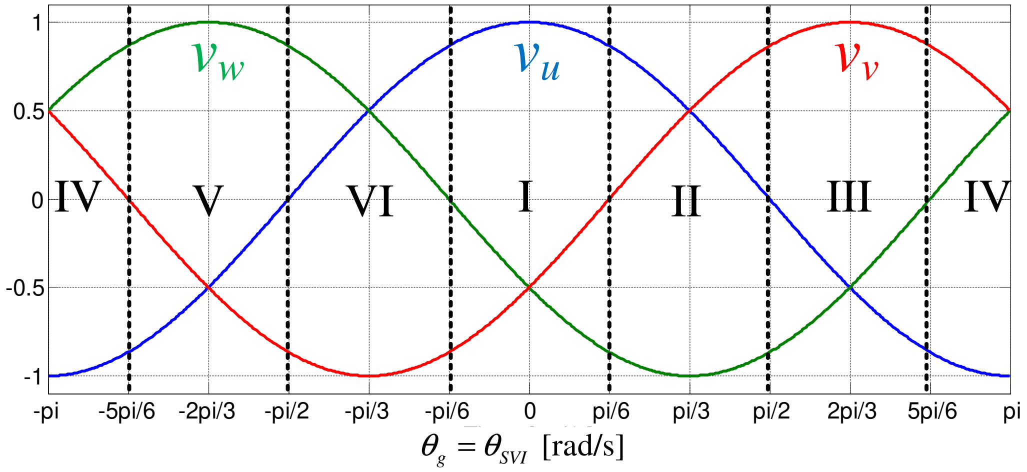

Figure 23: Grid phase voltages with sector numbers of the space vector current in case of unity power factor.

2.1.2 Proposed Current Space Vector Modulation

To maintain linearity, the SV space of Fig. 22 is limited to the inner circle of the hexagon, hence the modulation index value ($m = |I_{ref}|/I_{DC}$) is restricted to $0 \leq m \leq \sqrt{3}/2$. Different SV sequences are available, from basic ones [26], to more sophisticated ones, as to minimize

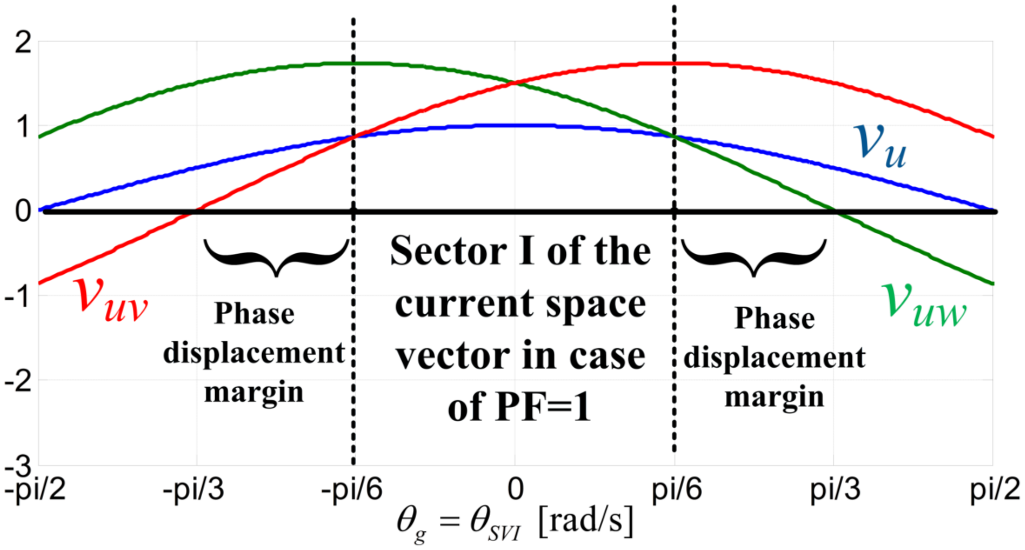

Figure 24: Power factor operation range to guarantee a positive voltage across S7 during the I sector.

switch commutations and switching lossess or to reduce distortion in supply current [27].

The PWM strategy to be implemented should ideally:

- guarantee overlap times between CSI commutations to avoid voltage spikes on the DC link
- avoid glitch generation by the PWM strategy during sextants changes
- minimize THD of the injected current
- minimize ground leakage current caused by common mode voltage on the input terminal
- minimize power losses

Because the output filter is a CL-type filter which has a lightly damped second-order characteristic, it shows a lightly damped resonant behavior: output glitches and spectral components at the resonant frequency can cause the output filter to ring. This glitch effect can be attenuated using an active damping as shown in [28], [29]. In the present work, instead of implementig passive or active damping solutions for CL resonance of the output filter, the proposed modulation aims to minimize the excitation of the output CL filter by avoiding glitches generation. Glitches can be caused during the transition of the current space vector from one SV sextant to the adjacent or by an undesired path of the output current of CSI due to the introduction of overlap times.

The first cause of glitch generation can be eliminated with an accurate choice of SV sequence for every sextant in order to avoid the consecutive application of the same active state vector at end of one sextant and at the beginning of the next as well as avoiding transition between two active state vectors that are more than $\pi/3$ apart.

The second cause is eliminated with the introduction of the power switch S_7 since the overlap time between an active state vector and a null state vector is obtained by widening its ON-time: i.e. leading and lagging the ON state with respect to the other active states transitions. The overlap time in CSI inverter modulation is required in order to avoid momentary DC input inductor open circuit, a condition symmetrical to dead time introduction in VSI inverter modulation.

In CSI operation an overlap time, t_{ov}, is needed for safe commutations between current space vectors. This overlap time causes distortion in the injected current waveforms if it is not accurately compensated. Since the application described in this chapter requires a high boost factor, the modulation index m is so low (this assumption will be detailed in the following section) that it makes difficult any finer subdivision of the active times t_a and t_b.

An effective overlap time compensation can be obtained only if every active state vector is separated from the others by the null state vector which represents the dominant state vector during overlapping. The SV sequence which satisfy these requirements is described in Fig. 25 and was named Alternated Sequence. The figure shows two different SV sequences, one for odd and one for even sextants. The change in commutation order is required to eliminate glitches during sextant transitions, as explained earlier.

The power switch S_7, besides ensuring a strong reduction of conduction power losses, also helps to solve this problem since it is the only contributor to null state vector generation, because of S_7 conduction voltage drop is lower than the other reverse-blocking switches (transistor with series connected diode). By using S_7 together with the alternate commutation sequence, the overlap time ensures that S_7 is active during every turn-on and turn-off transient of the reverse-blocking switches (S_1 to S_6). This ensures that all the commutations of S_1 to S_6 happen under zero current (ZCS), as all the input DC current flows on S_7. Under these operating conditions S_7 is the only device operating under hard switching. This behavior will be investigated in the simulations section.

Figure 26 shows the effect of overlap time t_{ov} on the proposed commutation strategy. The overlap time is introduced as the firing signal of power switch S_7. Because the null state is dominant with respect to other active states, the effective active vector times for the alternated sequence are:

$$\begin{cases} t_a{}' = t_a - 2t_{ov} \\ t_b{}' = t_b - 2t_{ov} \end{cases} \tag{2.3}$$

The SV modulation times t_a, t_b were compensated accordingly, by adding $2t_{ov}$ to them.

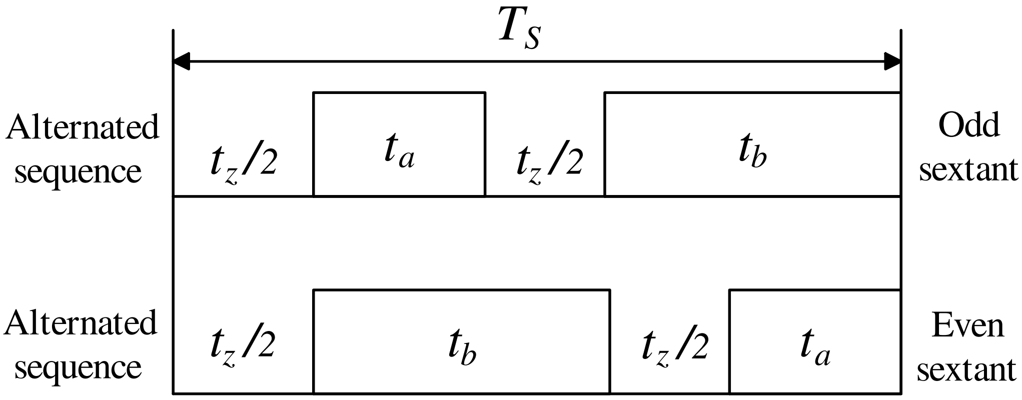

Figure 25: Alternated Sequence, details of commutation sequence for even and odd sextants to avoid glitch generation.

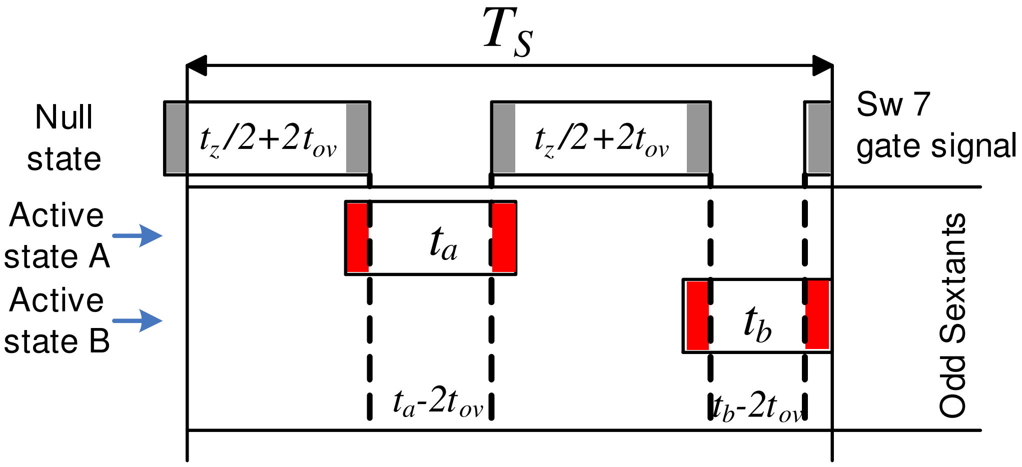

Figure 26: Alternated sequence - overlap time t_{ov} effect (scale exaggerated for demonstration purpose).

Another important issue that has to be taken into account in PV transfomerless topologies is the ground leakage current, that is mainly caused by the part of common-mode voltage variation introduced by the power converter operation [30].

With respect to traditional topologies, the CSI7 solution is able also to reduce the ground leakage current flowing through the parasitic capacitance between the PV panels and the ground.

In the proposed topology, shown in Fig. 21, the common-mode voltage can be computed using the neutral connection of the three-phase grid voltage as voltage reference, see (2.4).

$$v_{cm} = \frac{V_{P0} + V_{N0}}{2} \tag{2.4}$$

This way the instant values of the common-mode voltage during every active switches configuration can be easily computed and results respectively: $-v_v/2$ for vector I1,$-v_u/2$ for vector I2, $-v_w/2$ for vector I3, and so on. These instantaneous values are the same both in case of traditional CSI topology and the proposed CSI7 solution. The advantage of the latter is that, with the introduction of the additional switch S7, the null vector can be applied by S7 alone, while all the other transistors are turned Off. While in case of traditional CSI during the application of the three different null vectors, the instantaneous v_{cm} assumes the following voltage values: $v_u/2$,$v_v/2$ and $v_w/2$. Instead in case of the CSI7 solution, during the null vector configuration, the instantaneous v_{cm} is 0 thanks to the disconnection of the PV panels from the grid at the price of an increased number of commutation per cycle.

Section III shows some simulation results which compares the v_{cm} waveforms in the two cases.

2.1.3 Proposed control

In order to extract the maximum available energy from the PV source, the output voltage of the PV string is controlled by a MPP tracker. Therefore the first goal for assessing the performance of a PV CSI concerns its capability to operate in steady state conditions under a large input DC voltage variation. A steady state condition with an almost constant input DC current, i_{DC}, can be obtained when the mean value of the voltage across the input inductor L_{DC} of the CSI is null. Since the injected grid current is always at the same frequency of the grid voltage and thanks to the symmetry of the grid generator the evolution of the voltage across L_{DC} is the same for every SV sextant. The integral of $v_L(t)$ over a switching period, T_s in the sextant I of the SVM is shown in eq. (2.5).

$$\int_{t}^{t+Ts} v_l(t)\mathrm{d}t = \int_{t}^{t+Ts} ((V_{DC} - v_{wu}(t))t_a + \\ +(V_{DC} - v_{vu}(t))t_b + V_{DC}t_z)\mathrm{d}t = 0 \tag{2.5}$$

It is then possible to compute the voltage V_{DC} which satisfies eq. (2.5) obtaining a linear relationship between output voltage and the modulation index, as reported in [22].

This property is very important in order to limit the current ripple of I_{DC} which shows only an harmonic at the switching frequency. Figure 27 shows the relationship between the modulation index m and the V_{DC} at different power factor operation.

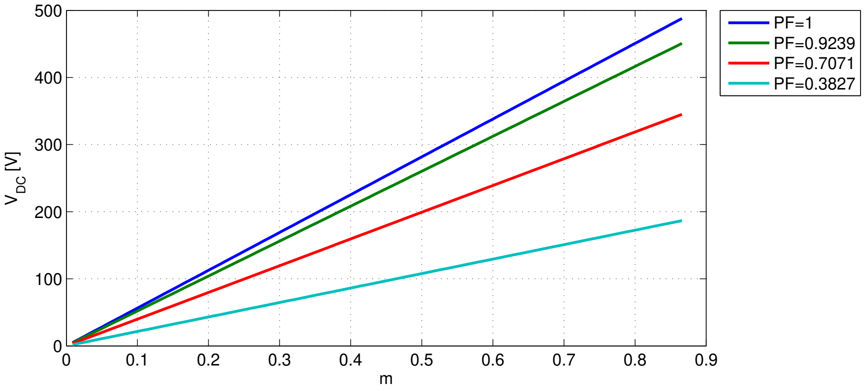

Figure 27: Relation between modulation index and V_{DC} of the PV module.

The CSI performance presented previously indicates the feasibility of the CSI to operate with a photovoltaic source as the output voltage of the PV panel can be properly controlled by a MPPT algorithm.

Figure 28 shows the proposed CSI control. The input voltage control loop employs a PI regulator which provides the modulation index m_d, proportional to the active current injected into the grid. In other words, the amplitude of the ideal active current can be obtained as $I_d = m_d * I_{DC}$. The modulation index m_q can be fixed to zero or varied to futher fine-tune the power factor of the CSI: in fact the presence of the capacitance-inductive output filter determines reactive power absorption. However, the power factor control capability of the proposed converter is beyond the scope of the present work. The modulation indexes m_α m_β are computed by Park's transform and used as input of the SVM. The two indexes are used

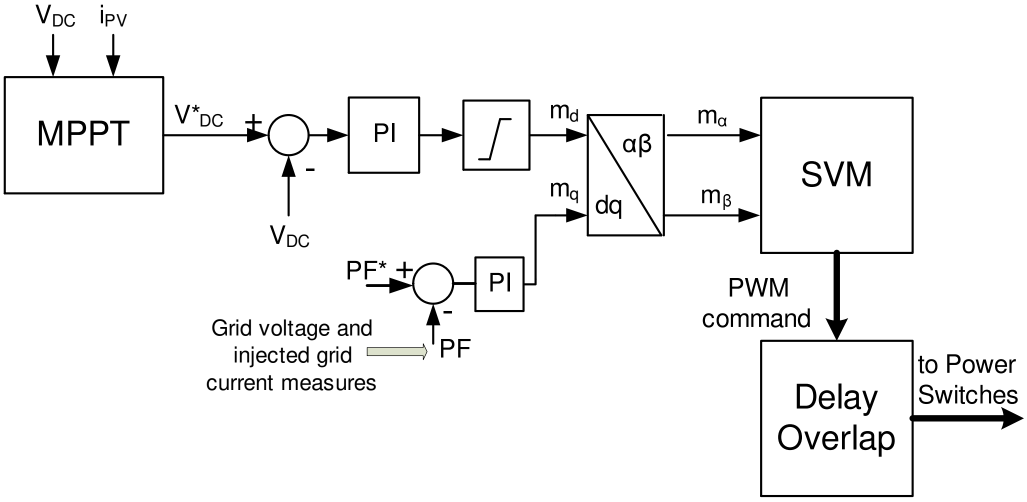

Figure 28: Schematic of the proposed control.

to determine the polar coordination of the current space vector: module $m = \sqrt{m_\alpha^2 + m_\beta^2}$ and angle $\theta = arctg\frac{m_\beta}{m_\alpha}$. Equation 2.6 shows the calculation of the normalized time intervals of the two active states which border the current space vector, where θ_1 is the angle of the current space vector referred to the active state vector placed in clockwise respect to it (see Fig. 22).

$$\begin{cases} d_a = 2/\sqrt(3) m \sin\left(\frac{\pi}{6} - \theta_1\right) \\ d_b = 2/\sqrt(3) m \sin\left(\frac{\pi}{6} + \theta_1\right) \end{cases} \tag{2.6}$$

2.2 Simulations

The proposed topology and modulation control strategy was numerically modeled in Matlab Simulink environment, employing Plecs plugin for the power converter stage. The simulated system incorporated a PV array and the power converter architecture shown in Fig. 21. The control of the CSI7 converter was implemented as shown in Fig. 28. For simplicity m_q was fixed to zero.

Two sets of simulations were carried out in order to verify the effectiveness of the proposed SVM in terms of injected grid current distortion and the evolution of the semiconductor power losses with photovoltaic sources of different power ranges.

Table 3 summarizes the parameters of the first set of simulation. In order to validate the effectiveness of the proposed SVM, the simulations were made in the worst scenario, i.e. with a very low input voltage and with a line-to-line grid voltage equal to 400V. The PV set-point voltage was fixed equal to $v_{DC}^* = 38.5V$, corresponding to MPP operating condition of a typical crystalline PV module. The simulations were conducted using the mathematical model of a PV module (classic non-linear current source characteristic) over a solar irradiation range from 0% to 100%.

Table 3: Simulation parameters for the validation of the proposed SVM.

Name	**Description**	**Value**	**Unit of Measurement**
V_{mpp}	PV panel MPP voltage	38.5	V
I_{mpp}	PV panel MPP current	6	A
V_g	rms line-to-line grid voltage	400	V
T_g	grid period	20	ms
T_s	Switching period	40	μs
t_{ov}	Overlap time	1	μs
L_{DC}	Input inductance	2	mH
C_{DC}	Input capacitance	10	μF
L	AC Filter inductance	1	mH
C	AC Filter capacitance	470	nF

Figures 29 and 30 show the waveforms of the injected grid currents with the Alternated switch sequence respectively without the overlap compensation and without the change in the SV sequence for odd and even sextants: as it can be seen, in both cases the current distortion is not acceptable. Figure 31 shows the injected grid currents with the proposed SVM strategy: in this case the waveform distortion is drastically reduced. It is important to stress that no active damping techniques were used neither in simulations nor in experiments. As shown, the overlap time compensation is mandatory when the modulation index reach such small values, e.g. $m \approx 0.067$ with an input voltage equal to 38.5 V.

As stated before, by introducing the overlap time with S_7 in the alternate commutation sequence, S_7 is active during every turn-on and turn-off transient of the reverse-blocking switches (S_1 to S_6). As a consequence, all the commutations of S_1 to S_6 happen under zero current (ZCS), as all the input DC current flows on S_7. Figure 32 shows that under these operating conditions S_7 is the only device operating under hard switching.

The second set of simulations were conducted in order to show the evolution of the semicon-

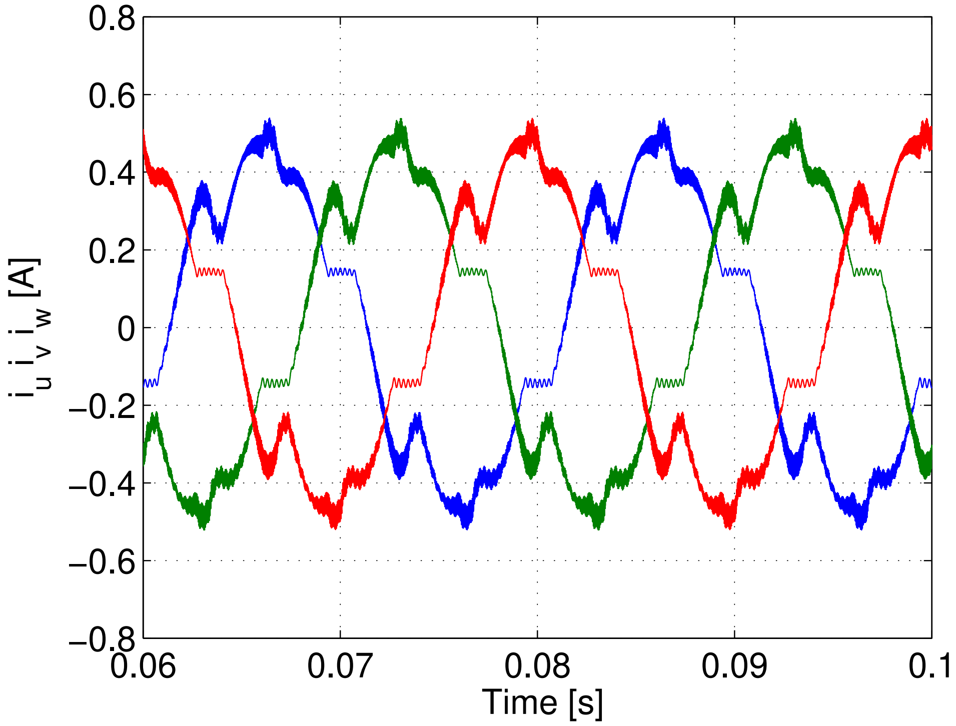

Figure 29: Injected grid currents. Alternated PWM without overlap compensation.

ductor power losses in case of wide power range photovoltaic source, in particular in presence of an increasing number of PV modules connected in series, to assess the operation of the CSI7 architecture as a modular string inverter.

The conduction and switching power losses were extrapolated from the datasheets of the CoolMos Mosfet SPB17N80C3 and the Sic Diode C2D10120A. The power losses were computed for a large range of switching voltages and currents applying the method described in [24] and inserted in the simulations by the thermal modeling used in Plecs plugin.

Table 4 shows the percentage decrease of semiconductor power losses along with the input voltage increase in presence of a constant input DC current (PV modules connected in series). Since losses are dependent strongly on current flowing through the power devices, the percentange of semiconductor power losses decreases as the DC input voltage increases. The efficiency of the proposed solution and its comparison with the traditional CSI converter will be shown in the section devoted to Experimental Results .

Finally, figures 33 and 34 show the waveforms of the common-mode voltage in case of classical CSI solution and in case of the proposed solution. It is to pointed out that the result is consequence of the null vector applied by S7 alone, while all the other transistors are turned

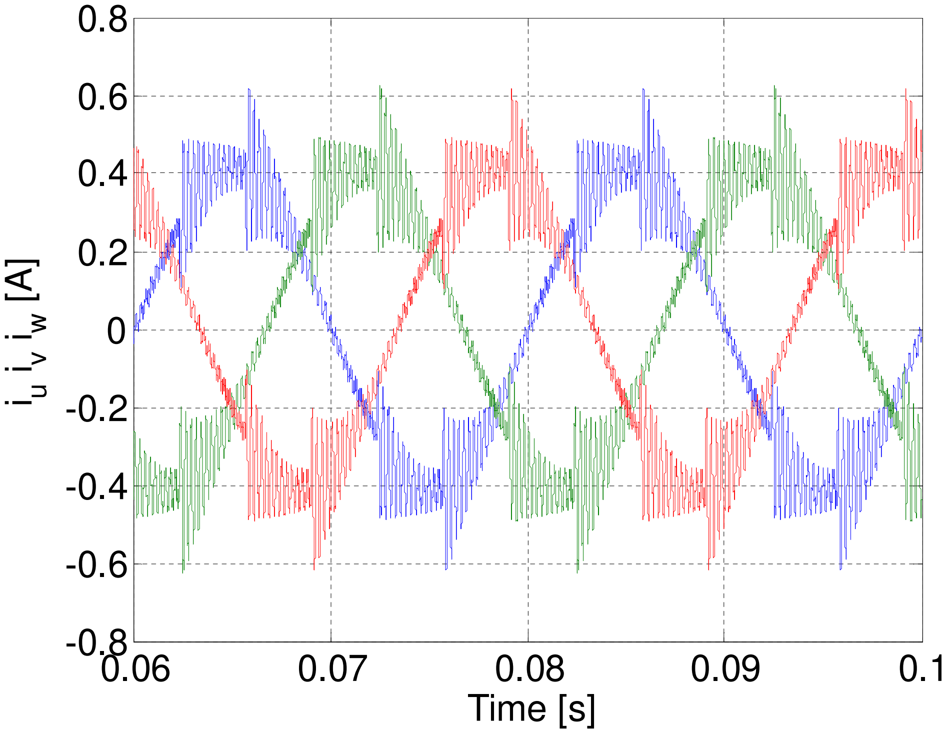

Figure 30: Injected grid currents. Alternated PWM without the change in the SV sequence for odd and even sextants.

Off. Without this extra commutation of the bridge the v_{cm} waveform is equal to the classical CSI solution: if v_{cm} does not pose an issue then for the sake of efficiency this extra commutation can be omitted.

As it can be seen, for instance, during the application of an injected current vector which is inside the sector I, the v_{cm} evolution in case of unity power factor operation is $-v_v/2$ (I_1 vector), $-v_w/2$ (I_4 vector) and $v_u/2$ (I_7 vector) in case of traditional CSI solution with base SVM, instead in case of CSI7 solution during the application of the zero vector $v_{cm} = 0$. The following section will confirm the advantages of this solution in terms of leakage current mitigation, with the direct measurements of the ground leakage current by means of an experimental test setup.

2.3 Experimental Results

A laboratory prototype was built to evaluate all the theoretical assumptions. A TMS320F28069 controller was used to implement the space vectors modulations of the traditional CSI and of the proposed CSI7. In addition to this, all the algorithms for the injection of electric power into the grid were implemented, only the MPPT algorithm was not developed since is out of

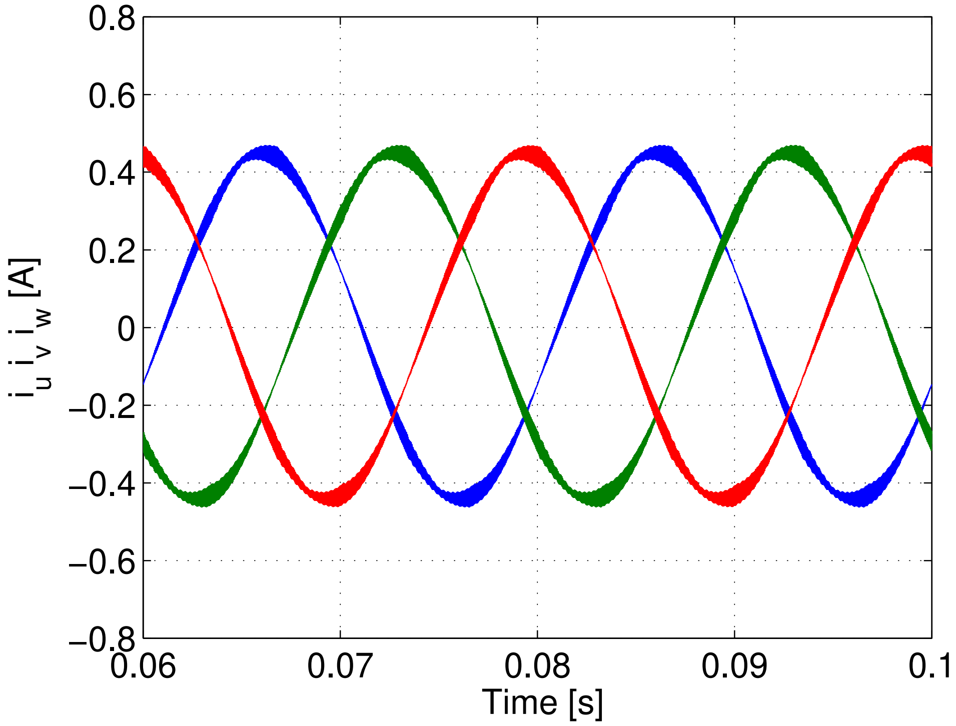

Figure 31: Injected grid currents. Alternated PWM with proposed PWM strategy and overlap compensation.

the scope of the work.

The experimental setup is shown in Figure 35. The CSI7 was connected to a variable DC Voltage Source. A three-phase transformer was connected between the grid and the outputs of CSI7. The neutral of the transformer secondary winding was connected to earth through the resistance R_g, which simulate the ground resistance of a three-phase grid. An equivalent capacitor simulates the parasitic capacitance to earth of PV panels and it was connected between the ground and the negative pole of the DC voltage source. Through this equivalent capacitor and R_g flows the ground leakage current of the PV system. A Digital Power Analyzer PPA 5530 was used for harmonic analysis and efficiency measurements.

Table 5 summarizes the conditions of the experimental tests.

The power switches used in the converter prototype are the commercial IGBT IHY15N120R3 1200V 15A. To further reduce conduction power losses, a SiC Mosfet can be used for S7. It is important to put in evidence that the power semiconductors were not chosen in order to maximize the efficiency. The measure of the efficiency should be mainly considered only as performance comparison of different modulation strategies running on the same hardware.

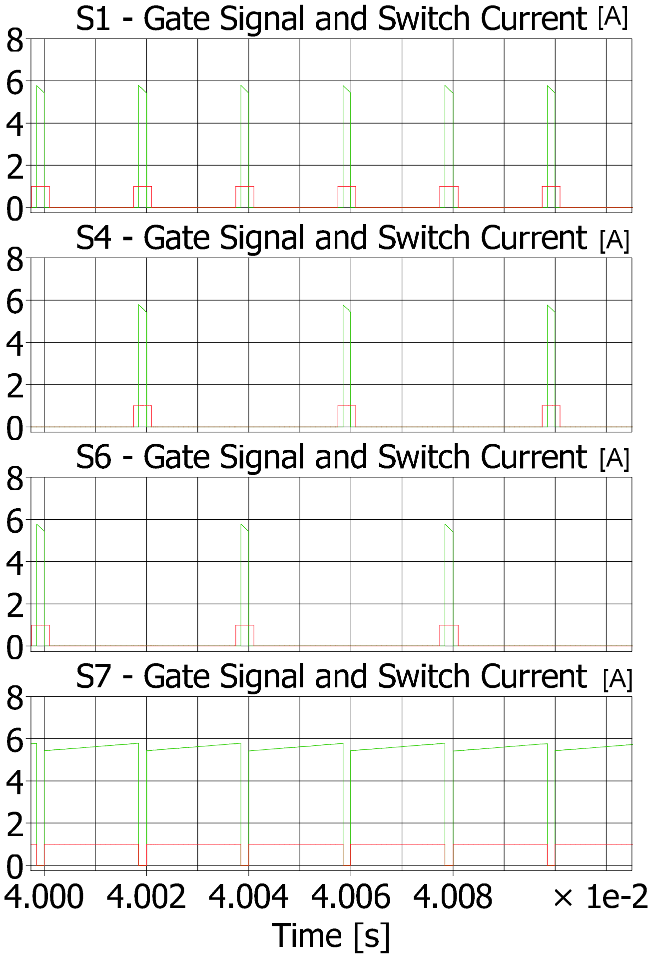

Figure 32: Effect of S_7: ZCS commutations of S_1 to S_6

Figure 36 shows a picture of the power board of the laboratory prototype. The input inductor L_{DC} was split in two input inductors in order to obtain a better performance in terms of output common-mode voltage and therefore lower ground leakage current [7].

The first part of experimental tests was conducted in order to verify the effectiveness of the proposed SVM for CSI7 topology, in particular the overlap compensation and the alternated sequence in the odd and even sextants.

The performance of the proposed solution was compared to the classic CSI topology driven by the base SVM: this represents the reference case. Figure 37 shows the grid voltage and current corresponding to 348 W of injected electric power. The THD of the injected current was measured equal to 11%.

The effectiveness of the proposed SVM for the CSI7 topology was proved through the following tests. For a fair comparison with respect to the previous reference case, the same value of injected electric power was used, i.e. 348 W. Figure 38 shows SVM performance when the

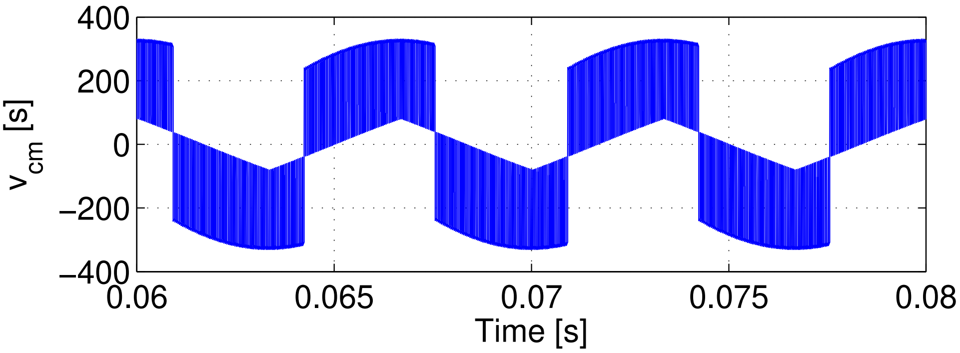

Figure 33: v_{cm} waveform in case of classical CSI solution.

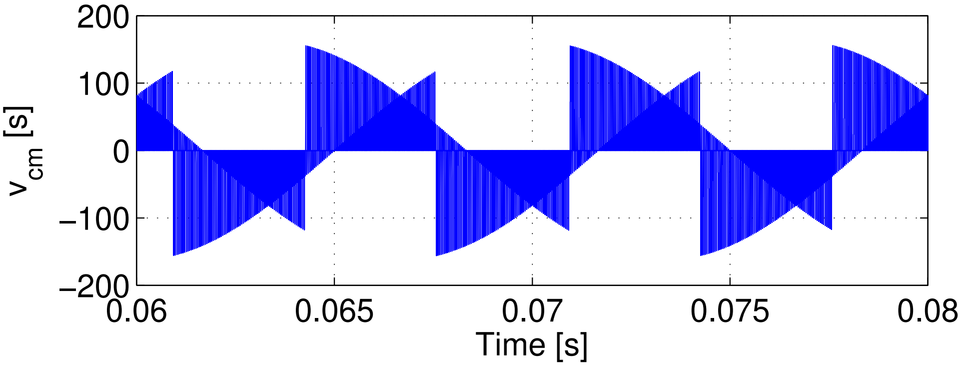

Figure 34: v_{cm} waveform in case of proposed CSI7 solution.

overlap compensation was not applied, while in Fig. 39 the inversion sequence was not applied. The THD of the injected currents result 8.9% and 11.5% respectively.

Eventually, figure 40 shows the performance of the complete SVM reaching a THD=4.5%.

Figure 41 shows the good dynamic response of CSI7 in case of step variation of the injected grid current, obtained with a step variation of the modulation index m_d.

The purpose of the second part of experiments is the evaluation of the ground leakage current issue of the CSI7 solution compared against the traditional CSI topology.

Under the same operating conditions of Table 5 the figures 42 and 43 show the ground voltage and ground leakage current. It is important to notice the strong reduction of the ground voltage (the V/div is different in the two oscilloscope captures) across C_{PV} which determines the ground leakage current. In spite of the small value of the parasitic capacitance used in the experiments, a reduction of RMS ground leakage current appears from 6.50 mA to 2.44 mA. In any case the CSI7 topology is not recommended for transformerless applications with thin film PV panels, typically characterized by a large parasitic capacitance to ground (up to $1uF/kWp$

Table 4: Semiconductor power losses (in percentage) with different MPP voltage in case of constant input DC Current equal to 6A.

V_{PV} **at MPP** $[V]$	**Input Power** $[W]$	**Semiconductor Power Losses** $[\%]$
38.5	230	8.56%
54	324	6.39%
74	444	4.95%
100	600	3.93%
150	900	2.98%
200	1200	2.50%

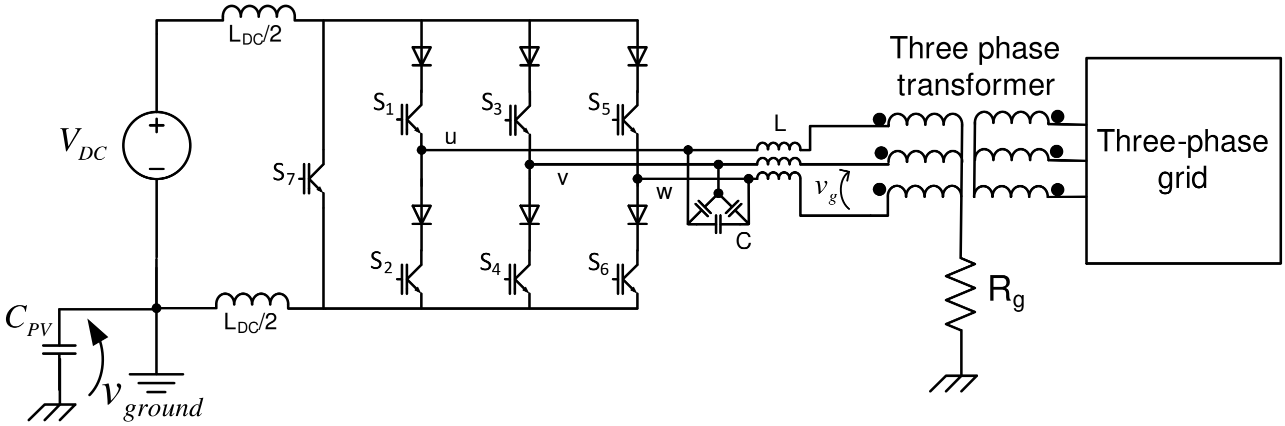

Figure 35: Experimental test setup.

Table 5: Experimental parameters.

Name	**Description**	**Value**	**Unit of Measurement**
V_{DC}	DC voltage source	60	V
V_g	rms line-to line grid voltage	230	V
f_g	grid frequency	50	Hz
f_s	Switching frequency	10	kHz
t_{ov}	Overlap time	2	μs
L_{DC}	Input inductance	2	mH
L	AC Filter inductance	440	μH
C	AC Filter capacitance	1	μF
C_p	equivalent PV parasitic capacitance	2.7	nF
R_g	ground resistance	4.7	Ω

for building integrated thin film PV modules).

Figure 44 shows the experimental comparison efficiency of the CSI7 solution and traditional

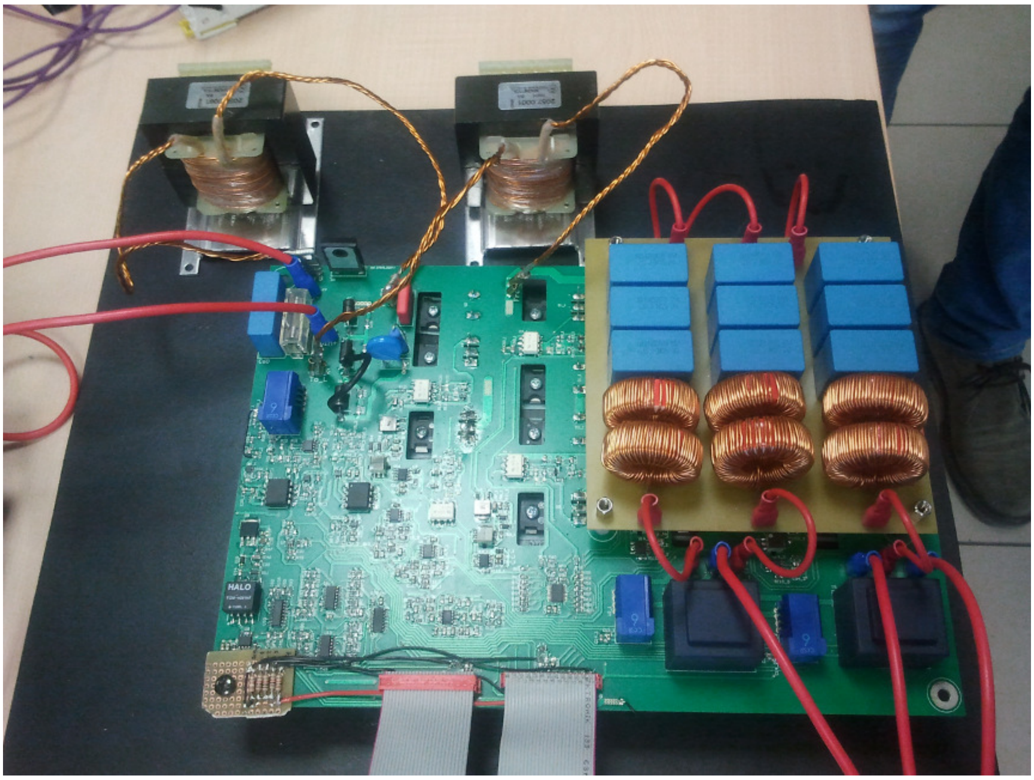

Figure 36: Power board of CSI7 laboratory prototype

CSI. In case of different input power and with a DC input voltage equal to 60V the efficiency difference results very large. This behavior was expected since in case of a relatively small DC input voltage the time interval in which one leg is short circuited is predominant during every PWM period. The same figure shows also the efficiency of the proposed solution with an higher DC input voltage, $V_{DC} = 210V$. Despite the power semiconductor devices were not chosen for efficiency maximization, the absolute efficiency results almost acceptable for actual PV systems in this last case.

2.4 Conclusion

A grid-tied three-phase CSI with innovative architecture and modulation strategy was modeled and simulated. The effectiveness of the proposed CSI7 topology and adopted SVM was compared against the traditional CSI solution by means of simulations and experiments.

Results show that CSI7 inherent step-up capability can be exploited to achieve a grid-connected single-stage in case of a very large variation of input DC voltage, as low as a single crystalline PV module.

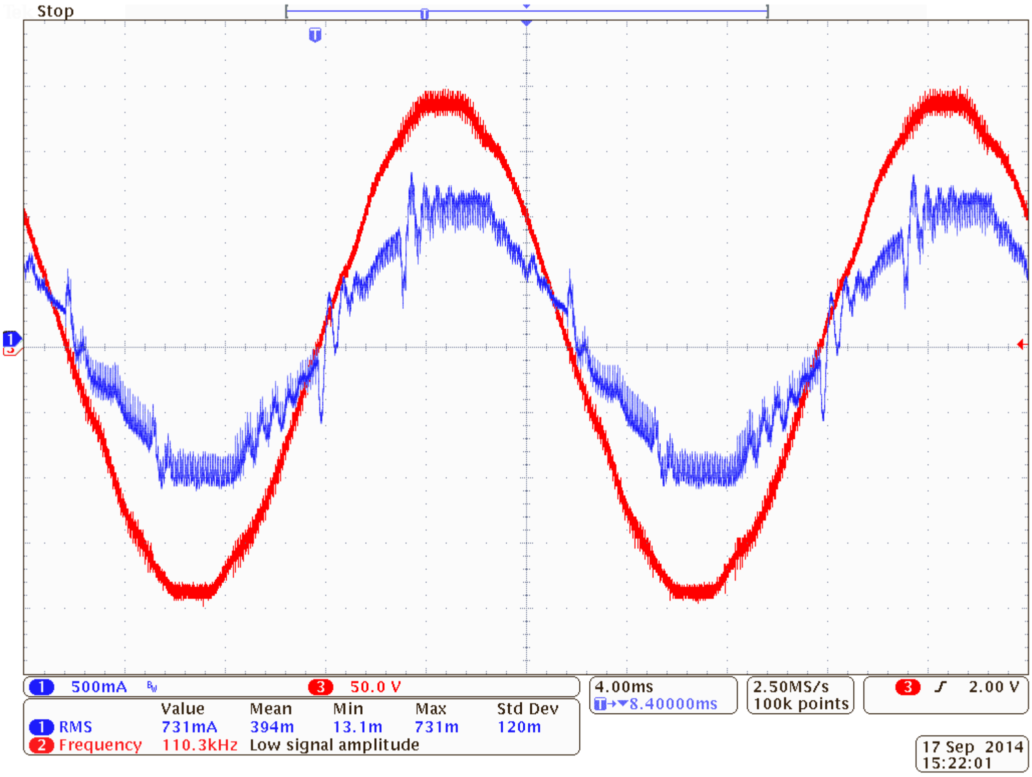

Figure 37: Experimental results. Phase grid voltage (50V/div) and injected current (0.5 A/div, THD 11%) in case of base SVM.

The benefits and the critical issues of CSI7 topology are exposed. It presents an additional power switch with respect to the traditional CSI solution in order to strongly reduce conduction semiconductor power losses. The additional switch S7 can be a simple Mosfet or Igbt (without reverse blocking capability) if the power factor operation is reasonably close to unity. In the proposed SVM the null output vector is obtained by switching on S7 while concurrently switching off the entire bridge: the higher commutation count is counterbalanced by the benefits obtained. In fact the proposed CSI7 solution is able to:

- minimize the THD of the injected grid current;
- attenuate the excitation of the output CL filter of the CSI without the use of any passive or active damping solutions
- reduce the common mode voltage variations with respect to ground thus reducing the ground leakage current
- reduce the conduction power losses
- allow the commutations of S_1 to S_6 to happen under zero current (ZCS)

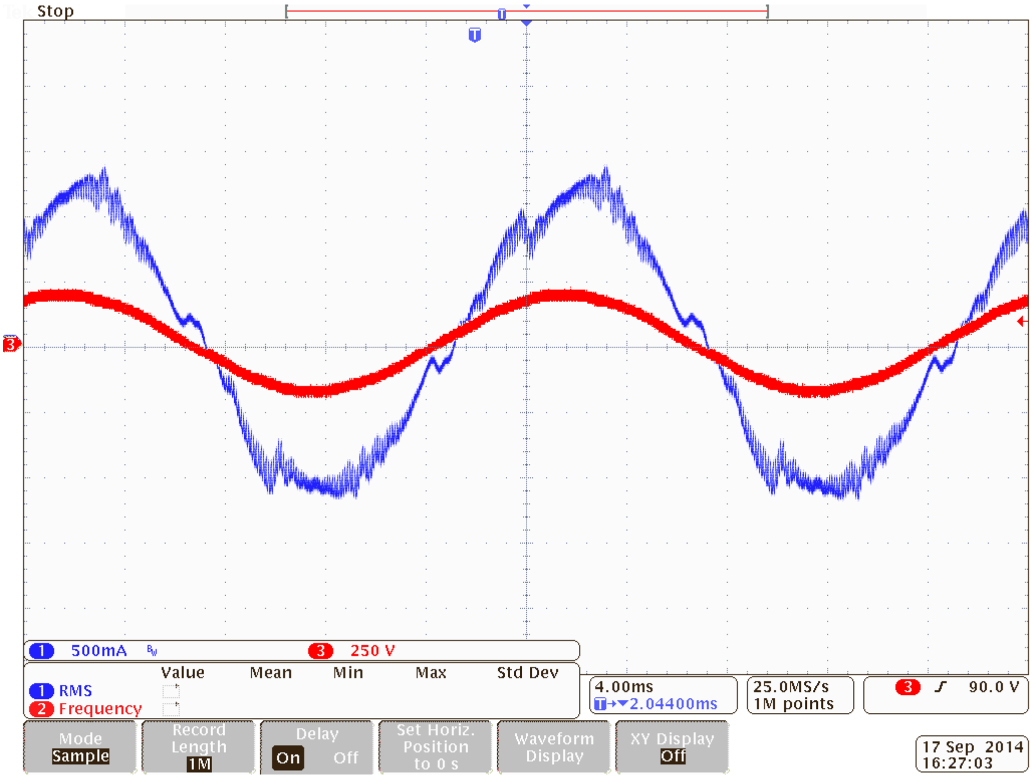

Figure 38: Experimental results. Phase grid voltage (250V/div) and injected current (0.5 A/div, THD 8.9%) in case of proposed SVM for CSI7 topology without overlap compensation.

The experiments proved that the topology is feasible in wide power range String Converter applications, all the way down to single-module converter. It is however more versed to high power applications, as shown by the power losses analysis and measured efficiencies. In particular the experimental results showed the improvements of the proposed solution in terms of injected current THD and conversion efficiency with respect to traditional CSI solution. Finally the lower excitation of the common-mode resonant circuit caused by the parasitic capacitance of PV panels with respect to traditional CSI solution was demonstrated. This implies that under the same operating conditions and as shown in the experiments, the CSI7 architecture and proposed SVM is characterized by a lower ground leakage current.

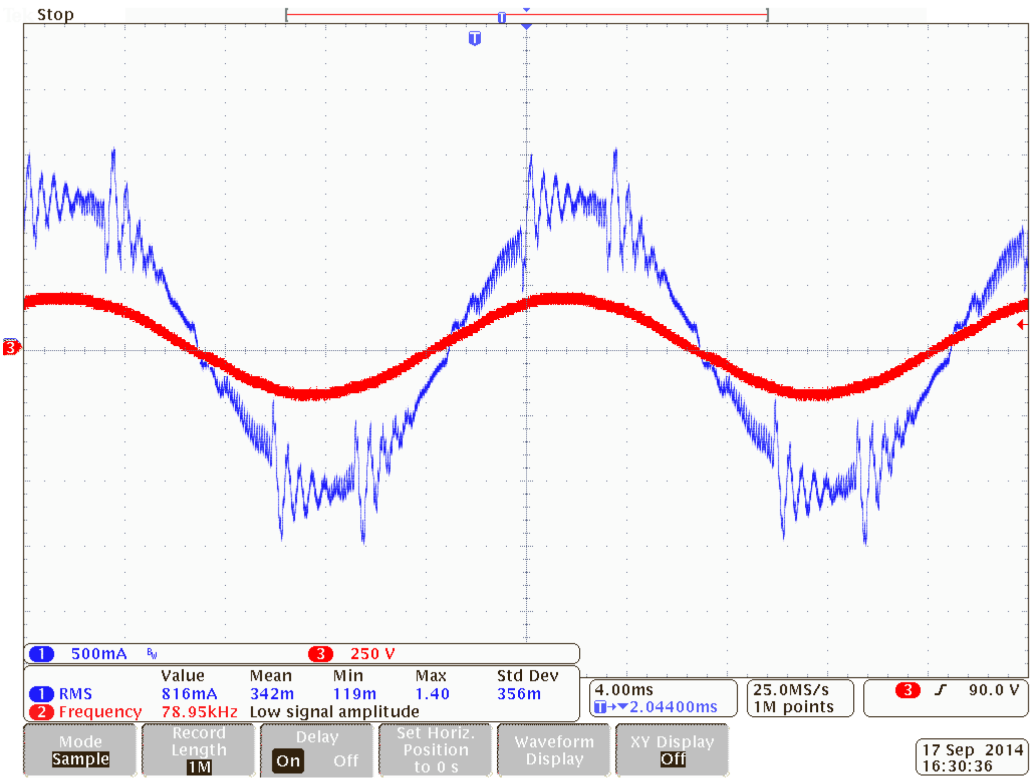

```
              Value     Mean   Min    Max    Std Dev
1 RMS         816mA     342m   119m   1.40   356m
2 Frequency   78.95kHz  Low signal amplitude
```

Figure 39: Experimental results. Phase grid voltage (250V/div) and injected current (0.5 A/div, THD 11.5%) in case of proposed SVM for CSI7 topology without the inversion sequence.

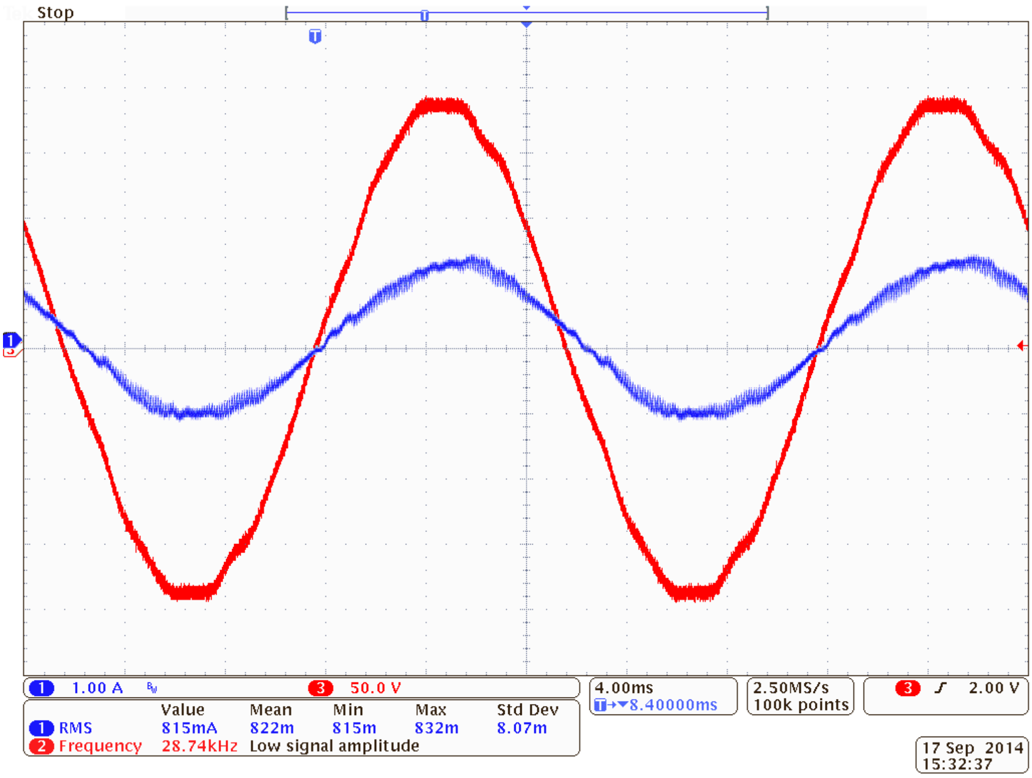

```
              Value     Mean   Min    Max    Std Dev
1 RMS         815mA     822m   815m   832m   8.07m
2 Frequency   28.74kHz  Low signal amplitude
```

Figure 40: Experimental results. Phase grid voltage (250V/div) and injected current (0.5 A/div, THD= 4.5%) in case of the complete proposed SVM for the CSI7 topology.

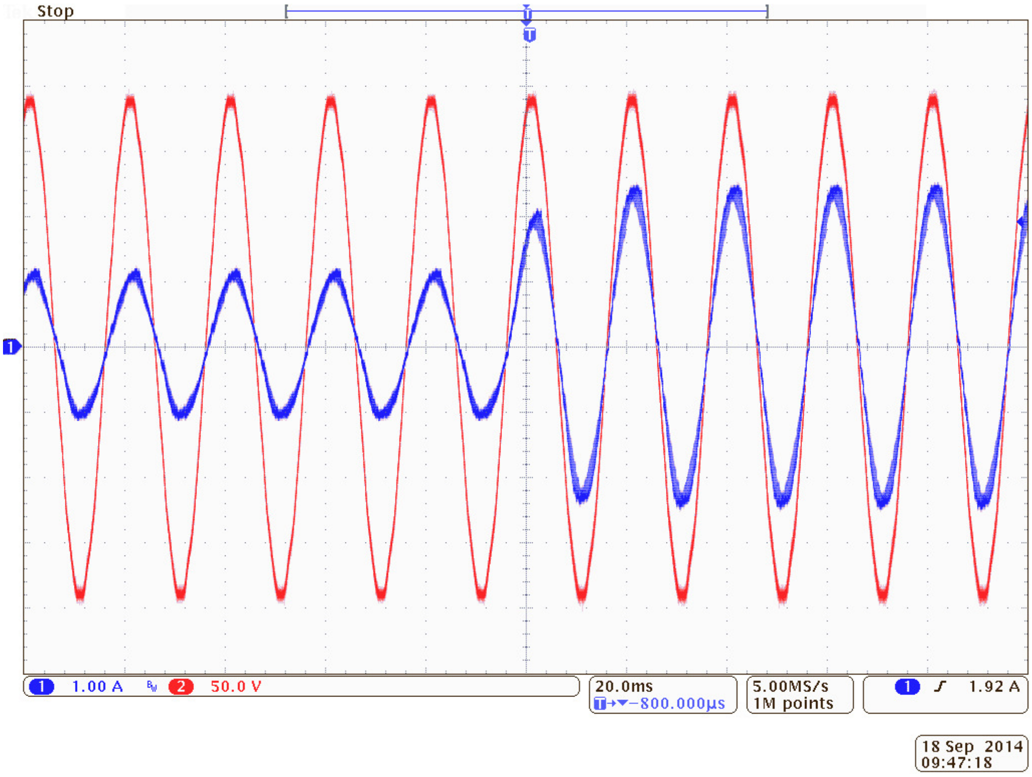

Figure 41: Experimental results. Step variation of the injected grid current (1A/div). The figure shows only one phase current and grid voltage.

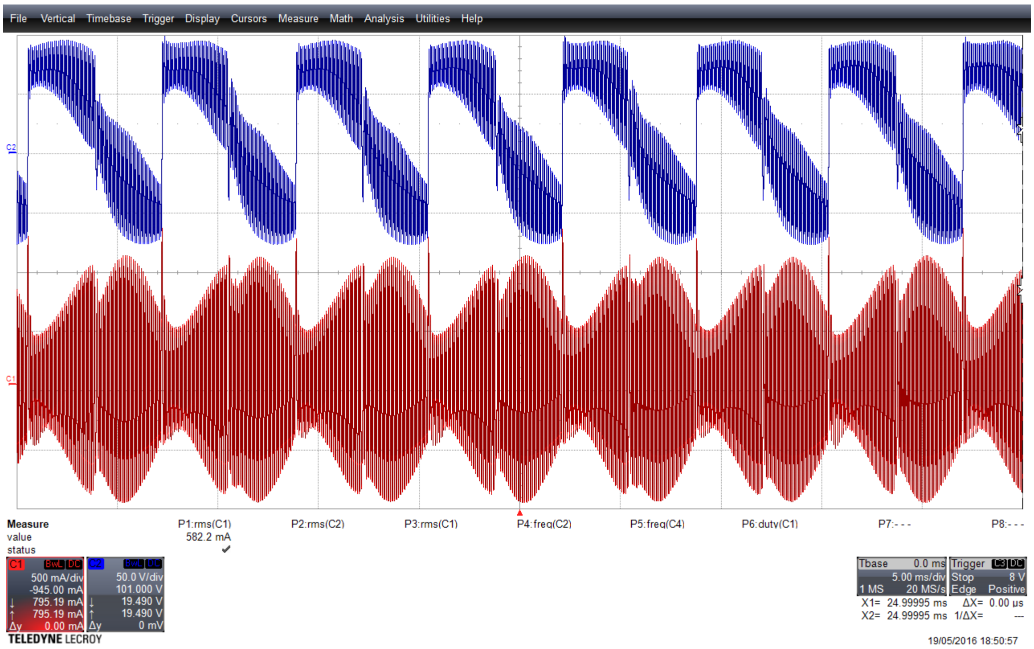

Figure 42: Experimental results. Ground voltage (250V/div) and ground leakage current (50mA/div) in case of base SVM for traditional CSI topology.

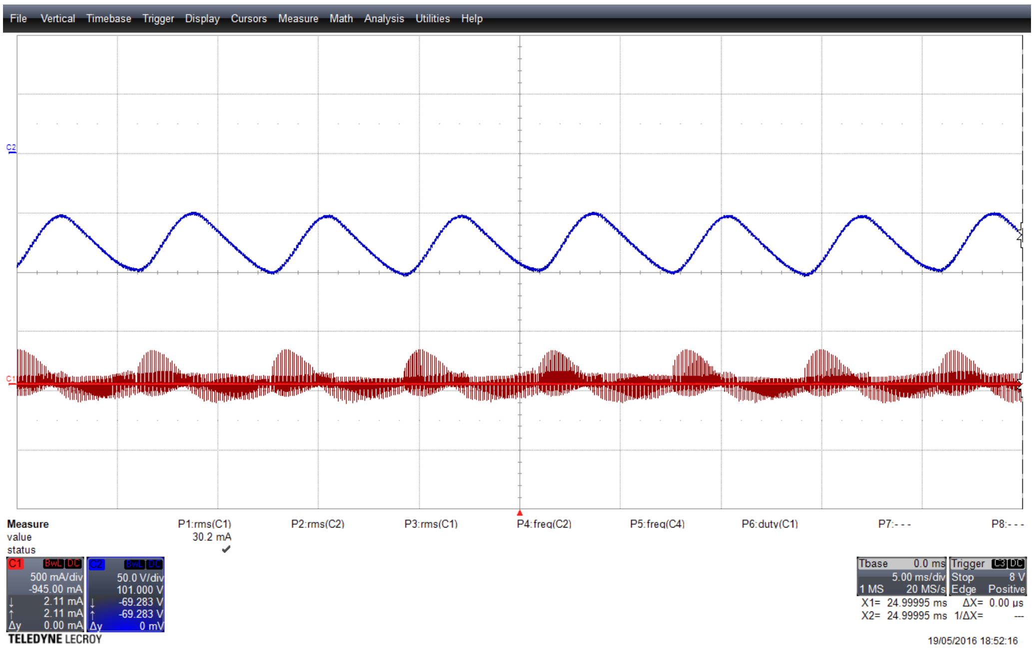

Measure P1:rms(C1) P2:rms(C2) P3:rms(C1) P4:freq(C2) P5:freq(C4) P6:duty(C1) P7:- - - P8:- - -
value 30.2 mA
status ✓

C1 BwL DC
500 mA/div
-945.00 mA
↓ 2.11 mA
↑ 2.11 mA
Δy 0.00 mA

C2 BwL DC
50.0 V/div
101.000 V
↓ -69.283 V
↑ -69.283 V
Δy 0 mV

Tbase 0.0 ms
5.00 ms/div
1 MS 20 MS/s

Trigger C3 DC
Stop 8 V
Edge Positive

X1= 24.99995 ms ΔX= 0.00 µs
X2= 24.99995 ms 1/ΔX= ---

19/05/2016 18:52:16

Figure 43: Experimental results. Ground voltage (50V/div) and ground leakage current (50mA/div) in case of proposed CSI7 solution.

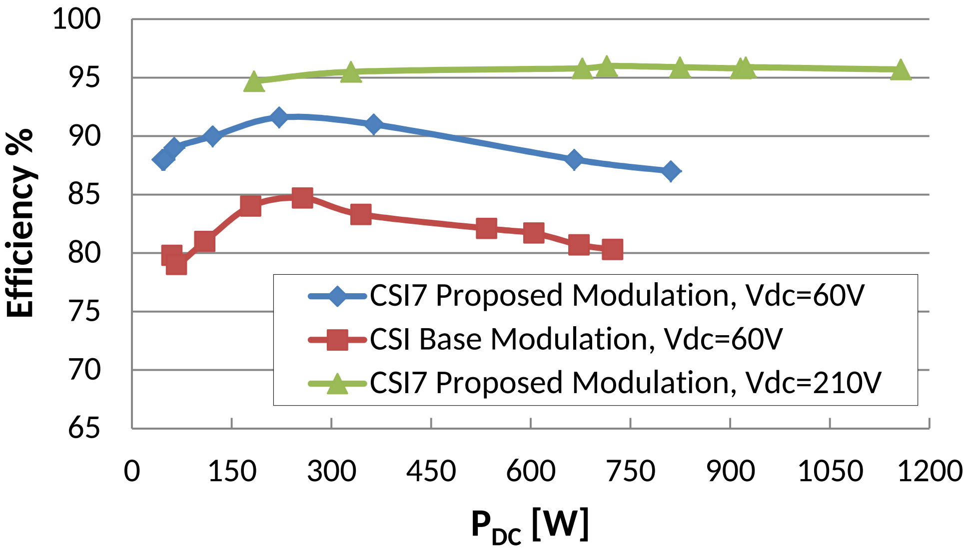

Figure 44: Experimental results. Efficiency comparison between CSI7 solution and traditional CSI solution.

3. Saturation Model in Internal Permanent Magnet Machines for Optimal Control Strategies

In this chapter the importance of a good model of the behaviour of Internal Permanent Magnet (IPM) machines is examined with a particular care to the research of the optimal control strategies. A model which takes into account the saturation and, in general, the non linear behaviour of the IPM machine is fundamental when the control strategies must be implemented to obtain a good performance of the machine.

In the end, an optimized algorithm which can find the optimal control strategies from the non linear model of the machine is presented and simulations results are discussed.

3.1 IPM motors and control trajectories

Recently, interior permanent-magnet (IPM) synchronous machines have become more and more popular in different transportation applications, such as automotive [31],[32],[33],[34], aerospace [35] and marine [36]. The key to their success is the combination of high torque density and wide speed range. The former can be achieved thanks to permanent-magnets and the latter thanks to high inductances and saliency ratio greater than the unity.

Specifically, the high-speed range can be achieved by accurate control strategies: Maximum Torque per Ampere (MTPA), Flux Weakening (FW) and Maximum Torque per Volt (MTPV) [37], [38], [39]. These control strategies are trajectories on a *d*-*q* reference plane where the operating regions are bounded by a Current Limit Circle (CLC) and Voltage Limit Ellipses (VLE), as shown in Figure 45. The *d*-*q* plane is obtained by Clarke's and Park's transformations of the electrical quantities.

The accuracy of these control strategies is strongly dependent on the knowledge of the machine's magnetic model and drive's parameters, such as DC BUS voltage and current rating. Moreover, such strategies are generally based on linear assumptions, i.e. considering L_d and L_q as constant parameters [40].

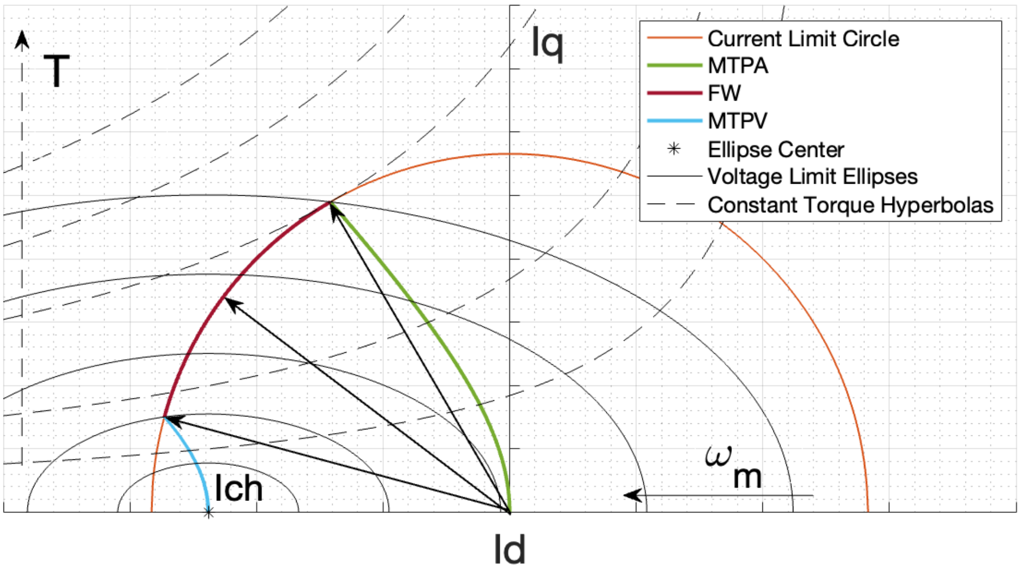

Figure 45: MTPA, FW and MTPV trajectories on d-q reference frame.

As known, the classic d-q reference frame IPM machine model might be unreliable in predicting the performance in case of iron saturation [41],[42],[43].

Several papers investigated solutions to overcome the aforementioned shortcomings. In [44] the maps of flux linkages λ_d and λ_q are computed by Finite Element Analysis (FEA) and used to compute MTPA and iso-torque curves. In [45], a nonlinear model including saturation, cross-coupling, spatial harmonics and temperature effects is proposed. In [46] and [47], an accurate machine model is proposed that relies on look-up tables populated by FEA and including temperature variations. In [48] and [49], an interesting, though simplified analytical approach is shown to compute the MTPA curve by mapping L_d, L_q and λ_{pm} by FEA. In [50] and [51], the MTPA curve is analytically computed with respect to q-axis current. In [52], [53] and [54], FEA is used to compute flux linkages on d- and q-axis as a function of current. In [55] a lumped-parameter model was developed, while in [56] a model-based correction method using stator flux adjustment is proposed.

Authors in [57] and [58] propose an analytical model which considers saturation saliences for the estimation of inductances value in permanent-magnet synchronous machine (PMSM). The model was validated numerically and experimentally and good results were obtained for PMSM machines. The proposed model can be used for different machines and, in particular, it can be very useful in IPM synchronous machines, where saliency's influence is higher. In [59] a different model which considers saturation and cross-coupling is proposed with the purpose of obtaining analytically inductance values and MTPA trajectory; this model was validated numerically with simulations considering an IPM-SM system. Another solution to include magnetic saturation in the control algorithm is to use the Extended Kalman Filter (EKF) [60], which perform a good estimation of the currents and inductances. EKF is an optimal estimation method for nonlinear systems, in which the state's estimation is obtained starting from its value and covariance matrix at the previous moment, that are updated basing on measured values. A good estimation of machine parameters is useful for sensorless control applications [61], where a good analytical model of the machine is needed to obtain a good estimation of rotor's position.

This chapter proposes a new approach based on a set of algorithms to obtain an accurate prediction of the electric machine behaviour considering nonlinear magnetic model. The possible variation of the permanent-magnet flux will not be taken into account in this model because in the design process of the electric machine, the permanent magnet operating point can be set according to the working temperature and thus considering the worst operating condition.

A reference IPM synchronous machine was chosen to assess the proposed method. Its parameters are listed in Table 6. The machine's equivalent inductances have been computed by means of 2-D Finite Element Analysis (FEA) and simulations were performed with different values of the stator currents in order to obtain complete maps of the L_d and L_q inductances in the d-q reference frame. Two different 2-D FEA methods were adopted to model magnetic nonlinearities and obtain equivalent inductances' maps: a standard magnetostatic method and Frozen Permeability (FP) method. Then, the two methods were compared in terms of control trajectories.

FP method allows to obtain motor's parameter operating under saturated conditions, taking into account the effect of the permanent magnets even when they are turned off (this is necessary to avoid the permanent magnets contribution to the flux linkage in the inductance computation). Authors in [62] use FP to separate permanent magnets and reluctance torque components [63] of a spoke-type IPM machine in order to optimize the control design. Basing on the proposed model, Wu et al. implemented an optimization process which allows to obtain a larger torque density; FEA and FP results were compared to prove the advantages coming from the application of the proposed optimized model. In [64], FP is used to provide an accurate inductance model of a variable-flux permanent magnet machine and the results are compared with experimental measurements showing a good correspondence. Frozen permeability can also be used to find a d-q model under saturated conditions, as shown in [65], since the classic model does not take into account saturation and cross magnetization; thanks to FP method these factors can be included in the model, ensuring a good representation of the machine's magnetic behaviour. In general, FP method can be used to do a magnetic field analysis of the machine under saturated conditions [66]. Anyway all these references do not provide methods or analytical solutions to compute MTPA, MTPV and FW trajectories and corresponding isotropic curves.

Starting from the maps of the equivalent inductances, a series of algorithms were developed in order to compute the operating points of MTPA, FW and MTPV trajectories, Voltage Limit Ellipses (VLE) and Constant Torque Hyperbolas (CTH).

3.2 Optimal Strategies in the Linear Model

Eq. 3.1 reports the IPM machine voltage equations in the rotating *d*-*q* reference frame and synchronous with the rotor's speed.

$$\bar{v}_{dq} = R\bar{i}_{dq} + \frac{d}{dt}\left(\bar{\lambda}_{dq}\right) + jp_p\omega_m\bar{\lambda}_{dq} \tag{3.1}$$

where:

- R: phase resistance;
- $\bar{v}_{dq}$: voltage vector;
- $\bar{i}_{dq}$: current vector;
- ω_m: mechanical speed;
- p_p: pole pairs number;
- $\bar{\lambda}_{dq} = \bar{L}_{dq}\bar{i}_{dq} + \bar{\lambda}_{pm,dq}$: flux linkage vector;
- $\bar{\lambda}_{pm,dq} = \begin{bmatrix} \lambda_{pm} \\ 0 \end{bmatrix}$: flux linkage due to PM;
- $\bar{L}_{dq} = \begin{bmatrix} L_d & 0 \\ 0 & L_q \end{bmatrix}$: inductance matrix.

Eq. 3.1 can be split in two scalar equations for d and q axes as:

$$v_d = Ri_d + L_d \frac{d}{dt}\left(i_d\right) - p_p \omega_m L_q i_q \tag{3.2}$$

$$v_q = Ri_q + L_q \frac{d}{dt}\left(i_q\right) + p_p \omega_m \left(L_d i_d + \lambda_{pm}\right) \tag{3.3}$$

Neglecting the voltage drop across the resistance and considering steady-state operation, torque can be expressed as:

$$T = \frac{3}{2} p_p \left[\lambda_{pm} i_q + i_d i_q \left(L_d - L_q\right)\right] \tag{3.4}$$

The operating limits of the machine can be identified as curves in the *d*-*q* plane: the current limit is identified by a circle, Eq. 3.5, and the voltage limit due to DC bus voltage can be expressed as in Eq. 3.6.

$$i_d^2 + i_q^2 = I_{lim}^2 \tag{3.5}$$

$$v_d^2 + v_q^2 = V_{lim}^2 \tag{3.6}$$

In steady-state, the voltage limit can be represent with an ellipse in the *d*-*q* reference plane, Eq. 3.7, by replacing Eq. 3.2 and Eq. 3.3 in Eq. 3.6 and neglecting the resistance drop.

$$\frac{\left(I_d + \frac{\lambda_{pm}}{L_d}\right)^2}{\left(\frac{V_{lim}}{p_p\omega_m L_d}\right)^2} + \frac{I_q^2}{\left(\frac{V_{lim}}{p_p\omega_m L_q}\right)^2} = 1 \tag{3.7}$$

where capital letters stand for stationary values.

The center of the ellipses is $[I_{ch}; 0]$, where I_{ch} is referred to as the *characteristic current* of the machine that can be obtained with Eq. 3.8.

$$I_{ch} = -\frac{\lambda_{pm}}{L_d} \tag{3.8}$$

The allowed operating region of the machine is defined by the intersection of the internal areas of the two curves of Eq. 3.5 and Eq. 3.7, i.e. the Current Limit Circle (CLC) and the Voltage Limit Ellipses (VLE) of Figure 45.

It is useful to express steady-state components I_d and I_q as a function of the current space vector amplitude I and phase γ as in Eq. 3.9.

$$\begin{cases} I_d = Isin\gamma \\ I_q = Icos\gamma \end{cases} \tag{3.9}$$

By replacing Eq. 3.9 in Eq. 3.4, torque can be expressed as in 3.10.

$$T = \frac{3}{2}p_p\left[\lambda_{pm}Icos\gamma + I^2 sin\gamma cos\gamma\left(L_d - L_q\right)\right] \tag{3.10}$$

In MTPA operations, the control acts to regulate the maximum torque for a fixed current amplitude. Considering Eq. 3.10, MTPA locus can be expressed as Eq. 3.11.

$$\begin{gathered} \tfrac{d}{d\gamma}(T/I) = 0 \\ \Rightarrow \lambda_{pm} sin\gamma + I(L_d - L_q)(sin^2\gamma - cos^2\gamma) = 0 \end{gathered} \tag{3.11}$$

The locus stated by Eq. 3.11 is based on a number of assumptions:

1. Pure sinusoidal currents and air gap magnetic field distribution;
2. No cross-coupling between the equivalent magnetic circuit and the *d-q* axes. The two axes are magnetically decoupled because they are at 90 electrical degrees;
3. No saturation effects, i.e. no variation of the inductances versus currents.

These assumptions are too restrictive for a complete model of an IPM machine, especially the last one. In fact, machine's inductances values cannot be considered constant, but they vary as a function of both current vector amplitude and phase: $L_d(I, \gamma)$ and $L_q(I, \gamma)$.

Therefore, the computation of the torque Eq. 3.11 should include the partial derivative of the inductances:

$$\lambda_{pm} sin\gamma + I \left[\frac{\delta L_d(I,\gamma)}{\delta\gamma} - \frac{\delta L_q(I,\gamma)}{\delta\gamma} \right] (sin^2\gamma - cos^2\gamma) = 0 \tag{3.12}$$

By taking into account the variation of the inductances with the operating point, it is not possible to obtain a simple analytical expression for the MTPA locus as in the previous linear model case. In addition to that, the functions $L_d(I, \gamma)$ and $L_q(I, \gamma)$ should be estimated starting from a complete map of the equivalent inductances over all the possible operating points of the machine. Similar issues occur in the computation of the other two operating modes loci: FW and MTPV.

The maximum-torque operating point lies on the intersection between the CLC and the MTPA locus, but for high speeds, also the VLE must be taken into account. In fact, MTPA operation is possible only below a certain speed referred to as *base speed*. Above the base speed, the shrinkage of the VLE causes the maximum-torque point to lie outside voltage limit, making the operating point inaccessible for steady-state operations (Figure 45). For each operating point of MTPA $(I_d; I_q)$, the base speed value can be computed as the intersection between MTPA (Eq. 3.11) and the VLE Eq. 3.7).

$$\omega_{base} = \frac{V_{lim}}{p_p\sqrt{(L_d I_d + \lambda_{pm})^2 + (L_q I_q)^2}} \tag{3.13}$$

As a consequence, when higher speeds are required, the machine must be operated in FW mode, where the maximum output torque decreases with speed. The terminal voltage and the amplitude of the current vector are kept constant at their limits V_{lim} and I_{lim}, while the phase angle is increased with the speed, thanks to the demagnetizing d-axis reaction. This trajectory can be expressed as the intersection between the CLC (Eq. 3.5) and the VLE (Eq. 3.7) as shown in 3.14.

$$\begin{cases} I_d^2 + I_q^2 = I_{lim}^2 \\ \frac{\left(I_d + \frac{\lambda_{pm}}{L_d}\right)^2}{\left(\frac{V_{lim}}{p_p \omega_m L_d}\right)^2} + \frac{I_q^2}{\left(\frac{V_{lim}}{p_p \omega_m L_q}\right)^2} = 1 \end{cases} \tag{3.14}$$

$$\Rightarrow I_d = \frac{L_d \lambda_{pm}}{L_d^2 - L_q^2}\left\{-1 + \sqrt{1 - \frac{L_d^2 - L_q^2}{L_d \lambda_{pm}^2}\left[\lambda_{pm}^2 + L_q^2 I_{lim}^2 - \frac{V_{lim}}{p_p \omega_m}^2\right]}\right\}$$

In order to take into account nonlinearities in the computation of FW strategy, the constant inductances of Eq. 3.14 should be replaced with $L_d(I, \gamma)$ and $L_q(I, \gamma)$. However, this is far too complex for a real-time implementation.

It is not possible to operate up to an arbitrarily high velocity in FW operation, but there is a FW speed limit. The maximum achievable speed corresponds to the smallest VLE touching the CLC, that can be computed from Eq. 3.7 with $I_q = 0$ and $I_d = -I_{lim}$.

$$\omega_{FW,end} = \frac{V_{lim}}{p_p(L_d I_{lim} + \lambda_{pm})} \tag{3.15}$$

However, if the characteristic current of the machine falls inside the CLC, it is possible to reach a theoretically infinite speed with MTPV operation. In this case, the optimal current vector follows the MTPV trajectory up the point $[I_{ch}; 0]$, corresponding to infinite speed and zero torque operation. In MTPV, the voltage is not sufficient to hold current to I_{lim} and the flux linkage λ must be decreased with the increase of speed, as $\lambda \approx V_{lim}/p_p w_m$. Actually, MTPV operation comes into action at the intersection point between its trajectory and the CLC (Figure 45). In fact, from that point, it is possible to obtain the same torque output for a lower current amplitude.

The computation of MTPV trajectory is easier in a new *D*-*Q* reference frame, whose origin is in the centre of the VLE. So doing, the current components become as in Eq. 3.16.

$$\begin{cases} I_D = \frac{\lambda_{pm} + L_d I_d}{L_q} \\ I_Q = I_q \end{cases} \tag{3.16}$$

By replacing Eq. 3.16 in Eq. 3.7, the VLE becomes a voltage limit circle as shown in Eq. 3.17.

$$\frac{I_D^2}{\left(\frac{V_{lim}}{p_p \omega_m L_q}\right)^2} + \frac{I_Q^2}{\left(\frac{V_{lim}}{p_p \omega_m L_q}\right)^2} = 1 \tag{3.17}$$

The new current vector in *D*-*Q* reference frame can be defined in terms of amplitude and phase as in Eq. 3.18.

$$\begin{cases} I' = \sqrt{I_D^2 + I_Q^2} = \frac{V_{lim}}{p_p \omega_m L_q} \\ \gamma' = \tan^{-1}\left(\frac{I_D}{I_Q}\right) \end{cases} \tag{3.18}$$

By replacing Eq. 3.18 into Eq. 3.4:

$$T = \frac{3}{2}\frac{V_{lim}}{\omega_m L_q}\left[\frac{V_{lim}}{p_p\omega_m}\left(1-\frac{Lq}{Ld}\right) sin\gamma' cos\gamma' + \lambda_{pm}\frac{Lq}{Ld}cos\gamma'\right] \tag{3.19}$$

The MTPV locus can be obtained from torque Eq. 3.19 with respect to the current angle in the *D*-*Q* frame:

$$\begin{gathered} \tfrac{d}{d\gamma'}(T/V_{lim}) = 0 \\ \Rightarrow (L_d - L_q)\left[(\tfrac{L_d I_d + \lambda_{pm}}{L_q})^2 - I_q^2\right] + \lambda_{pm}(\tfrac{L_d I_d + \lambda_{pm}}{L_q}) = 0 \end{gathered} \tag{3.20}$$

As for MTPA, Eq. 3.20 is based on restrictive assumptions, thus more accurate results can be achieved only including partial derivative of inductances.

In conclusion, a closed analytical formulation is possible if and only if the behavior of inductances is known as a function of the current amplitude and phase angle. Moreover, this would result in a very complex solution, not suited to real-time implementation.

This chapter proposes a viable solution taking into account the variation of L_d and L_q with the working point of the reference machine. Complete maps of the two equivalent inductances along the *d*-*q* axes are defined thanks to 2-D FEA. Then, the computation of MTPA, FW and MTPV curves follows an algorithmic approach, based on the above mentioned maps.

3.3 Finite Element Analysis for Magnetic Model Mapping

This section briefly describes the two different 2-D FEA methods employed to model the non-linear magnetic behaviour of the reference IPM machine. The geometry of the chosen reference machine is shown in Figure 46 and its parameters are listed in Table 6.

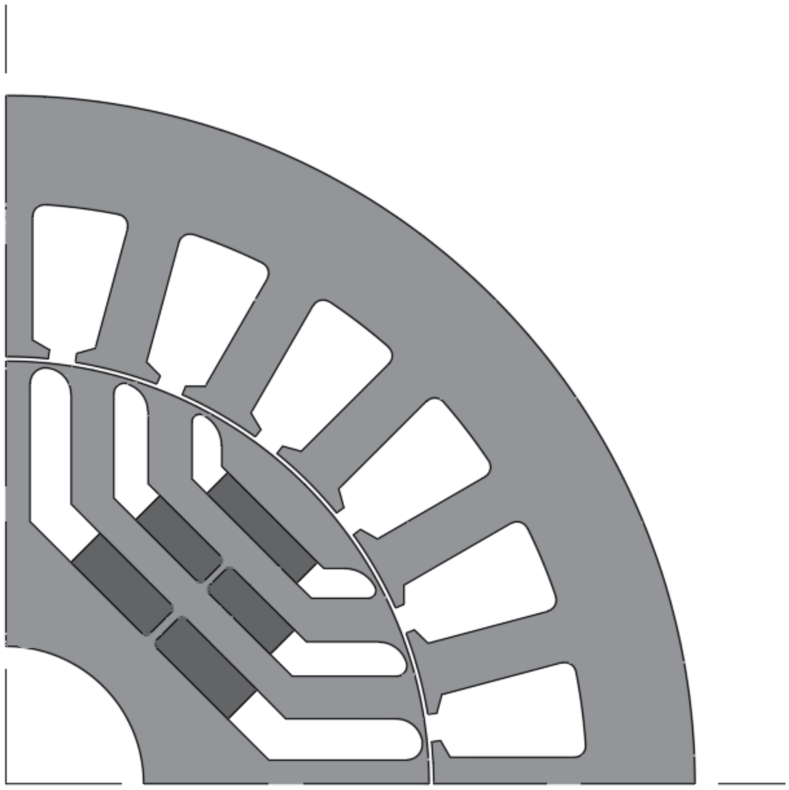

Figure 46: Geometry of the reference IPM synchronous machine.

Table 6: Main parameters of the reference IPM synchronous machine.

Parameter	**Symbol**	**Value**	**Unit**
n° of Pole Pairs	p_p	2	-
n° of Stator Slots	Q	24	-
n° of Conductors per Slot	n_c	2	-
Stack Length	L_{stk}	100	mm
Phase Resistance	R	0.0032	Ω
Flux Linkage of PM	λ_{pm}	0.0128	Wb
Rated Current	I_{lim}	400	A
Overload Current	I_{OL}	720	A
DC BUS Voltage	V_{lim}	48	V
Maximum Speed	ω_{max}	30	krpm

3.3.1 Standard Method

The first adopted method (Standard Method) is based on standard nonlinear magnetostatic simulations. Specifically, it uses only one nonlinear magnetic 2-D FEA, that includes both armature current and permanent-magnets as MMF sources. FEA simulations were performed with different values of the stator currents in order to obtain a complete map of the L_d and L_q inductances in the *d*-*q* plane.

The inductances maps for the reference machine are shown in Figure 47 and Figure 48.

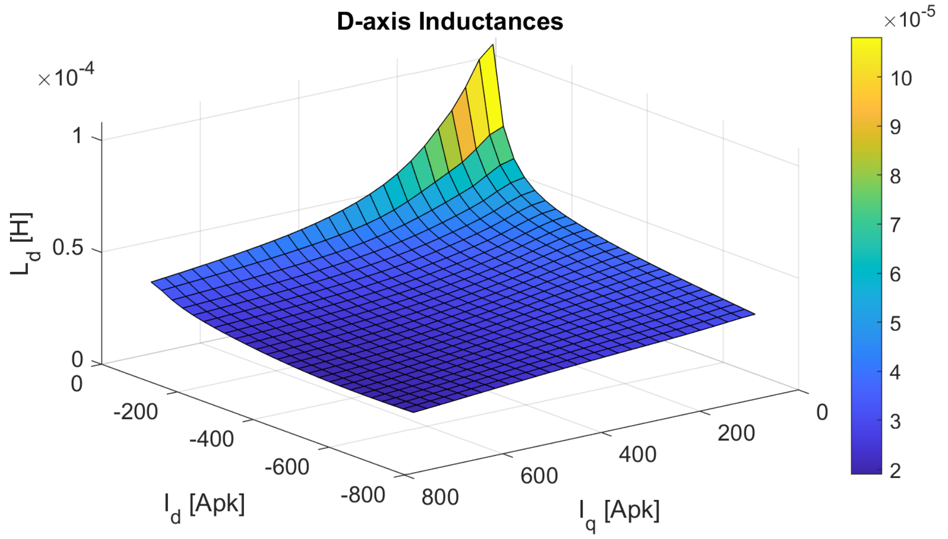

Figure 47: Inductance map of *d-axis* (L_d) obtained with the Standard Method.

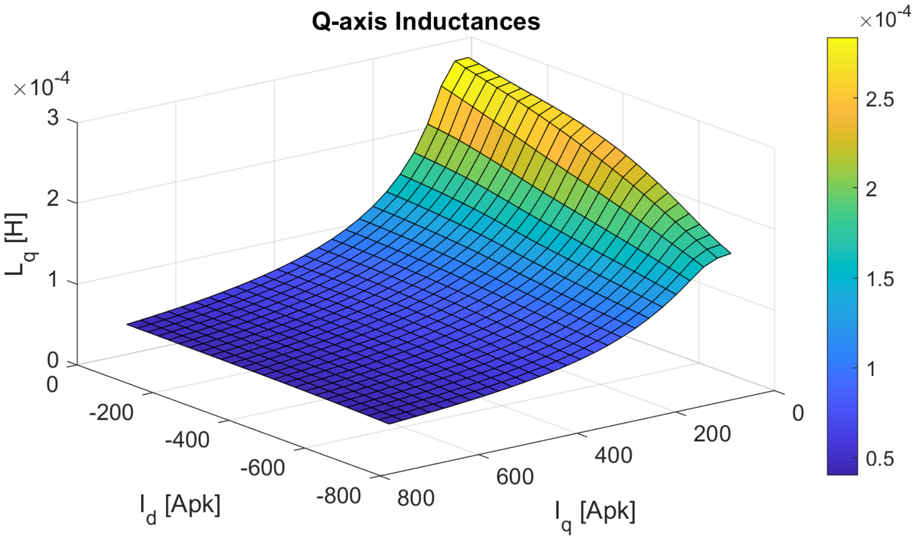

Figure 48: Inductance map of *q-axis* (L_q) obtained with the Standard Method.

3.3.2 Frozen Permeability Method

The Frozen Permeability method (FP) relies on two different sets of simulations. The first simulation is run in a specific operating point, generally rated operation, and the nonlinear magnetic model is obtained via 2-D FEA considering MMF contributions from armature currents and permanent-magnets. Then, the iron permeability is computed and stored for each mesh element by this nonlinear magnetic field analysis. Finally, permeability values are set for a second linear 2-D FEA simulation where permanent-magnets' MMF is set to zero.

Thanks to FP the stator inductances are evaluated with the actual working point of the ferromagnetic material. Hence, the estimation of inductances is accurate even when the permanent-magnets' MMF is set to zero, since FP includes the effects of permanent-magnets in the working point of stator and rotor laminations on the $B-H$ curve. Further details on FP method can be retrieved in [67] and [68]. This method provides inductance values significantly different from the Standard Method.

Similarly to the Standard Method, the complete maps of L_d and L_q inductances are obtained by a set of simulations with different couples of $i_d - i_q$ currents. The maps of the magnetic model of reference machine are shown in Figure 49 and Figure 50.

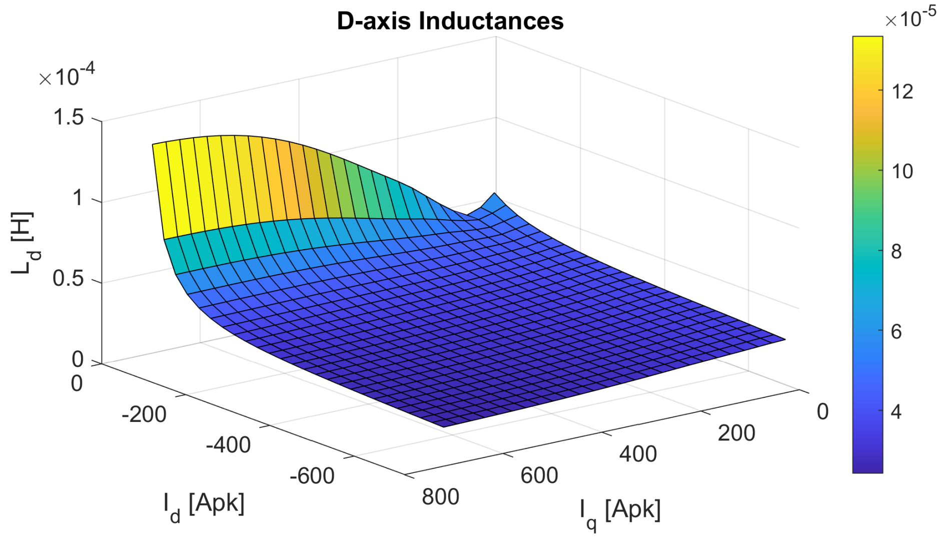

Figure 49: Inductance map of *d-axis* (L_d) obtained with the Frozen Permeability method.

3.4 Nonlinear *d-q* Model Computation

In the following, the algorithms developed for each control trajectory will be presented. The code is based on the L_d and L_q maps obtained from the nonlinear magnetic models computed by the two presented 2-D FEA methods. Before introducing control strategies algorithms, two control loops must be presented: iterative numeric process and stationary loop.

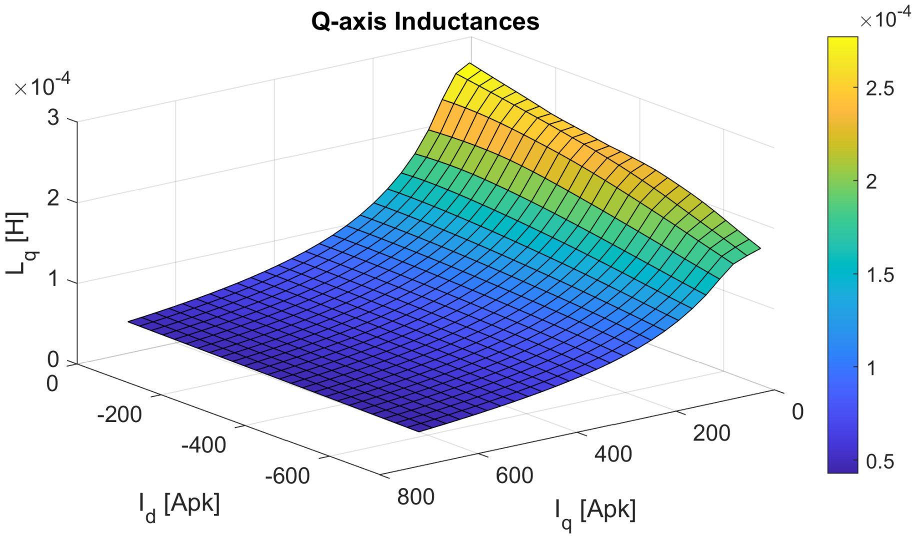

Figure 50: Inductance map of *q-axis* (L_q) obtained with the Frozen Permeability method.

The iterative numeric process is necessary to overcome an existing circular dependency: in order to compute the operating point $(I_d; I_q)$, the values of L_d and L_q must be known; however, these values are functions of the still unknown $(I_d; I_q)$ values. The iterative numeric process is adopted for all the curves and operates as follows:

- Define a starting value of L_d, L_q considering a known point belonging to the desired control curve;
- Compute I_d, I_q according to Eq. 3.11, Eq. 3.14 or Eq. 3.20 for MTPA, FW and MTPV respectively;
- Re-compute L_d, L_q with the current values of I_d, I_q and the inductances map;
- Use the new value of L_d, L_q computed in the previous bullet for the next iteration.

This iterative process can be further improved by a *stabilizing loop* that reiterates the previous procedure until the difference between the current value and the previous one is below a fixed threshold. As an example, this method was used for the estimation of the characteristic current I_{ch}, that has a circular dependency on L_d:

- I_{ch} is estimated with Eq. 3.8 using the mean value of L_d on the overall domain;
- L_d and L_q are computed in the point $(I_{ch}; 0)$ with the inductances map;
- I_{ch} is re-computed with Eq. 3.8;
- The difference ΔI_{ch} between the current I_{ch} value and the previous one is computed and

compared with a desired threshold.

This loop continues iterating until ΔI_{ch} decreases below the fixed threshold. In this way, undesired numerical oscillations are limited and L_d and L_q converge to the most precise values in the point of interest.

3.4.1 Maximum Torque Per Ampere (MTPA)

As shown in Section 3.2, MTPA curve cannot be expressed in a closed-form, when numerical maps of L_d and L_q are used. The numeric algorithm developed for MTPA iterates as follows:

- A space vector of current amplitude $[I]$ is defined ranging from 0 to current limit I_{lim} value;
- For each value of $[I]$, a vector of current phase $[\gamma]$ is defined ranging from 90° to 180°;
- Each couple of the matrix $[I;\gamma]$ identifies an operating point in the second quadrant of the *d*-*q* plane;
- For each couple, L_d and L_q are interpolated from inductances maps at disposal. Torque is computed by Eq. 3.4 and stored in a matrix;
- For each value of $[I]$, the maximum torque is computed comparing the matrix elements corresponding to each value of $[\gamma]$. Also the corresponding values of L_d, L_q, I_d and I_q are computed and stored.

In this way, the MTPA trajectory is identified and the base speed vector ω_{base} can be computed with Eq. 3.13 for each value of $[I]$. The ending element of ω_{base} vector will be used for the computation of FW trajectory.

3.4.2 Flux Weakening (FW)

While MTPA points are computed starting from a $[I;\gamma]$ matrix, FW and MTPV points are based on a speed vector. In fact, these last two strategies come into play for high speeds, and the maximum output torque is fixed by the speed. Hence, the procedure for FW computation is similar to the one for MTPA, but based on a speed vector. The FW algorithms works as follows:

- The last element of the base speed vector $[\omega_{base}]$ of MTPA is selected as the starting element for the FW speed ($\omega_{FW,start}$);

- The limit speed in FW ($\omega_{FW,end}$) is computed according to Eq. 3.15;
- The FW speed vector ranges from ω_{start} to ω_{lim};
- Starting values of L_d and L_q are computed in the end point of MTPA trajectory: $L_d = L_d(I_{d_{end,MTPA}}, I_{q_{end,MTPA}})$ and $L_q = L_q(I_{d_{end,MTPA}}, I_{q_{end,MTPA}})$;
- For each element of the speed vector, the following parameters are computed and stored:
  - I_d by Eq. 3.14;
  - I_q by the Current Limit Circle of Eq. 3.5;
  - Torque by Eq. 3.4;
  - The new values of L_d and L_q to be used for the next speed value are interpolated from the map with the current I_d and I_q values.

A graphical representation of the procedure is depicted in Figure 51.

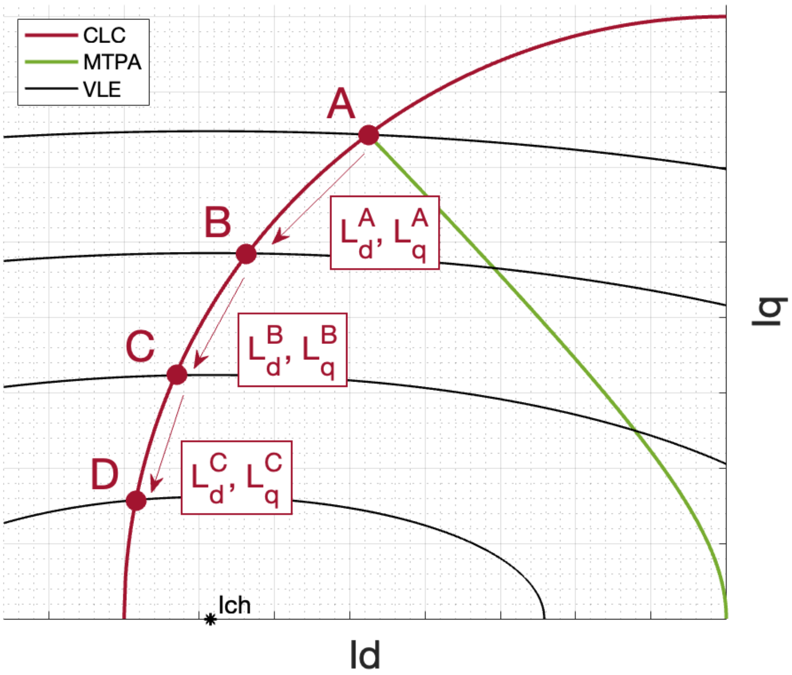

Figure 51: Procedure of the FW algorithm on the d-q reference plane .

3.4.3 Maximum Torque Per Volt (MTPV)

The algorithm for MTPV starts from a speed vector, considering $I_q = 0$ and then iterating for the overall range of γ. This procedure is more complex than the previous ones: in MTPA the computation was based on a $[I; \gamma]$ matrix and in FW a starting point was available, being the ending point of MTPA. Here, the starting values of L_d, L_q and γ are required at the beginning of each iteration. Hence, the point $(I_{ch}; 0)$ is chosen as the starting point for the trajectory computation, that corresponds to the infinite velocity point. In order to practically define a speed vector, the infinite velocity has been approximated with a very high velocity. Thus, the starting point of MTPV is located at $\gamma = 180°$ and an high speed value. Specifically, the algorithm for MTPV is based on the following loop:

- Starting values of L_d and L_q are computed in the starting point $(I_{ch}; 0)$ with the stabilizing loop described in Section 3.4;
- For each element of the speed vector with $\gamma' = 180$ř, the L_d and L_q values computed at the previous iteration are taken as starting values and the stabilizing loop is performed. After their values are fixed with high accuracy, the following parameters are computed:
  - I' and the I_D are computed by Eq. 3.18 where $I_Q = 0$;
  - I_d and I_q are computed by Eq. 3.16;
  - Torque is computed by Eq. 3.4 and stored in a matrix;
  - The new values of L_d and L_q to be used for the next speed value are interpolated from the map with the current I_d and I_q values.

So doing, the inductances and the torque on the d-axis have been fixed. Starting from these values, it is possible to iterate the procedure on the overall range of γ'. For each speed value:

- I' is computed by Eq. 3.18;
- I_D and I_Q are computed from I' and γ' by Eq. 3.18;
- I_d and I_q are computed by Eq. 3.16;
- Torque is computed by Eq. 3.4 and stored in a matrix;
- The new values of L_d and L_q to be used for the next γ' value are interpolated from the map with the current I_d and I_q values.

Once the complete torque matrix is computed for each operating point of $[\omega_{MTVP}, \gamma]$ the maximum torque is computed comparing the matrix elements corresponding to each value of $[\gamma]$. Also the corresponding values of L_d, L_q, I_d and I_q are computed and stored. In this way, the operating points of MTPV trajectory are obtained.

A graphical representation of the procedure is depicted in Figure 52.

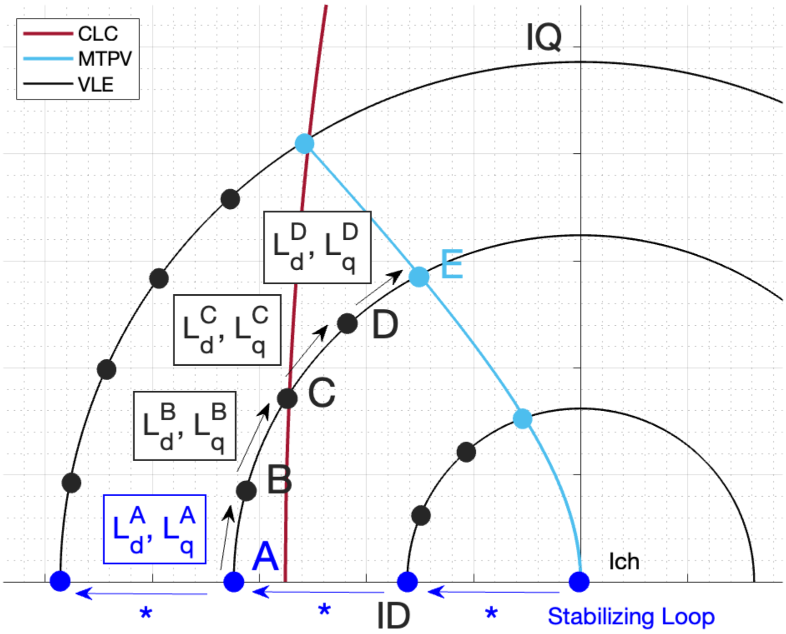

Figure 52: Procedure of MTPV algorithm on the new *D*-*Q* reference plane.

3.4.4 Voltage Limit Ellipses

As for the previous curves, also for the Voltage Limit Ellipses, the initial values for L_d and L_q must be set. For each ellipse, an initial point was chosen on the MTPA trajectory, computed in the previous subsection. Then, the points of the ellipse were computed iterating for lower I_d values (moving to the left) and higher I_d values (moving to the right) - i.e. d-axis current is negative. Hence, the ellipse is divided in a left and right side with respect to the MTPA curve. In the following only the algorithm approach for left part of VLE is described.

A set of values $[I_q]$ for which the corresponding ellipses will be evaluated is defined and for each element of this vector, then the following steps are carried out:

- The corresponding I_d on the MTPA trajectory is identified;
- The starting values of L_d and L_q are interpolated from the inductance map;
- The corresponding speed value is computed by Eq.3.7;
- A vector ranging from the identified I_d to the current limit $-I_{lim}$ is defined. For each value of this vector:
  - I_q is evaluated with the L_d and L_q of the previous step by Eq. 3.7;
  - The new L_d and L_q with the current values of I_d and I_q are interpolated from the

maps for the next iteration.

As an example, if the ending point of MTPA is used for the computation, the voltage limit ellipse corresponding to the rated speed will be obtained. The code for the right part of the ellipse is similar to the left part one, but the vector of I_d values ranges up to I_{lim} instead of $-I_{lim}$.

3.4.5 Constant Torque Hyperbolas

The Constant Torque Hyperbolas are computed with the same method of the Voltage Limit Ellipses and, in the following, only the code of left part is described. A set of values $[I_q]$ for which the corresponding hyperbole will be evaluated is defined and for each element of this vector, the following steps are carried out:

- The corresponding I_d on the MTPA trajectory is identified;
- The starting values of L_d and L_q are interpolated from the inductance map;
- The corresponding torque value is computed by Eq.3.4;
- A vector ranging from the identified I_d to the current limit $-I_{lim}$ is defined. For each value of this vector:
  - I_q is evaluated with the L_d and L_q of the previous step by Eq. 3.4;
  - The new L_d and L_q with the current values of I_d and I_q are interpolated from the map for the next iteration.

3.5 Results and Comparisons

3.5.1 Generated Control Trajectories

The control trajectories on the *d*-*q* plane were computed with both Standard Method and FP. The results are reported in Figure 54 and Figure 55 along with the curves obtained with the conventional linear magnetic model (Figure 53) in order to provide a clear comparison about their performance.

In the pictures, MTPA curves are drawn both in rated current case (solid line) and in overcurrent case (dashed line). MTPA trajectory is remarkably different with the three methods, especially at high currents (dashed line). In fact due to high saturation, inductances computed with FP differ significantly from the ones computed with the Standard and the linear method.

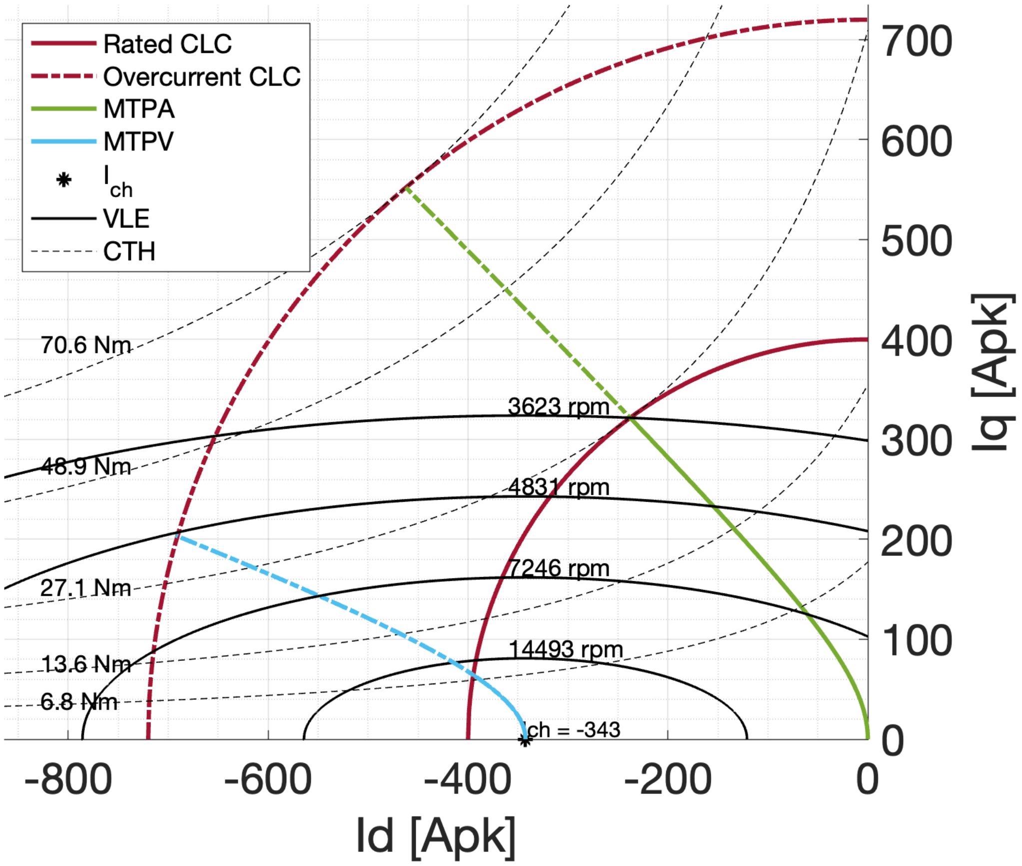

Figure 53: Control trajectories on the d-q plane computed with the conventional linear model.

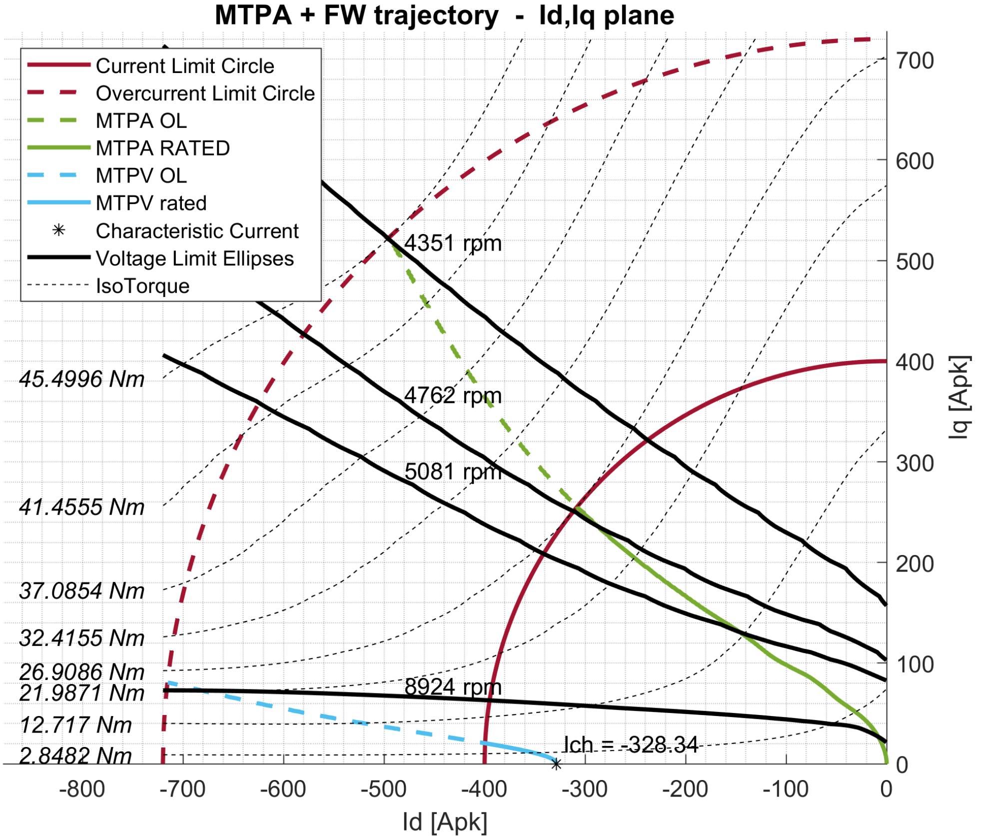

Figure 54: Control trajectories on the d-q plane computed with Standard Method.

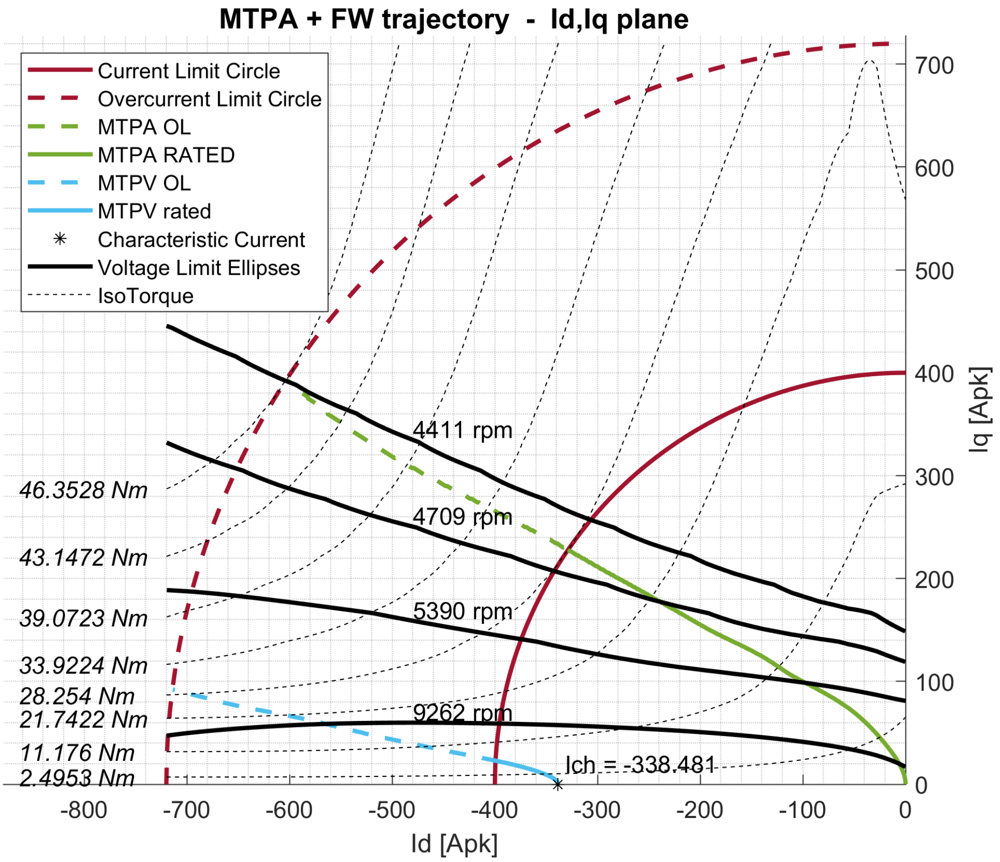

Figure 55: Control trajectories on the d-q plane computed with FP.

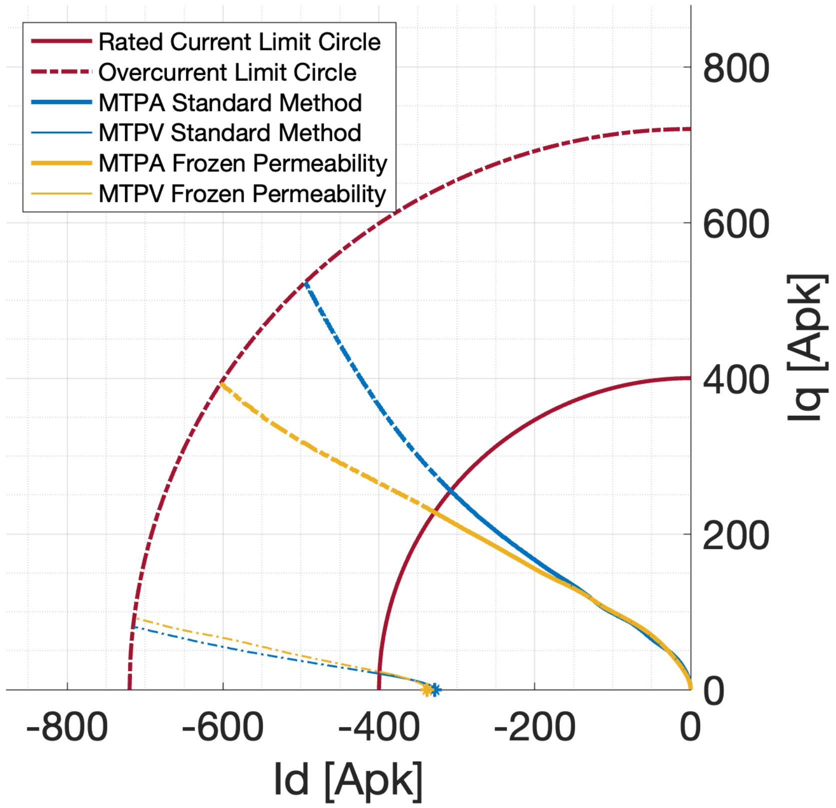

Figure 56: Comparison of MTPA and MTPV curves, obtained with Standard Method (blue) and FP (yellow).

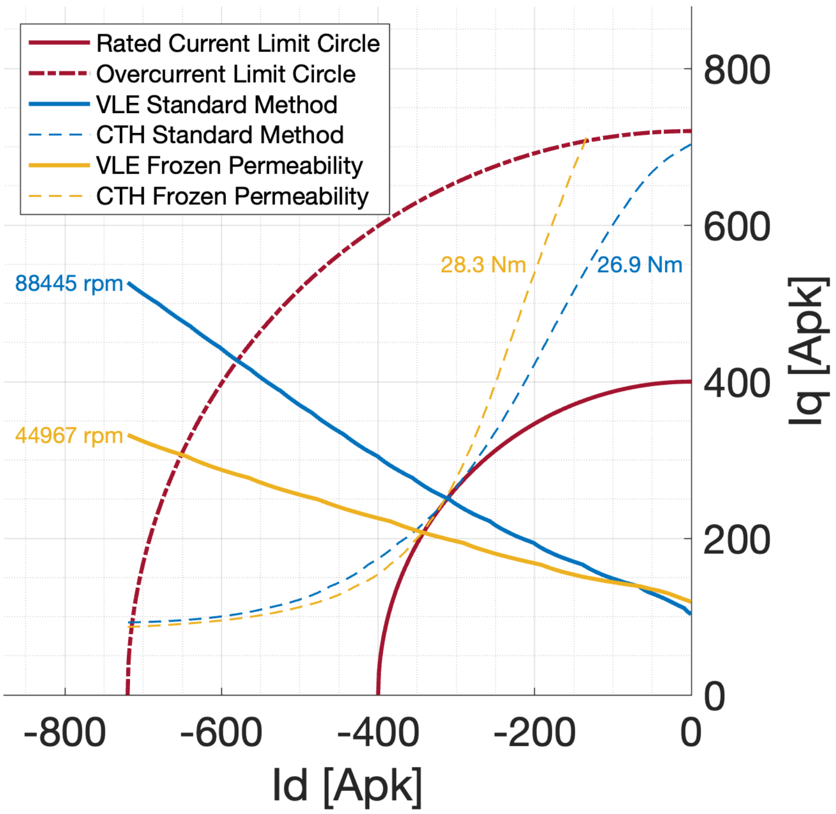

Figure 57: Comparison of Voltage Limit Ellipse (at base speed) and Constant Torque Hyperbola (at rated torque), obtained with Standard Method (blue) and FP (yellow).

The Voltage Limit Ellipses (black solid lines) are very different from the ideal ellipses of the conventional linear model (where the L_d and L_q are assumed to be constant). Specifically, on the left side of the d-q plane the ellipses moves away from the d-axis. Similarly to the case of MTPA, the linear model is less accurate when the amplitude of the current vector increases. These phenomena cause differences in the MTPA base speed and FW limit speed. On the other hand, the characteristic current point $[I_{ch}; 0]$ is similar for both the approaches, falling inside the rated current limit circle.

MTPA and MTPV curves are reported in the same figure for FP and Standard Method (Figure 56): MTPA trajectory computed with FP is more tilted towards the negative d-axis, underlining a better capability of such method to detect the correct behaviour of the machine when saturation starts to be non-negligible.

Fig. 57 highlights the differences between the two methods for the Voltage Limit Ellipse (computed at base speed) and the Constant Torque Hyperbola (computed at rated torque).

3.5.2 Comparison of the Two Different Nonlinear Methods

The comparison is further enhanced with a reference curve, based on trajectories computed with a 2-D FEA. Specifically, MTPA is computed by 2-D FEA *FEMM* with the following procedure:

- A range of current density $[J]$ is defined;
- A range of current phase angle $[\gamma]$ is defined;
- For each couple of $[J;\gamma]$ matrix, five different rotor positions are defined (6 mechanical degrees apart one from the other in order to cover 360 electrical degrees);
- The solution of the magnetic model is found for all the different rotor positions and torque is evaluated by the Maxwell's stress tensor;
- The mean value of the torque on all position is computed;

This process is repeated for each element $(J;\gamma)$. Then, MTPA trajectory is obtained computing the maximum torque value on all the values of γ.

Figure 58 shows a comparison between the MTPA curve obtained with: i) the conventional linear model (green line); ii) the nonlinear model based on standard magnetostatic simulations (blue line); iii) the nonlinear model based on FP simulations (yellow line); iv) the reference trajectory computed via 2-D FEA (purple line).

Results show that the MTPA trajectory is remarkably different for two nonlinear methods, especially at high currents (dashed lines). As shown, the reference 2-D FEA MTPA trajectory is much better matched with the MTPA obtained with FP method rather than with the one obtained with the Standard Method. The error for the linear model curve and for the Standard Method curve is significant especially outside the rated CLC, where the saturation effects are higher.

Regarding the output torque vs. speed characteristic, the comparison between linear model, standard nonlinear method and nonlinear FP is reported in Figure 59; in the constant torque region the three methods lead to a significant differences in the torque value, while in the constant power region the frozen permeability and the standard nonlinear methods lead to similar results. This is due to the effect of de-saturation linked with flux weakening.

In conclusion, FP method proves to be more accurate in the mapping and modeling of IPM synchronous machines.

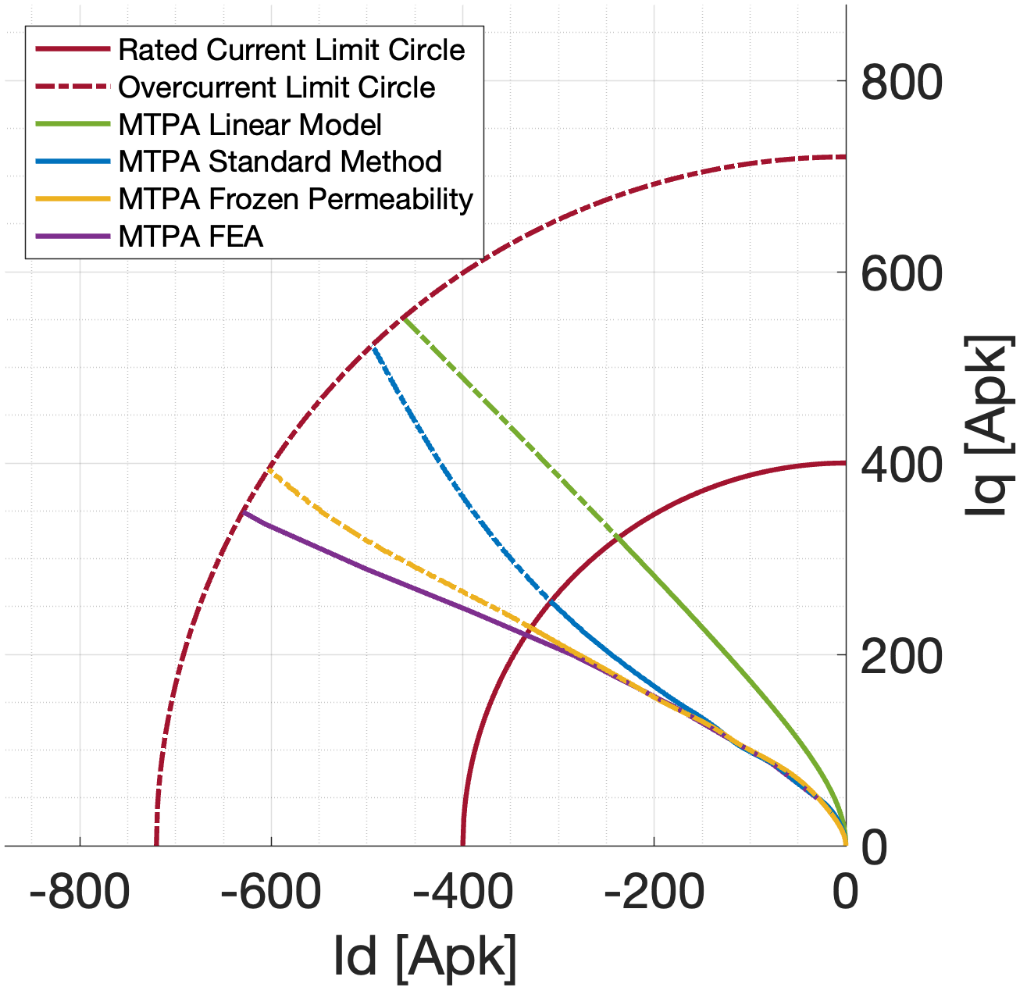

Figure 58: Comparison of MTPA curve obtained by the conventional linear model, nonlinear model based on Standard Method, nonlinear model based on FP and direct computation via 2D FEA.

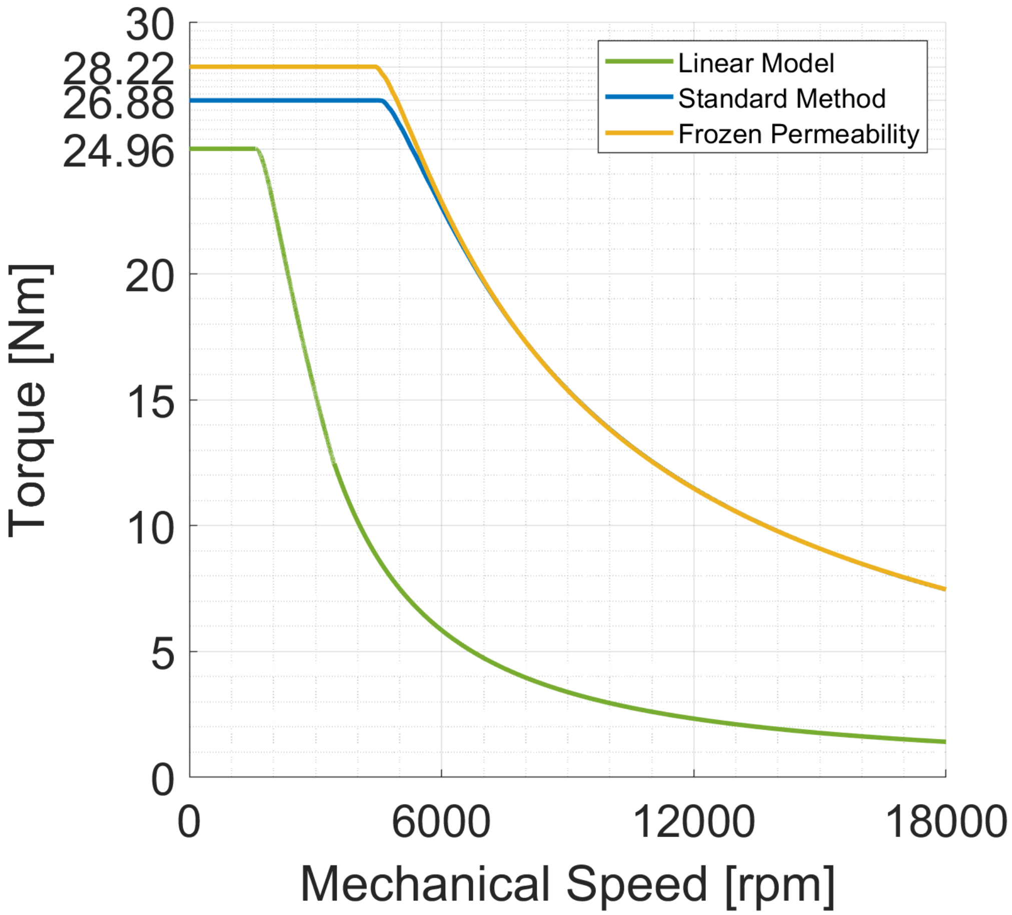

Figure 59: Comparison of Torque-Speed curves obtained by the conventional linear model, nonlinear model based on Standard Method and nonlinear model based on FP.

3.6 Conclusions and future developments

A new algorithmic approach to compute the machine performance in MTPA, FW and MTPV for IPM synchronous machines is presented. The proposed approach is applied to compute the current components in the $i_d - i_q$ reference frame for the MTPA, FW and MTPV, evaluating also the voltage limit ellipses, isotorque curves, and torque vs. speed characteristic. Moreover, the proposed algorithms are efficient and suited to a real-time implementation, being still quite reliable in case of magnetic saturation. More traditional methods are based on a linear model, that does not account for L_d and L_q variations with the working point of the machine. Hence, traditional method fails at high speed, and/or with magnetic saturation, on the other hand a direct analytical solutions would require the computation of partial derivatives of $L_d\,(I,\gamma)$ and $L_q\,(I,\gamma)$ with respect to the current phase angle, leading to complex and unfeasible real-time implementations. A method for MTPA, FW and MTPV is presented. This method is efficient and suited to a real-time implementation, being still quite reliable in case of magnetic saturation. The proposed method is based on the inductance maps of the machine obtained by 2-D Finite Element Analysis. Two different methods were adopted for the FEA simulations: a standard nonlinear magnetostatic method (Standard Method) and Frozen Permeability method (FP Method). The two solutions were assessed by a reference curve, obtained with a direct computation 2-D FEA via the Maxwell's stress tensor. MTPA curve obtained with the conventional linear model differs significantly from the reference curve, especially for high currents values. On the other hand, the trajectory obtained with the proposed algorithmic approaches more similar to the reference. In addition to that, a comparison of the accuracy of the Frozen Permeability method with respect to the Standard Method was made. Results prove the higher accuracy of the nonlinear model based on Frozen Permeability, especially in case of relevant currents and high saturation.

4. Enhanced Internal Permanent-Magnet Machines Flux Weakening Control Strategies for Traction Applications

Internal Permanent magnet machine is one of the most common typologies employed in the design of power train for electric transportation. It shows: high torque density, high efficiency (due to the absence the magnetizing current and rotor circuit) and high flux-weakening capability [69]. In power train application flux-weakening control strategy is a critical point because electrical machines operate in a wide speed range above the constant torque region. The fluxweakening definition is due to the fact that the stator magnetic field is used to weaken the permanent-magnet flux linked with the stator coil. This aim is achieved by increasing the negative d-axis current component until the characteristic current of the machine for an ideal infinite speed range when the characteristic current match the outer limit of the current circle. Many papers deal with the optimal magnetic flux quantity to obtain an optimal machine behavior, that can be substantially synthetized in a machine design that force the characteristic current on the edge of the current limit circle in the id-iq plane, thus avoiding MTPV region to obtain the maximum exploitation of the power train. For electric vehicle application this simple statement must fulfill different duty types with corresponding different current limits, therefore a trade-off has to be found. In this chapter the characteristic current is designed to be in the middle of two current limits corresponding to the continuous duty type (S1) and the short-time duty (S2). According to this design approach a large volume of rare earth permanent-magnets must be employed achieving high machine performance and efficiency, but also high permanent magnet linkage flux. With this design approach, during flux-weakening operation at high speed it is necessary to counteract the magnet Back-EMF with an appropriate d-axis magnetomotive force, in particular a high negative d-axis current has to be fed even if the torque set point is quite low or at least equal to zero. Different flux-weakening control strategies have been developed in the last years as shown in [70], [71], nevertheless even if this control strategies are strongly proven in motor operation, few studies and examples of what happen during fast transitions of the torque set point and the external load at high speed have been deeply investigated. The control strategy for an electrical vehicle is usually based only on a torque control loop and the driver adjusts the vehicle speed acting on the throttle (torque control). During brake or other fast torque transitions, the torque set point could be moved from its maximum value to zero and, if the motor is in the flux-weakening region, the motor should move its working point either in generating region or in a zero-torque condition. During the transition of torque set point, the current angle error due to iron losses changes its sign [72] making difficult to manage the energy-flow transition from the motor to the battery to avoid battery unsafe operation or overcharge. Moreover, the vehicle behavior could be heavily affected by the braking torque generated by the motor, especially for motorcycles also a short time braking torque could cause drive injures.

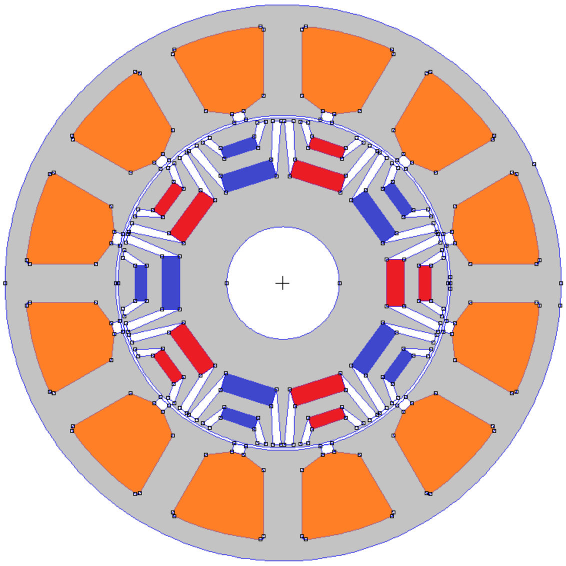

Figure 60: Geometry of an IPM motor.

The author of [73] proposes a flux-weakening control algorithm based on the increase of the id current error, once the voltage limit is reached. This id error is used to decrease the vq axis voltage set point. The control scheme is substantially a modification of the classical feed-forward vector control method. This solution allows a smooth transition from MTPA to flux-weakening control strategies and a fast response. In addition, this method does not strongly rely on the motor parameter and LUT of the magnetic model. Other control approaches [74] implement the fluxweakening strategy employing the outer voltage loop to generate an appropriate id current to keep the voltage vector within the range limits imposed by the Voltage DC BUS. The control scheme is aimed to the voltage maximum exploitation, also in this case no specific strategy is deeply investigated to manage the fast torque transition. In paper [75], an enhanced control strategy for high speed permanent-magnet synchronous machines is proposed for electric vehicle application. This control strategy operates from low up to high speeds region employing the same approach of the outer voltage loop adding some additional block with also the MTPV equations. Even in this case fast torque transition issue is not pointed out and no tests on a real vehicle are presented. Other similar control strategies are presented in [76],[77],[78].

4.1 PM vector control equations

According to d-q rotor reference frame, where the d-axis corresponds to the North permanent-magnet (PM) magnetic axis, the steady-state voltage equations of permanent-magnet synchronous motor PMSM are expressed as follows:

$$\begin{cases} v_d = R_s i_d - \omega_e L_q i_q \\ v_q = R_s i_q + \omega_e \Lambda_{PM} + \omega_e L_d i_d \end{cases} \tag{4.1}$$

where i_d, i_q, v_d, v_q are d- and q-axis components of stator currents and motor terminal voltages, Λ_{PM} is the PM flux, R_s is the stator resistance, L_d and L_q are d- and q-axis selfinductances. If the motor has no saliency the selfinductances are equals.

The terms $-\omega_e L_q i_q$ and $+\omega_e L_d i_d$ are the motional terms which couples d-q axis components. These two contributions could be compensated in the control strategy in order to have two independent axes. The torque equation of PM motor is expressed in Eq. 4.2:

$$T = \frac{3}{2} p \left[\Lambda_{PM} i_q + \left(L_q - L_d \right) i_d i_q \right] \tag{4.2}$$

where p is the pole pair number.

Fig. 61 shows the machine operating regions: the region I is the constant torque and the region II is the constant power one. Inside the region I the operating limits are imposed by current circle limit, see Eq. 4.3, while the limit of region II is given by both voltage and current limit circle. The voltage limit circle in the i_d-i_q plane becomes an ellipse, see Eq. 4.4 and Eq. 4.5

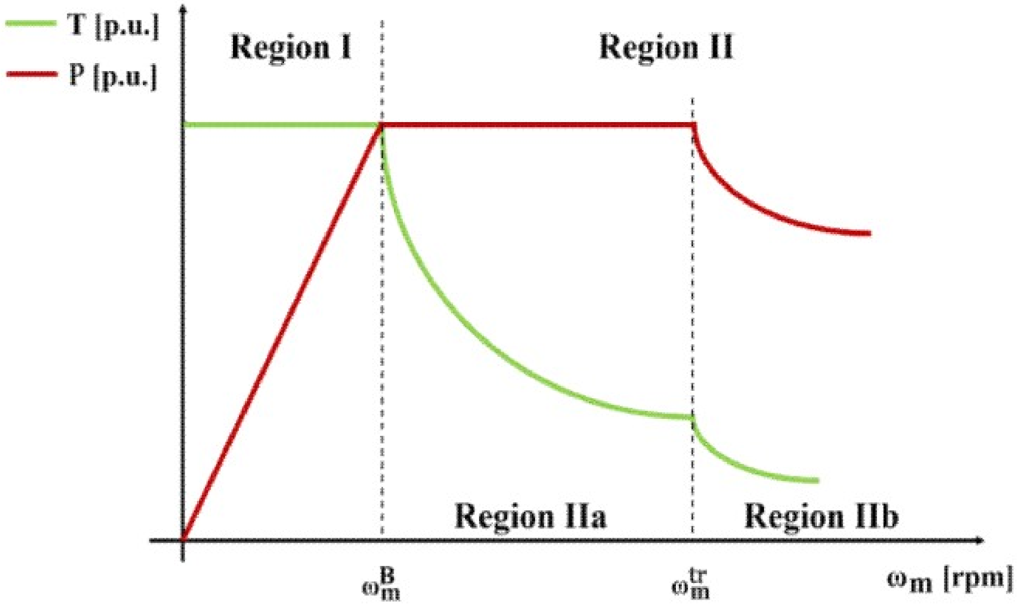

Figure 61: Electrical machine operating regions.

where ω_m is rotor mechanical speed.

$$i_d^2 + i_q^2 <= i_{Lim}^2 \tag{4.3}$$

$$v_d^2 + v_q^2 <= v_{Lim}^2 \tag{4.4}$$

$$L_d^2 \left(i_{Lim} + \frac{\Lambda_{PM}}{L_d} \right)^2 + L_q^2 i_q^2 <= \left(\frac{v_{Lim}}{p\omega_m} \right) \tag{4.5}$$

Current and voltage limits depend on the inverter kVA rating and the battery voltage state. For a given machine, the voltage limit depends on machine mechanical speed, in particular the ellipse axes shrink as the mechanical speed increases. The center of the voltage ellipse is expressed as follows:

$$i_{ch} = -\frac{\Lambda_{PM}}{L_d} \tag{4.6}$$

The aim of the motor control is to set the machine electrical inputs to obtain a certain torque at a given mechanical speed enhancing power train performance. In so doing an optimized control strategy has to be adopted. The control strategy of region I is so called MTPA, which objective is to maximize the torque to current ratio (that corresponds to the minimization of the Joule losses). The region II could be divided in two sub-region IIa and IIb, if the voltage ellipse center i_{ch} falls inside the current limit. In the sub-region IIa the motor is controlled according to flux weakening (FW) strategy, while in the region IIb the MTPV strategy has to be adopted to maximize the torque to voltage ratio.

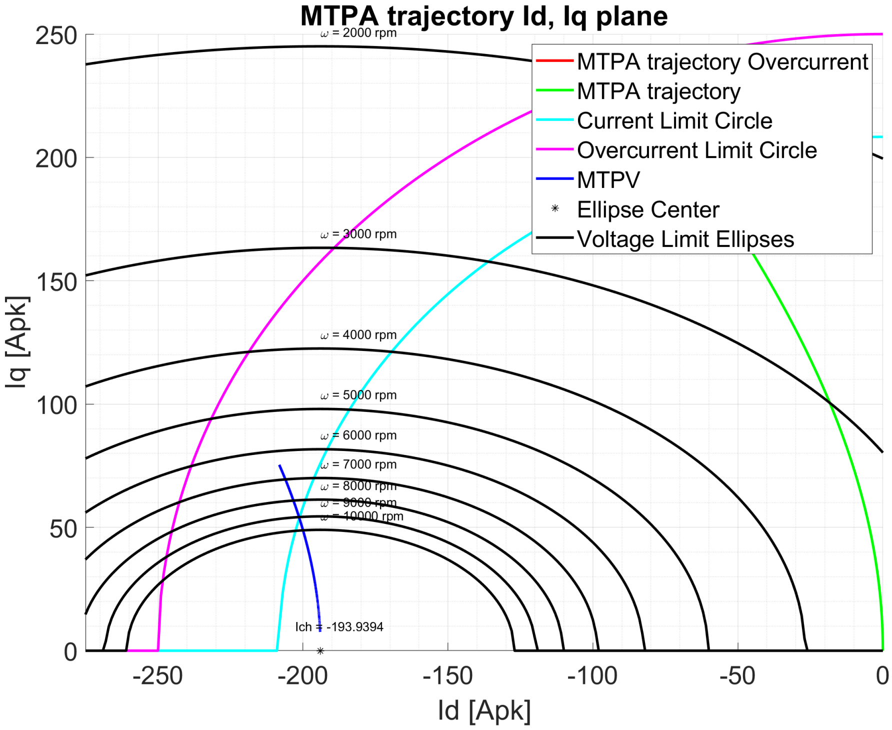

Figure 62: Theoretical i_d-i_q plane control strategies.

4.2 Flux weakening behaviour in traction application

During the vehicle operating conditions, the driver controls the torque reference by means of the throttle. Thus, during acceleration, the ideal behaviour depends linearly to the torque set point. This correlation is fundamentally true in MTPA region, while in FW the torque decreases as the speed increases with a constant current vector amplitude. Therefore, a robust control strategy should approximate this behaviour and guarantee a full exploitation of the FW region. Flux Weakening, in traction applications, permits to achieve an extended constant power range eliminating the need for mechanical gear ratio and avoiding the volt-ampere oversizing of the power converter. To implement Field Weakening of IPM motor it is necessary to generate a suitable negative i_d setpoint. As a matter of fact, a negative id current will produce a flux along the *d*-axis opposing the rated flux generated by Permanent Magnets. The strategy adopted to determine the i_d setpoint affects the motor performance and it must be designed taking into account on one side the torque generation and on the other the voltage and current limitations. As is well known a Field Weakening strategy can reduce the generated torque deteriorating acceleration performance if a too strong action is made. On the contrary a late start or a weak action may result in undesired torque drop according to the current regulator saturation. Since the current set point and the level of Flux Weakening depend on load, motor parameters and battery state of charge the generation of the ideal weakening trajectory and, in turn, of the relative id setpoint it's a complicated task. From a theoretical point of view the i_d and i_q setpoints could be computed starting from the torque command and the desired flux magnitude. With this approach, known as feedforward technique, it's almost impossible to obtain the maximum possible torque vs speed due to parameters change during motor operation. Voltage battery variation, magnetic saturation, resistive voltage drop can affect the final result. In [76] an effective feed-forward flux-weakening control algorithm, based on motor equations, is proposed. Assuming I_s the maximum inverter current and V_{BUS} the measured BUS voltage, from equations 4.3 and 4.5 it is possible to obtain currents command $i_{d_{safe}}$, $i_{q_{max}}$ in function of motor parameters, electrical speed $\omega_e = p\omega_m$ and BUS voltage:

$$\begin{cases} i_{d_{safe}} = \dfrac{-\Lambda_{PM}L_d+\sqrt{\Lambda_{PM}^2 L_d^2-\left(L_d^2-L_q^2\right)\left(L_q^2 I_{max}^2+\Lambda_{PM}^2-\frac{V_{BUS}^2}{\omega_e^2}\right)}}{\left(L_d^2-L_q^2\right)} \\ i_{q_{max}} = \sqrt{I_s^2 - i_d^2} \end{cases} \tag{4.7}$$

Fig. 63 reports the results obtained by Feed Forward technique generation of i_d command. The first set (red solid lines) is obtained using rated motor parameter and the actual Battery

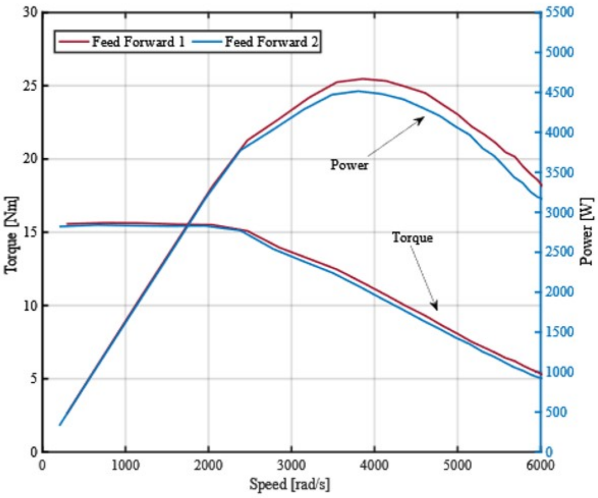

Figure 63: Drive performance with Feed Forward strategy with two different battery charge levels. Red line with the correct battery voltage and blue line with underestimated BUS voltage of 5%.

voltage. The second one (blue solid lines) refers to a situation in which the BUS voltage is underestimated of about 5%. As it is clearly visible in the latter case the torque and, then, the power obtained in Flux Weakening conditions are lower than previous one. It could be helpful to recall that in both cases the results are away from those you will get in an ideal situation being the mechanical power far from constant in Flux Weakening region. In summary some closed-loop correction is necessary to fully exploit the power limit of IPM motors.

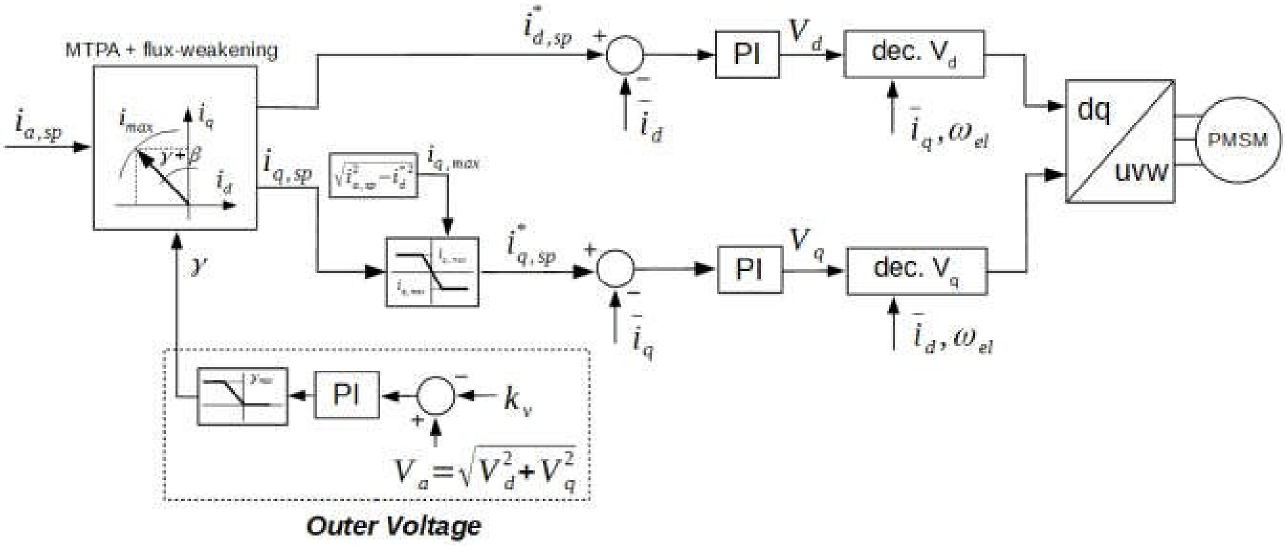

Figure 64: Outer Voltage Scheme proposed in [74].

In literature methods based on saturation of current regulators detection or on voltage satu-

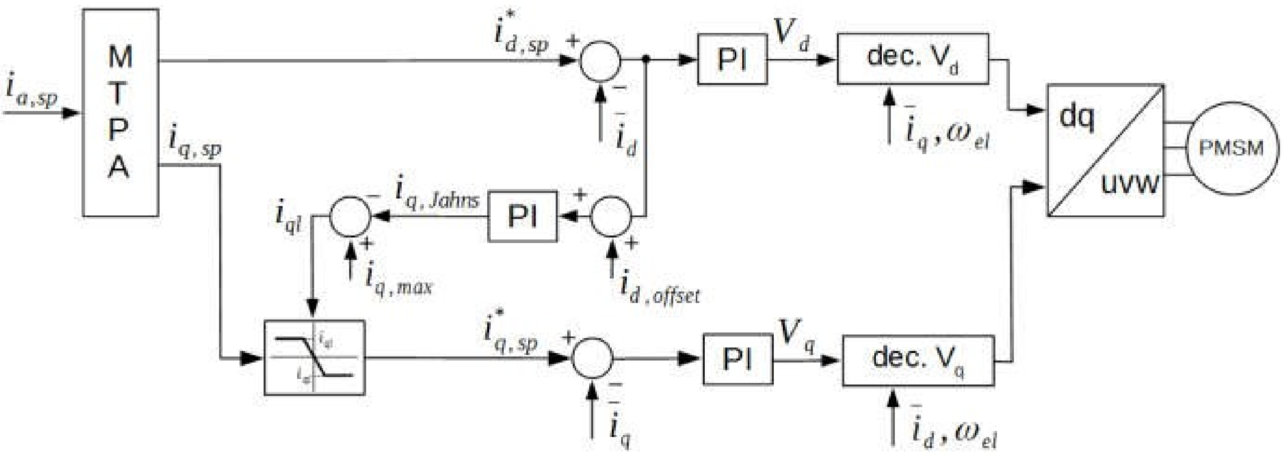

Figure 65: Control scheme proposed by “Jahns” in [73].

ration detection have been proposed by researchers. Among them we investigated the scheme proposed in [74] [72] and in [73] because of their simplicity and effectiveness.

Fig. 64 reports the scheme proposed in [74]. In the MTPA operations the torque command is converted into the corresponding values of d-q axis current commands $i_{a_{sp}}$ by function blocks f1 and f2 and then the polar to rectangular conversion block ($i_{d_{sp}}$ and $i_{q_{sp}}$).

The flux-weakening control module executes the current angle reduction by a PI regulator which input is the voltage saturation error obtained by comparing the requested voltage with the available battery voltage that depends on the state of charge.

Fig. 65 reports the scheme proposed in [73]. In this solution MTPA operation is very similar, the flux-weakening control is realized using the i_d error (Δi_d) between the d-axis current command $i_{d_{sp}}$ and the resultant value $\bar{i}_d$ which provides valuable detection feedback. In presence of a growing d-axis current error Δi_d, the q-axis current command $i_{q_{sp}}$ will be decreased. By so doing the command current vector is forced back down inside the ellipse instead of lying outside the voltage limit ellipse at a given speed. Both methods look good to exploit the potential of the IPM electrical machine in flux-weakening, almost in acceleration. Since under both schemes rely on an integral action that drives the limits of the currents command, some issues could arise in deceleration depending on the integral dynamic.

With the aim to test their performance in acceleration and in deceleration as well, a suitable test bed was implemented (see Section 4.4).

Fig. 66a and 66b show the performance in acceleration and deceleration of the flux-wakening strategy of both outer voltage method and Jahns method during experimental tests. As previ-

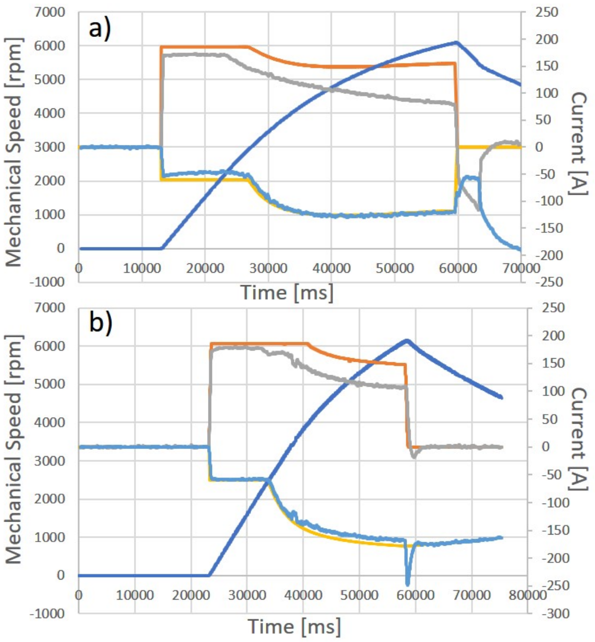

Figure 66: Speed profile (blue solid line) and d-q currents signals: i_d set point (yellow solid line), motor i_d((light blue solid line), i_q set point (orange solid line) and motor i_q (grey solid line). 7a) Outer voltage control and 7b) Jahns control.

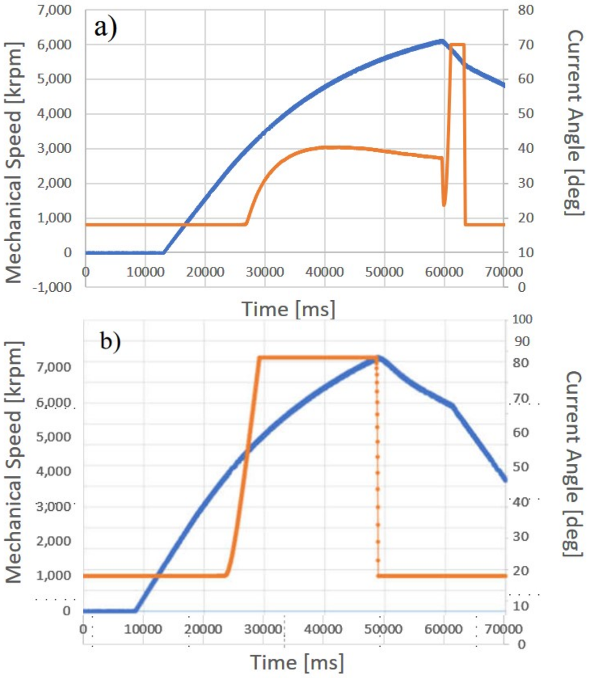

Figure 67: a) Outer voltage current angle (orange solid line) and b) Jahns current angle (orange solid line).

ously discussed, the flux-weakening angle or d-q current components are computed relying on an integrator. As it can be expected, they perform quite good in acceleration, but present a big issue when the torque command goes abruptly to zero at high speed due a external mechanical braking action.

In Fig. 67a and 67b it can be appreciated that the angle computed by the integrator (orange solid line) when torque command goes to zero, approaches the value computed for the MTPA region. This is due to the fact that in breaking condition the voltage error in the outer loop method changes sign and the integral value reduces it to its minimum angle value (about 18 deg). Something similar happens in Jahns method as well.

Obviously since i_d setpoint should depend on speed and voltage only, the sudden change of the outer voltage error generates a wrong $i^*_{d_{sp}}$ command, i.e. the $i^*_{d_{sp}}$ command suitable for MTPA region. This in turn generates an error in current control giving rise to voltage error or i_d error again. Moreover, it produces an uncontrolled active breaking torque and an uncontrolled generation, with consequent uncontrolled current flow in battery pack. Eventually also the breaking feeling perceived by the driver will be uncomfortable being the initial braking phase uncontrolled and, in condition of wet road, it can be harmful. In Fig. 66a the different slope of the speed profile during braking phase in case of outer voltage method can be appreciate. Jahns method (Fig. 66b) results are quite similar.

4.3 Optimized control strategy for flux weakening operation

To improve the performance of both methods, a feed-forward action based on the current command of formula 4.7 was introduced to overcome the issue related to the current angle computation. In so doing a good estimation of the d-axis current can be computed and adopted by the control strategy during breaking in flux-weakening region.

During breaking phase in flux-weakening region, if the $i_{d_{sp}}$ command computed using the integral approach is lower than the $i_{d_{safe}}$ command resulting from 4.7 the latter will be taken as $i^*_{d_{sp}}$ current setpoint. Thus, the motor performance is preserved during breaking phase at high speed. This is the reason why we named this contribution “id-safe”.

Fig. 68 reports the experimental result of the Outer Voltage method improved by the “id-safe” strategy, while Fig. 69 shows the corresponding results during acceleration/deceleration from

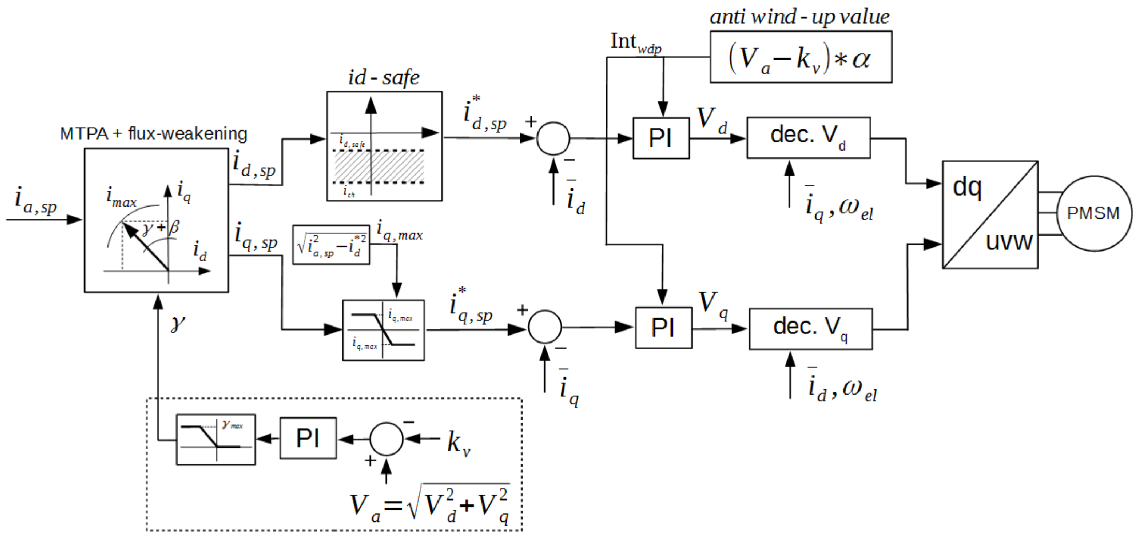

Figure 68: Outer Voltage method improved by the Id-safe strategy.

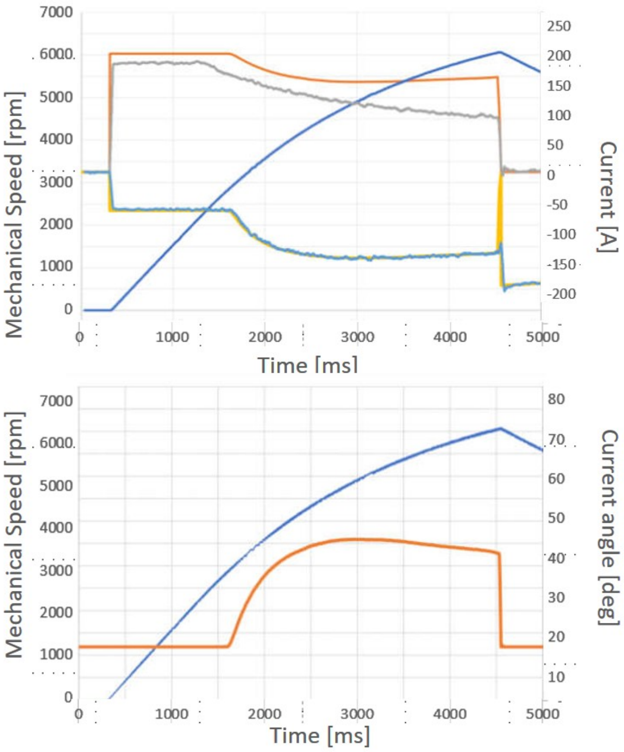

Figure 69: Improved Outer Voltage method results; a) speed profile and i_d and i_q currents signals and b) current phase angle (orage solid line).

zero up to 6000 rpm and back. During the braking phase the current angle is by-passed by the “id-safe” values, as it can be seen the annoying effect on speed at the early braking stage is properly compensated and the performance repetitiveness was guaranteed.

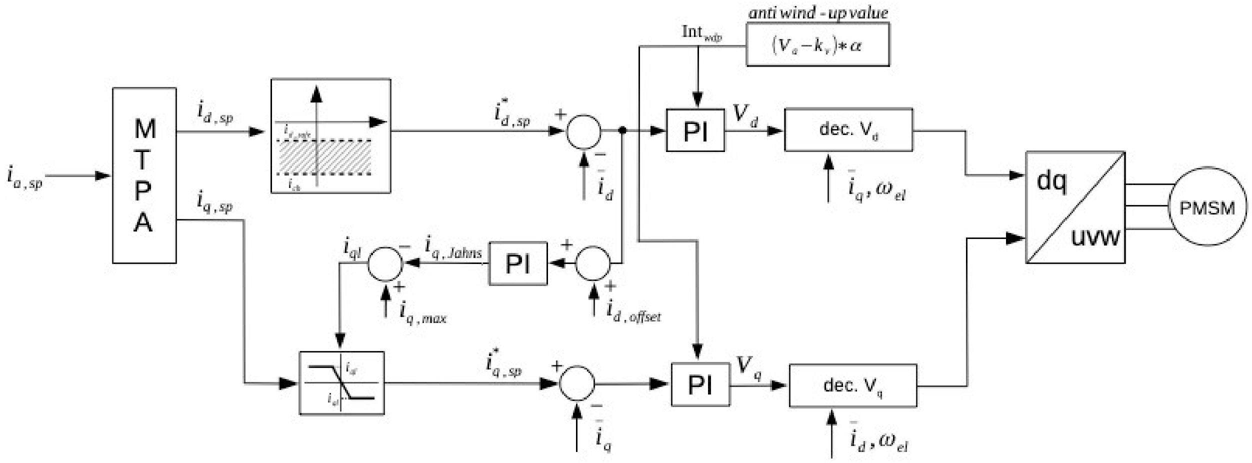

Figure 70: Improved Jahns control scheme.

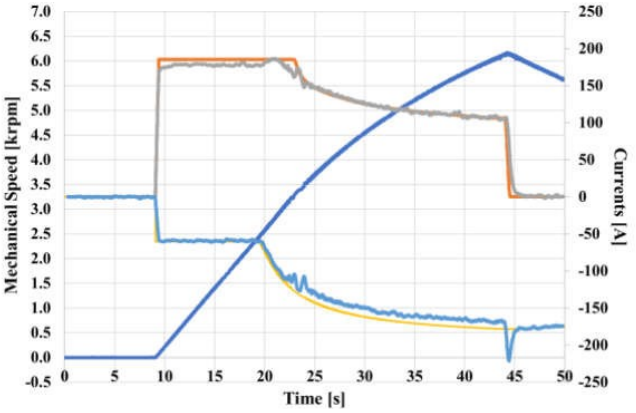

Figure 71: Improved Jahns control scheme results; speed profile and i_d-i_q currents signals.

The same feed-forward action was introduced in Jahns control scheme. Fig. 70 shows the resulting control scheme while Fig. 71 reports the behaviour during acceleration /deceleration from zero up to 6000 rpm and back. The current angle profile is similar to that shown in Fig. 67. Also, in this case the breaking action performs good showing controllability and repetitiveness. A particular anti-wind up approach has been introduced with the aim to increase further the performance in flux-weakening region, while keeping the voltage request on the edge of the saturation. In particular the error between the requested voltage and the voltage at disposal is multiplied by a suitable gain F and then it is summed to the integral action of both d-q axis current PI regulators. In so doing, no deep saturation of current PI regulators can arise due to the lack of voltage. The dynamic performance of the system increases, since current PI regulators are forced to ask, more or less, what the system can realize in term of voltage. This solution must be applied with great care in case of outer voltage, since this method relies on voltage saturation for current angle computation.

4.4 Experimental results

The proposed control strategies have been validated on an active test bench. The rig is composed as follows:

- 12 slots 10 poles IPM Motor under test;
- Three-phase high current drive;
- Power analyzer;
- Torque meter;
- 48 V lead battery pack;
- Active brake 45 kW, 500 Nm.

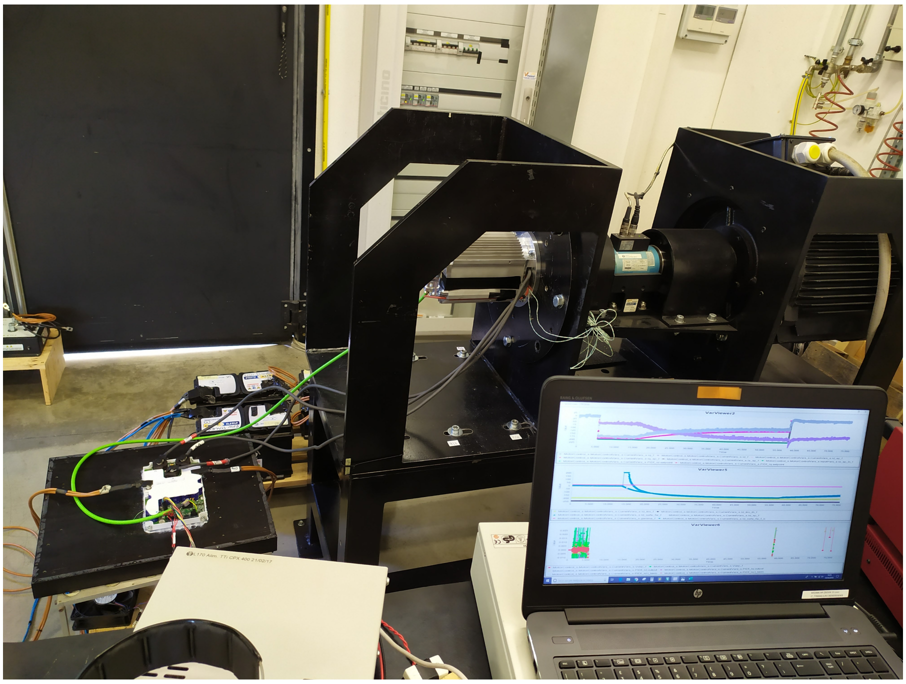

Figure 72: Test bench set up.

The test bench is shown in Fig. 72, while TABLE I reports IPM motor characteristics used to show experimental results shown in Sections 4.2 and 4.3. The control algorithms have been implemented on an ARM architecture floating-point DSP STM32F407VET6, using LEM HC5F800-s as current transducer, based on hall effect principle. The run-time control data, such as set points and measured currents on d-q axis, are logged by STM-Studio software. The active brake has been controlled by a speed loop control, while the motor under test has been controlled with a torque reference employing the proposed control loop and strategies. The IPM motor has a nominal continuous torque of 8.5 Nm @ 4500 rpm. The lamination external diameter is equal to 120 mm, while the stack length is equal to 120 mm. The motor is cooled by natural convection and radiation air cooling frame with fins. The rotor position sensor is an absolute digital magnetic encoder.

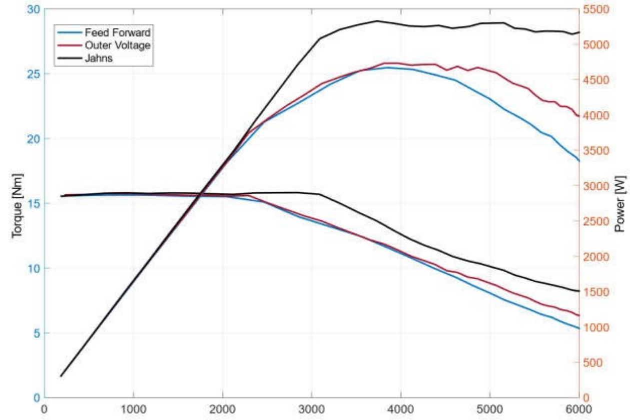

Figure 73: Results comparison between feed forward method and the improved proposed methods. Feed forward strategy (red solid line), improved outer voltage (light blue solid line) and improved Jahns method (black solid line).

Fig. 73 show the result of the comparison between feed forward approach, optimized outer loop and optimized Jahns in terms of torque and power generation versus speed. It is clearly visible that Jahns outperforms both feed-forward method and outer loop method.

4.5 Conclusions

Different IPM motor control strategies for light traction pure electric vehicles were analyzed. Two methods proposed in literature based on saturation of current regulators detection or on voltage saturation detection have been adopted. Their performance exploits good the potential of the IPM electrical machine in Flux Weakening during acceleration, but since they rely on an integral action some issues could arise in deceleration depending on the integral dynamic as observed during experimental tests. According to this, to overcome this issue two additional control strategies to optimize their performance during deceleration were introduced. The pro-

Table 7: IPM Drive Motor Characteristics.

Name	**Description**	**Value**	**Unit of Measurement**
I_n	Nominal current	68.5	A_{rms}
T_n	Nominal load torque	8.5	Nm
ω_m	Nominal mechanical speed	4500	rpm
Q	Number of slots	12	-
p	Pole pairs	5	-
V_n	Nominal supply voltage	48	V_{rms}
Λ_{PM}	Permanent magnet flux	13.2	mWb
I_{ov}	Overload current	335	A_{rms}
T_{ov}	Overload torque	34.5	Nm
k_t	Torque constant	0.13	V_{rms}/A_{rms}
L_{stk}	lamination stack length	120	mm
n_c	Number of slot conductors	10	-
S_w	Copper wire section	7.6	mm^2
L_w	Wire length	5.9	m
R_{ph-ph}	Phase-to-Phase resistance	3.3	$m\Omega$
L_{ph-ph}	Phase-to-Phase indutance	0.22	mH
$S2$	Short duty time	30	min

posed control actions are “id-safe” and anti-wind up approach. The “id-safe” is a feed forward value which corrects the id current command according to motor speed and BUS voltage. The anti-wind up avoids the deep saturation of d-q current PI regulators allowing to fully exploit the available BUS voltage. The optimized methods have been validated by experimental tests with an IPM motor for light electric vehicle. Both methods have improved the motor performance, during transition from flux-weakening strategy to MTPA due to deceleration. The anti-wind up must be applied with great care in case of outer voltage control strategy.

5. Extended MTPA-FW Control Technique for PM Electrical Machines with CSI

5.1 Motor Parameters and Reference Trajectories

The machine taken into account in this chapter is an interior permanent magnet (IPM) syncronous machine. IPM machines are widely used in this field since they allow to obtain high performance by combining the different torque source of synchronous reluctance machines and traditional permanent magnets machines. In Table 9 the main parameters of the motor considered for the simulations are reported and Fig. 74 shows the geometry of the motor considered.

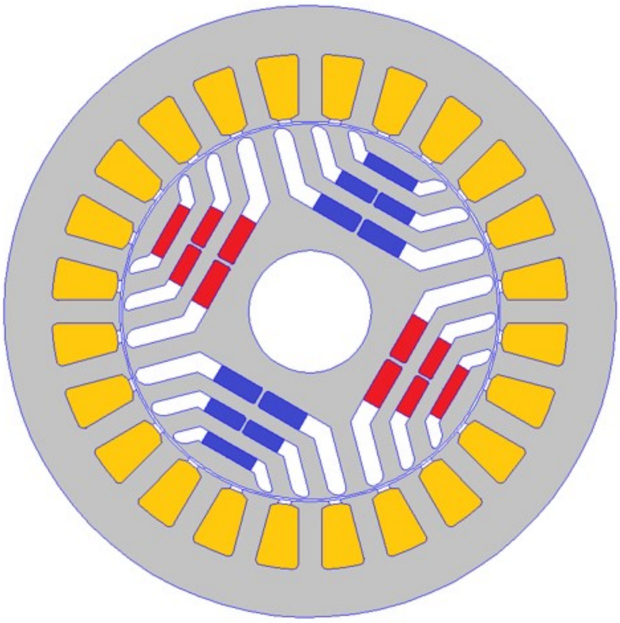

Figure 74: Reference motor considered for the application.

The overall performance of the motor are given by the interaction of the motor, the drive, and the power source, therefore the torque-speed characteristic is determined only when all the system parameter are defined and a control strategy is chosen.

To obtain an extended speed range a proper control strategy must be implemented to reduce the main machine flux, usually an external control loop is added to the vector control to move toward the negative id axis the current vector when the required voltage exceed the voltage limit. When the characteristic current is inside the current limit circle an additional control loop must added to reduce the current vector amplitude in order to move from the FW control strategy to MTPV control strategy.

In the following the motor model is simplified and the inductance values on d and q axis are considered constant (as reported in Table 9) for a simpler comparison between VSI and CSI performance, a more detailed approach considering variable inductances can be found in [79].

The electric power train model was created in PLECS, where all the simulations were made.

Neglecting magnetic saturation of the machine, the optimal control trajectories obtained are shown in Fig. 75. As expexcted MTPA, FW and MTPV are needed to reach the maximum speed value desired, so the control implementation can become quite complicated with a traditional VSI as the maximum speed value is limited by the DC BUS Voltage.

Another important advantage of the CSI topology is that it allows to control directly the current given as an input to the stator of the motor. Thanks to this, their shape is almost a pure sinusoidal waveform with almost null ripple, leading to a minimization of the traditional PWM losses in magnets and iron that are normally generated from VSI current ripple.

5.2 VSI Model

A traditional VSI architecture was chosen, with 6 switches With a DC BUS as input ideal voltage source, see Fig. 76. The voltage source inverter was employed to drive the electric

Table 8: Motor Data

Motor Parameter	**Symbol**	**Value**	**Unit**
Slot number	Q	24	-
Pole pairs number	p	2	-
Nominal current	I	425	A_{rms}
Nominal torque	T	44	Nm
Mechanical power	P_{mec}	14	kW
Maximum speed	ω_{max}	23000	rpm
Stator phase resistance	R_s	3.2	$m\Omega$
Stator d-axis inductance	L_d	3.1	mH
Stator q-axis inductance	L_d	8	mH

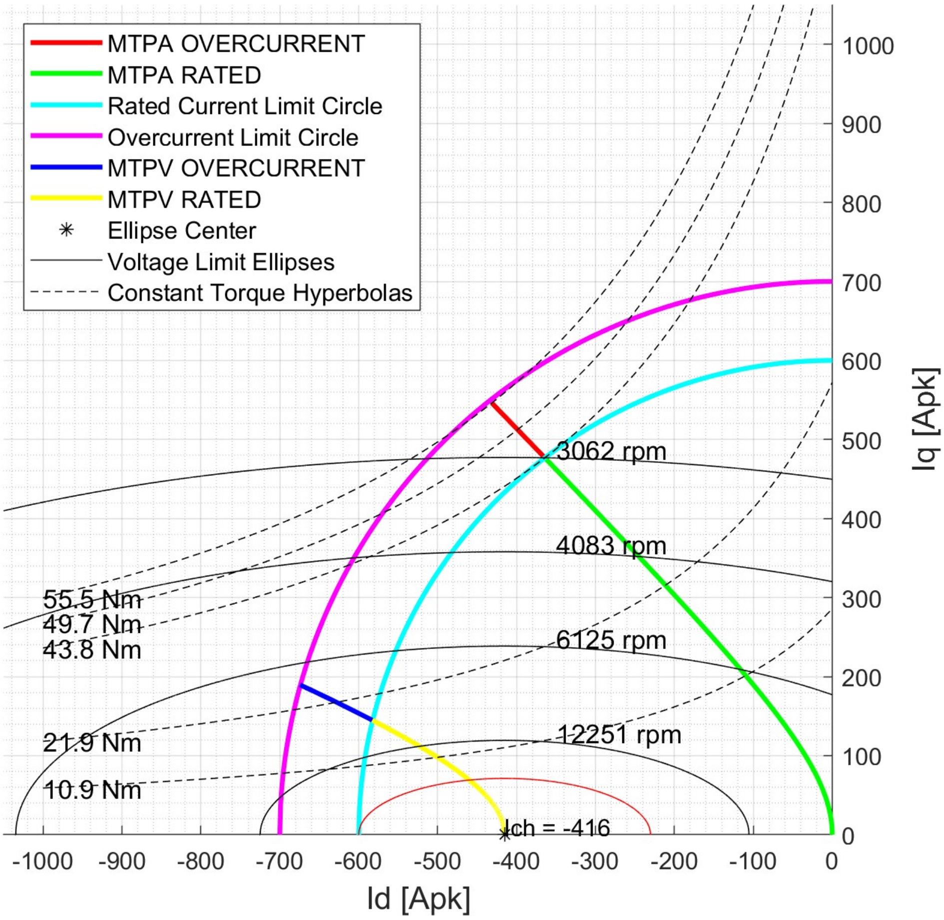

Figure 75: Optimal control trajectories.

motor, whose parameters are the one presented in Section 5.1, all the components and the control blocks were modelled in PLECS.

In Fig. 77 the block diagram of the control mode for the MTPA is reported. The current vector angle for MTPA is given as a function of the current amplitude.

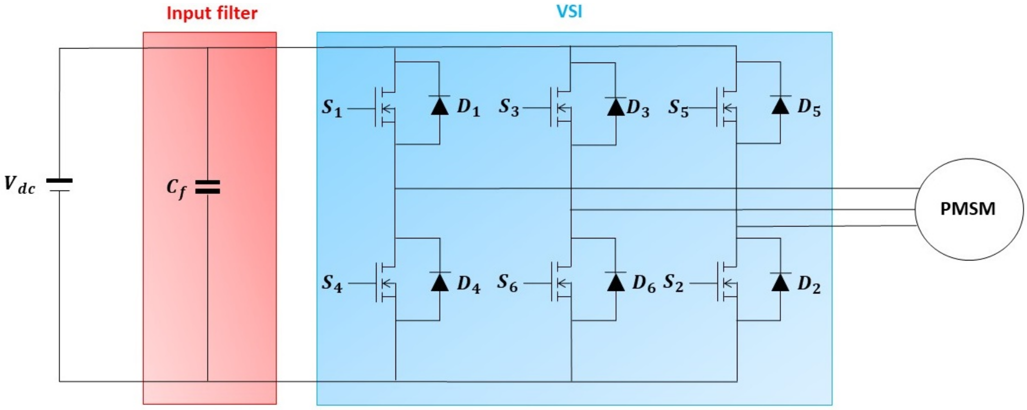

Figure 76: VSI schematic.

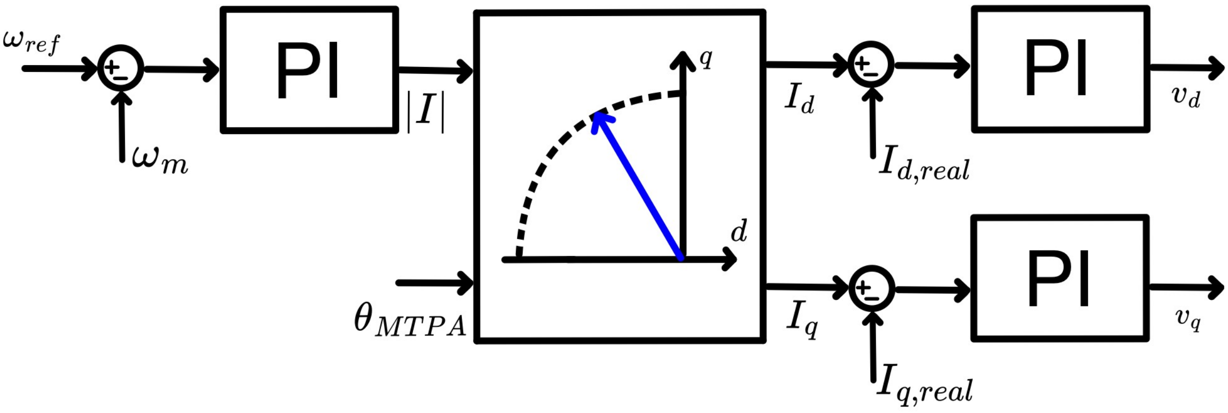

Figure 77: Block diagram of the VSI control mode in MTPA conditions.

With the purpose of reaching the desired speed of 23000 rpm, a flux weakening strategy must be implemented, in this case an outer voltage loop is employed to modify the current vector angle. The voltage required by the current loop is comparet to the DC BUS voltage, when the required phase voltage exceed the available DC BUS limit the flux weakening loop will add an additional angle to the current vector to increase the negative id current and decrease the iq current as shown in Fig. 78.

In this case, a MTPV control strategy must be implemented to reach the speed setpoint. Initially, the maximum speed reachable with FW is computed according to (5.1).

$$\omega_{FW,end} = \frac{V_{lim}}{p_p(L_d I_{lim} + \lambda_{pm})} \tag{5.1}$$

When the mechanical speed of the motor reaches $\omega_{FW_{end}}$, the MTPV control strategy starts to act; the saturation blocks which limits the current module obtained at the output of the speed loop and the d axis current obtained from the outer voltage loop. So the current amplitude is reduced dynamically, according to the desired MTPV trajectory found which maximize the motor performance.

When the current values on d and q axis are found, they must be converted into voltage values, needed to find the correct PWM modulation for the VSI. Several types of already known modulation exist: the one chosen was a Symmetrical Space Vector Modulation (Symmetrical SVM), since it allows chasing sinusoidal voltages with a peak value up to $\sqrt{3}/2 \cdot V_{dc}$.

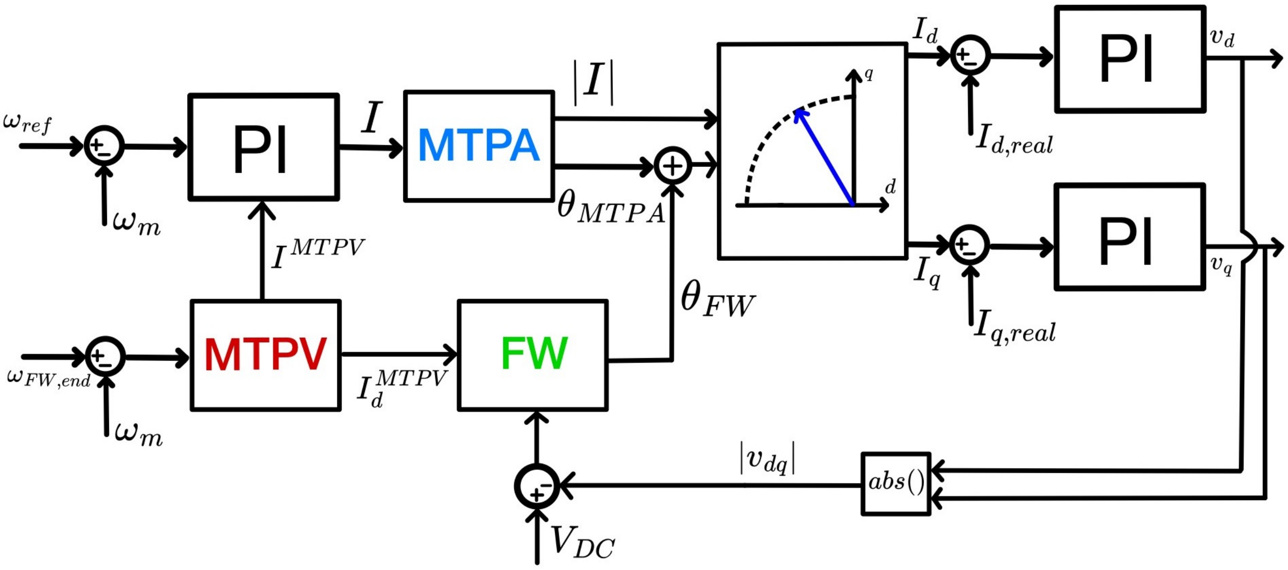

Figure 78: Block diagram of the VSI control mode in MTPA, FW and MTPV conditions.

In PLECS a constant set point of 23000 rpm was applied: in Fig. 79, the theoretical resulting torque is shown considering all of the three control strategies implemented. In order to get to the desired speed set point, MTPA, FW and MTPV must be used in the control loop. Differently from what it is shown in the following section it is not possible to delay the flux weakening for a VSI without increasing the input DC voltage.

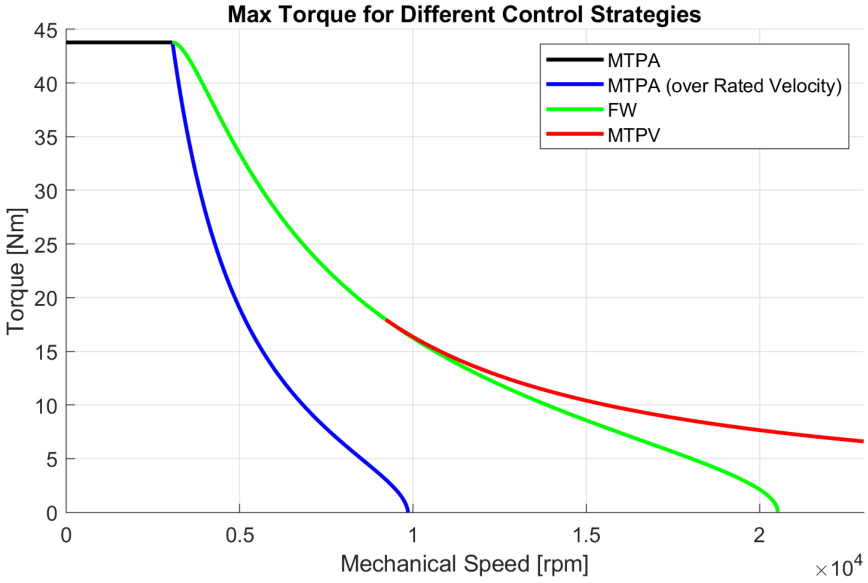

Figure 79: Motor electrical torque with VSI for different control strategies.

5.3 CSI Model

5.3.1 CSI Architecture

The traditional CSI architecture includes an half-bridge pre-stage to generate the input DC current and six switches, SiC MOSFETs in this case, Fig. 80.

The need of a pre-stage was already explained in the low-speed range, since the back-EMF peak values of the motor are lower than then the DC input voltage. Several efforts have been made in literature to eliminate the pre-stage: authors of [80] and [81] proposed its elimination in the high speed range and its maintenance in the low speed range. More recently, authors of [82] proposed to substitute the pre-stage with a coupled inductor and a diode. However, these works did not consider a FW strategy, which is necessary if the motor back EMFs cannot surpass the input DC voltage and the boost capability of the CSI can be exploited only for a limited speed range. That explains the need of a pre-stage in this work. Particularly a bidirectional boost was chosen since it allows to reduce the number of devices and switching losses for obvious reasons. Of course, the input inductance L_{DC} and the output filter C_f, should be designed. For the DC-link inductance a margin has been taken with respect to the formula in (5.2), well-known in literature, that defines the minimum value.

$$L_{DC} = \frac{\sqrt{3} T_{sw} V_m}{4 \Delta I_{DC,max}} \tag{5.2}$$

Where T_{sw} is the switching frequency period, chosen equal to $1/60kHz$, V_m is the peak value of the voltage awaited on the motor side and $\Delta I_{DC,max} = 5\% I_{DC}$. The resulting inductance $L_{DC} = 0.1\ mH$. About the output C_f filter instead, the problem of the LCL resonance was deeply studied in [83]. $C_f = 300\ \mu F$ was found to be a value that kept the electrical torque ripple moderate at low mechanical speeds, the switching frequency influences the filter design too. Torque "glitches" are reduced thanks to an alternate modulation too, see Subsection C.

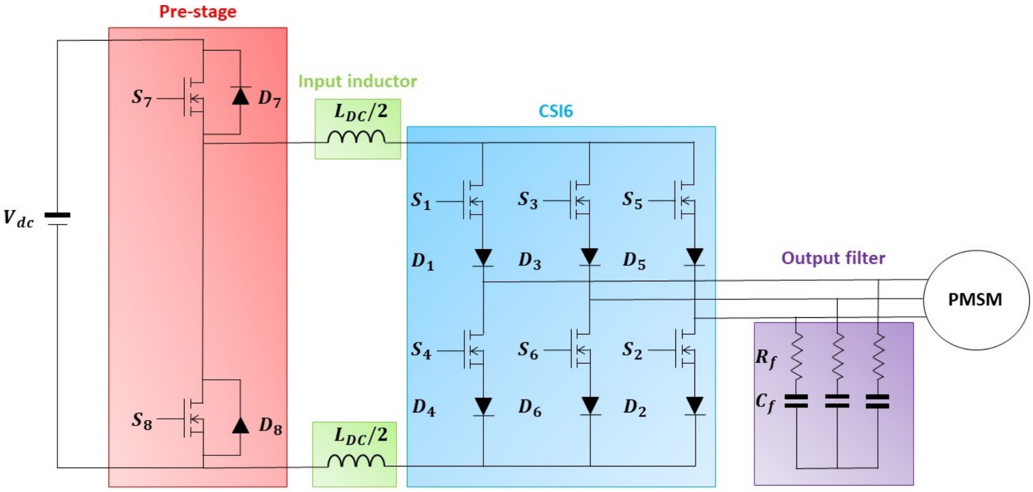

Figure 80: CSI schematic.

5.3.2 Proposed Control scheme and Flux-Weakening Technique

Similarly to the procedure followed for the control design of the VSI, the CSI control strategy was defined. In Fig. 81 the simple MTPA control strategy is reported. In this case, the current value obtained in output are called m_d and m_q, since they are directly used for the modulation strategy of the CSI, that, differently from VSI, is driven in current.

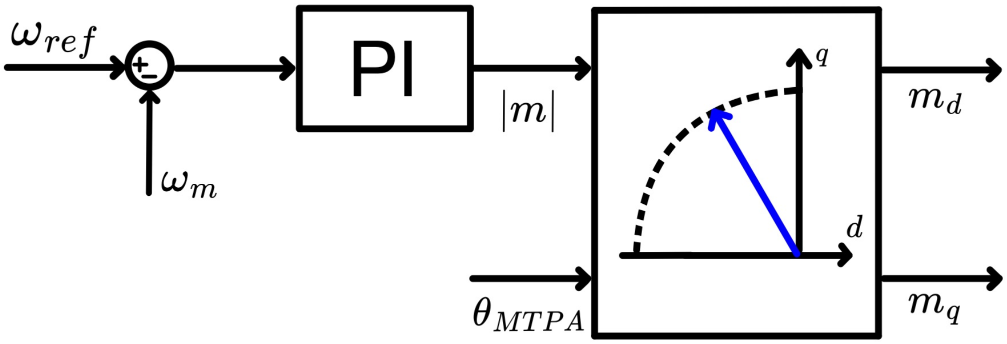

Figure 81: Block diagram of the CSI control mode in MTPA conditions.

In Fig. 82 the MTPA and FW more traditional control strategy is reported. This implementation for the CSI simplifies the total number of control loops since there is not the passage from d-q currents to d-q voltages, compared to a more traditional MTPA and FW control applied to a VSI. It should be stated that all the articles reported in the bibliography did not treat the FW problem for a CSI, however for very high speed range it becomes necessary. In [84], the authors explained different ways to delay the flux weakening and decided to implement the reduction of the modulation index, i.e. the ratio between the module of the reference current and the DC current. Decreasing the ratio, reduces the efficiency but allows reaching higher speeds without implementing a FW algorithm, because a higher current from the DC source and therefore the output voltages of the CSI increase: here another method is employed and the FW implementation proposed in this chapter and shown in Fig. 83 is quite different. In order to exploit the CSI boost capability, an additional control loop is added to modify the overlap time when the voltage limit is near. In this way the motor can receive more voltage and the base speed increase with respect to the VSI application. When the maximum overlap time is considered, the maximum voltage is reached and the flux weakening can begin, reaching higher torque at the maximum final speed.

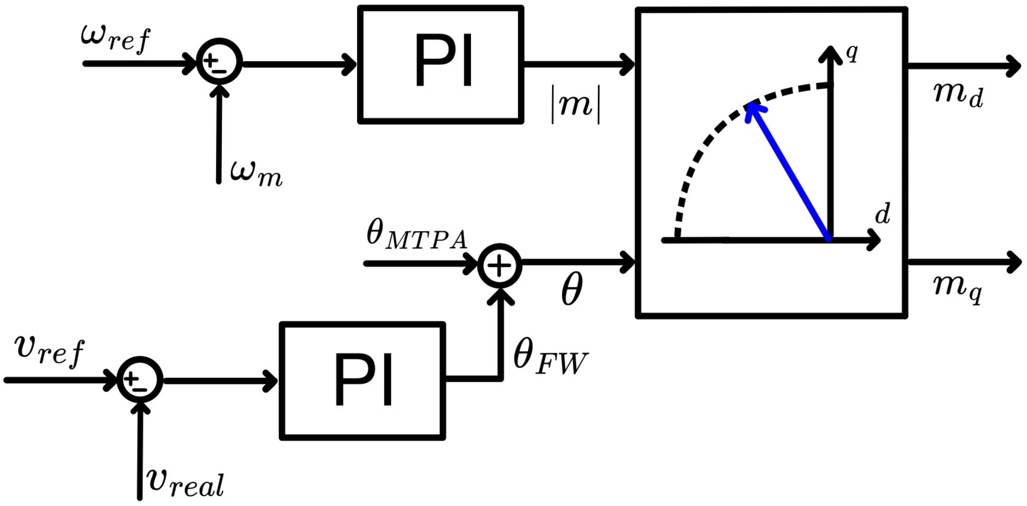

Figure 82: Block diagram of the CSI control mode in MTPA and FW conditions.

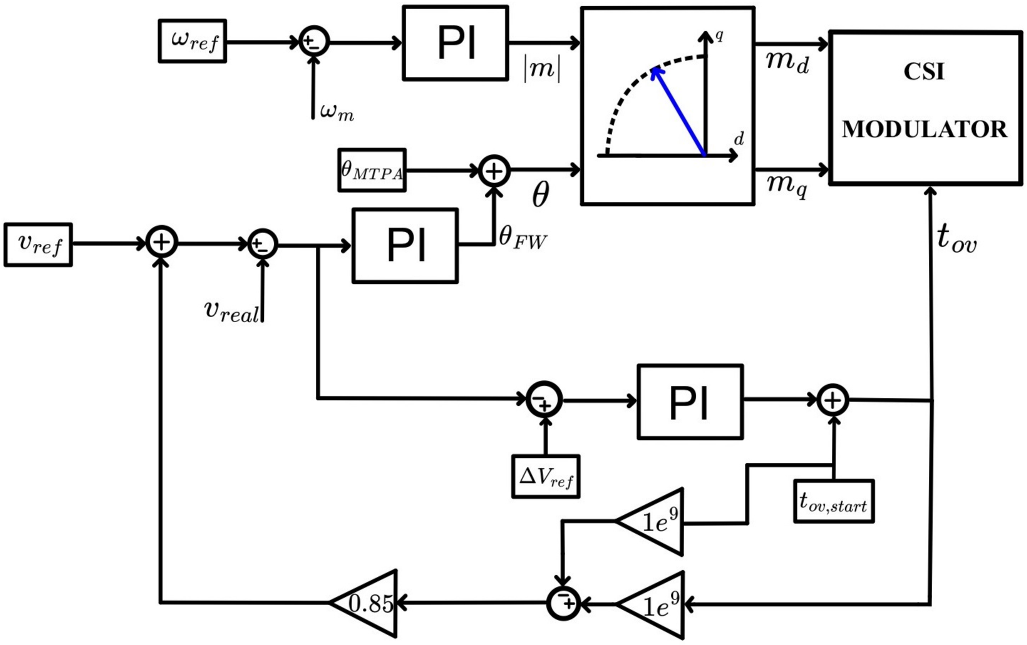

Figure 83: Block diagram of the CSI control mode in MTPA and FW conditions with voltage boost.

In Fig. 84, the advantage of employing an overlap time variation is clear: the blue curve was obtained keeping the overlap constant at 10 ns, instead the yellow one was obtained, varying it from 10 ns to 100 ns. As well as for the VSI, simulations were carried out at $f_{sw,CSI} = 60\ kHz$ and $f_{sw,pre} = 60\ kHz$. Efficiency results are reported and compared with the VSI in Section 5.4.

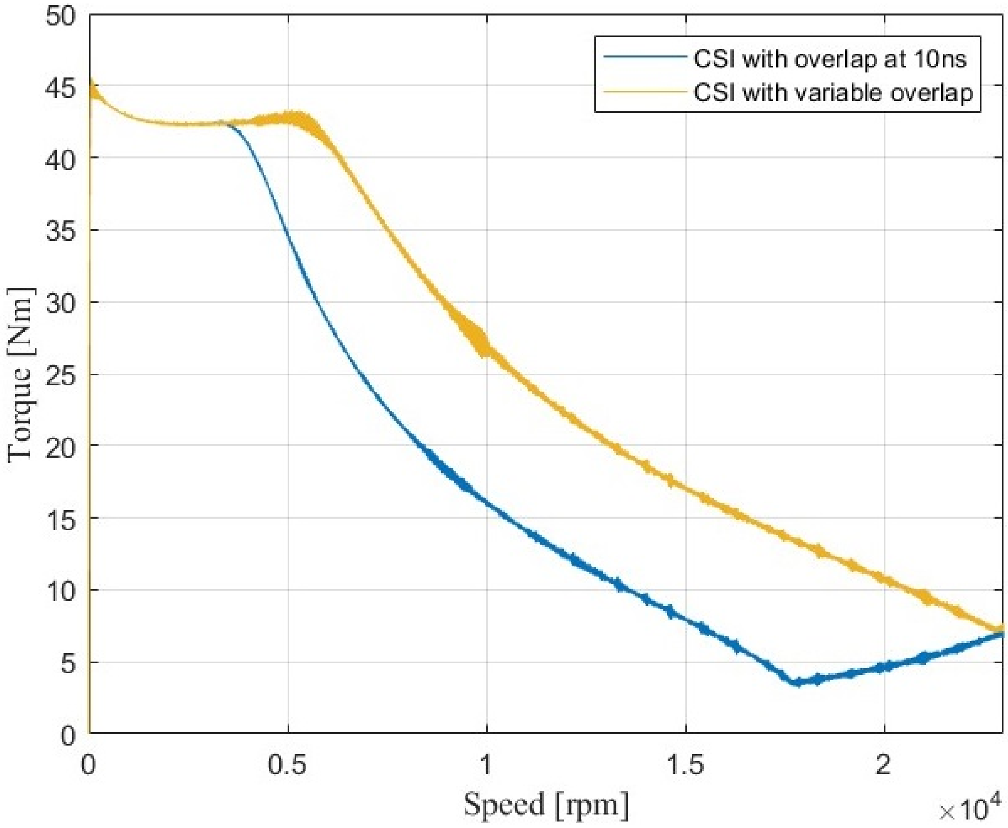

Figure 84: Motor electrical torque with CSI (with constant overlap and with controlled overlap).

5.3.3 SVM Technique

An alternated SVM modulation, similar to the one presented in [85] was chosen. The idea is the same as for the VSI SVM: the difference lies on the reference, that is a current vector. Main formulae, see (5.3) and (5.4), for the evaluation of the active vectors appliance times, were implemented in a C-script included in the PLECS model. Among the different modulation techniques, an asymmetrical one was employed instead of a symmetrical in order to reduce the switching losses.

$$\begin{cases} I_{ref} = \sqrt{I_\alpha^2 + I_\beta^2} \\ \tau_a = \frac{2}{\sqrt{3}} \cdot \frac{I_{ref}}{I_{DC}} \cdot \sin\left(\frac{\pi}{3} - \theta\right) \\ \tau_b = \frac{2}{\sqrt{3}} \cdot \frac{I_{ref}}{I_{DC}} \cdot \sin\theta \\ \tau_0 = 1 - \tau_a - \tau_b \end{cases} \tag{5.3}$$

$$\begin{cases} T_a = \tau_a \cdot T_{sw} \\ T_b = \tau_b \cdot T_{sw} \\ T_0 = \tau_0 \cdot T_{sw} \end{cases} \tag{5.4}$$

5.4 Performance Comparison

In terms of performance comparison, the power in the most significant point should be evaluated. In Fig. 85 a comparison between the torque-speed curves of the motor with VSI and CSI (with and without the overlap control) are reported. The power is evaluated in three significant points:

1. Base speed at nominal torque;
2. Final flux weakening speed for VSI (9000 rpm);
3. Final maximum speed reached (23000 rpm).

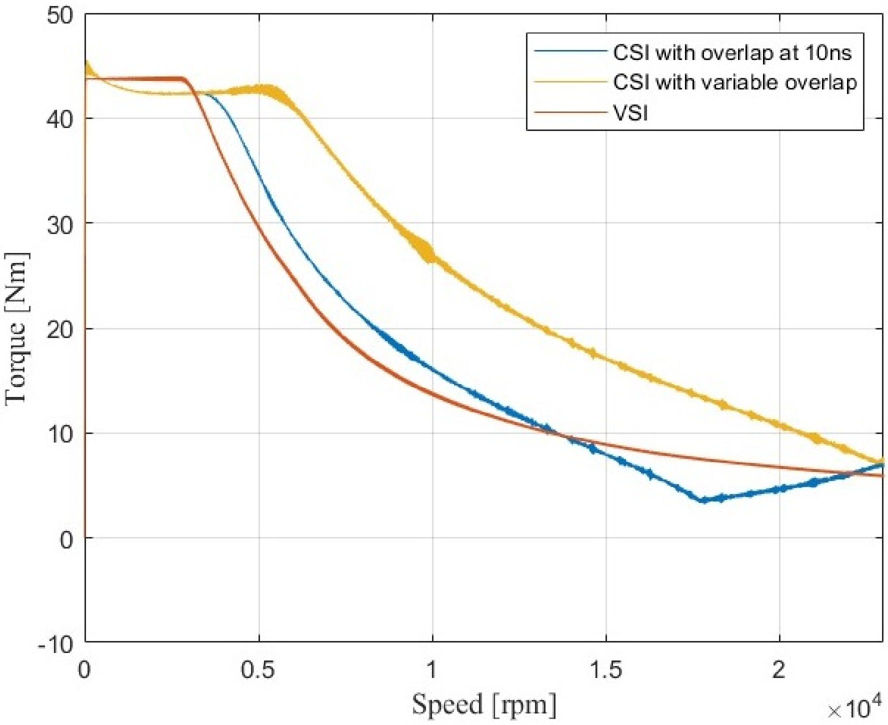

Figure 85: Motor electrical torque with VSI and with CSI with and without the overlap control.

Table 9: Power Comparison

Configuration	**Speed [rpm]**	**Torque [Nm]**	**Power [kW]**
VSI	3062	43.8	14
CSI with $OV = 10ns$	3420	42.4	15.2
CSI with controlled OV	5000	43.2	22.6
VSI	9000	15.2	14.3
CSI with $OV = 10ns$	9000	17.9	16.8
CSI with controlled OV	9000	29.2	27.5
VSI	23000	5.9	14.2
CSI with $OV = 10ns$	23000	6.7	16.1
CSI with controlled OV	23000	7.7	18.6

One of the main key performance indicator for an electric drive is the efficiency, therefore it is important to correctly compute both the motor and the inverter efficiency. Here, it must be specified that losses on L_{DC} for the CSI and on C_f for the VSI have not been taken into account. In the first subsection, the efficiency computation of the converter stage is explained and in the second one the power losses on the motor are compared.

5.4.1 Converter efficiency comparison

To compute the efficiency a PLECS feature is employed [86], in fact, the software allows computing the power losses of a switch, if a thermal model is defined. When creating a new thermal model in PLECS, conduction and switching losses need to be specified: both can be derived from the device datasheet. Conduction losses are easy to evaluate since it is sufficient to extrapolate points from the drain-source voltage- drain current curve $v_{DS} - i_D$. Switching losses, instead, are more complicated to compute: an efficient way is to derive a value of the switch-on and switch-off losses E_{on} and E_{off} for a specific value of the couple $(V_{block} - I_{load})$ and then upload the results in PLECS. In this study EPC2304 GaN FETs in parallel are employed. The analytical model was built from already existing one in literature: [87] and [88] constitute an example. However, these model were improved considering the variability of the reverse-transfer capacitance C_{rss} during the voltage transients and the non linear current rise during a channel modulation condition. EPC2304 and VS-100BGQ100 diode [89] were chosen for the comparison. For both architectures, the efficiency values were evaluated in three different condition: base speed ω_B, $9000rpm$ and highest speed reached $\omega_{max} = 23000$. The switching frequency chosen for both VSI and CSI was $f_{sw} = 60kHz$. Results are resumed in TABLE 10 for the CSI and in TABLE 11 for the VSI. When comparing the two architectures, TABLE 10 and 11, it appears that the CSI has lower efficiency and that is due to the diodes continuos conduction over time, however differences are very slight. Considering the possibility of avoiding the MTPV, the lower stress on the motor insulation and the lower $THD\%$ of the motor currents, CSI becomes very interesting for traction application. Moreover, consideration on the motor losses should also be made, to make the whole comparison.

Table 10: Efficiency of CSI with overlap control.

$f_{sw,pre} = f_{sw,CSI} = 60kHz$	**Input Power** $[W]$	**Power losses pre-stage** $[W]$	**Power losses CSI** $[W]$	**Efficiency** $[\%]$
Base speed $\omega_B = 5000\ rpm$	11937	320	675	91.70
Final FW speed $\omega = 9000\ rpm$	13733.8	88.04	176.4	98.04
Max speed $\omega_{max} = 23000\ rpm$	22286.8	115.9	256.7	98.33

Table 11: Efficiency of VSI.

$f_{sw} = 60kHz$	**Input Power** $[W]$	**Power losses VSI** $[W]$	**Efficiency** $[\%]$
Base speed $\omega_B = 3500\ rpm$	7570	545.73	92.83
Final FW speed $\omega = 9000\ rpm$	13906	251.52	98.2
Max speed $\omega_{max} = 23000\ rpm$	14420	234	98.39

5.4.2 Motor losses

From the motor efficiency point of view, one of the most critical point is to reduce the ripple of the current in input to the motor, because it leads to important drawbacks that can affect significantly the overall performance of the machine. The machine simulated with perfect sinusoidal stator currents (ideal condition reached with CSI) has a global efficiency of 88.3% at 23000 rpm, where considering a current ripple of about 4% of the main current component, so with an overall good sinusoidal shape of the currents, a reduction of the efficiency of the motor of 1% can be obtained. Nevertheless, the overall efficiency is not the only advantage;

the losses on the magnets strictly depends on the current ripple and they can be reduced by segmenting the magnet along the axial direction but this affects the K_e of the machine. By using a CSI these losses are highly reduced, leading to a minor risk of magnet demagnetization and overheating.

5.5 Conclusions

A new extended MTPA-FW control technique for a CSI is presented and compared with a more traditional VSI topology. The FW control for the CSI was implemented to obtain the maximum exploitation of the system for a typical constant power region profile; thanks to the CSI the base speed can be increased by modifying dynamically in the control loop the overlap time, in order to exploit the CSI intrinsic capability to boost in voltage, so a new control model is proposed. The extended speed above the base speed was obtained combining the intrinsic boosting capability of the CSI with a flux weakening control strategy. This combined control strategy allows to obtain high speed region without MTPV, which, on the other side, is mandatory with the traditional VSI topology when high speed values are desired, incrementing the complexity of the motor control.

The comparison was made considering a 13.8 kW liquid cooled IPM machine for light electric vehicle. In order to simplify the analysis, the magnetic saturation effect is not considered, so the inductance on d and q axis are kept constant. In the comparison also the pre-stage losses for the CSI are considered and the additional losses in the motor related to the current ripple for the VSI.

Thanks to the new extended MTPA-FW control mode of the CSI and its boost capability, the overall torque (and power) obtained is maximized in the entire speed range taken into account. Furthermore, the current given as an input to the motor have almost null ripple, so the PWM losses which generally affects the total output power are very low compared to the one traditionally obtained with the VSI topology. Even if the CSI converter is slightly less efficient compared to the VSI, the overall system efficiency, considering also the motor losses and performance, supports the proposed topology.

Conclusions

An innovative architecture of a CSI and modulation strategy are presented in Chapter 1 and Chapter 2.

A three-phase CSI, called CSI7, with innovative architecture and modulation strategy was modeled. The effectiveness of the proposed CSI7 topology and adopted SVM was compared against the traditional CSI solution by means of simulations and experiments. This topology introduces an additional power switch compared to the traditional CSI solution to significantly reduce conduction semiconductor power losses. This extra switch, S7, can be a simple Mosfet or IGBT (without reverse blocking capability) if the power factor operation is sufficiently close to unity. In the proposed SVM, the null output vector is achieved by engaging S7 while simultaneously disengaging the entire bridge: the increased commutation count is offset by the benefits gained. As a first test for the new topology, an application with fixed frequency operation of the fundamental current was chosen: it was used as grid connected inverter for photovoltaic applications. Specifically, the proposed CSI7 solution can:

- minimize the THD of the injected grid current;
- attenuate the excitation of the output CL filter of the CSI without the use of any passive or active damping solutions
- reduce the common mode voltage variations with respect to ground thus reducing the ground leakage current
- reduce the conduction power losses
- allow the commutations of S_1 to S_6 to happen under zero current (ZCS)

The experiments proved that the topology is feasible in wide power range String Converter applications, all the way down to single-module converter. It is however more versed to high power applications, as shown by the power losses analysis and measured efficiencies. In particular, the experimental results showed the improvements of the proposed solution in terms of injected current THD and conversion efficiency with respect to traditional CSI solution. The lower excitation of the common-mode resonant circuit caused by the parasitic capacitance of

PV panels with respect to traditional CSI solution was demonstrated. This implies that under the same operating conditions and as shown in the experiments, the CSI7 architecture and proposed SVM is characterized by a lower ground leakage current.

Chapter 3 presented a new algorithmic approach to compute the machine performance in MTPA, FW and MTPV for IPM synchronous machines. The proposed approach is applied to compute the current components in the $i_d - i_q$ reference frame for the MTPA, FW and MTPV, evaluating also the voltage limit ellipses, isotorque curves, and torque vs. speed characteristic. Moreover, the proposed algorithms are efficient and suited to a real-time implementation, being still quite reliable in case of magnetic saturation. More traditional methods are based on a linear model, that does not account for L_d and L_q variations with the working point of the machine. Hence, traditional method fails at high speed, and/or with magnetic saturation, on the other hand a direct analytical solutions would require the computation of partial derivatives of $L_d\left(I, \gamma\right)$ and $L_q\left(I, \gamma\right)$ with respect to the current phase angle, leading to complex and unfeasible real-time implementations. A method for MTPA, FW and MTPV is presented. This method is efficient and suited to a real-time implementation, being still quite reliable in case of magnetic saturation. The proposed method is based on the inductance maps of the machine obtained by 2-D Finite Element Analysis. Two different methods were adopted for the FEA simulations: a standard nonlinear magnetostatic method (Standard Method) and Frozen Permeability method (FP Method). The two solutions were assessed by a reference curve, obtained with a direct computation 2-D FEA via the Maxwell's stress tensor. MTPA curve obtained with the conventional linear model differs significantly from the reference curve, especially for high currents values. On the other hand, the trajectory obtained with the proposed algorithmic approaches more similar to the reference. In addition to that, a comparison of the accuracy of the Frozen Permeability method with respect to the Standard Method was made. Results prove the higher accuracy of the nonlinear model based on Frozen Permeability, especially in case of relevant currents and high saturation.

Finding the optimal control trajectories is fundamental. A wrong control can affect significantly the machine's performance, as shown in Chapter 4, where different IPM motor control strategies for light traction pure electric vehicles were analyzed. Two methods proposed in literature based on saturation of current regulators detection or on voltage saturation detection have been adopted. Their performance exploits good the potential of the IPM electrical machine in Flux Weakening during acceleration, but since they rely on an integral action some issues could arise in deceleration depending on the integral dynamic as observed during experimental tests. According to this, to overcome this issue two additional control strategies to optimize their performance during deceleration were introduced. The proposed control actions are "id-safe" and anti-wind up approach. The "id-safe" is a feed forward value which corrects the id current command according to motor speed and BUS voltage. The anti-wind up avoids the deep saturation of d-q current PI regulators allowing to fully exploit the available BUS voltage. The optimized methods have been validated by experimental tests with an IPM motor for light electric vehicle. Both methods have improved the motor performance, during transition from flux-weakening strategy to MTPA due to deceleration. The anti-wind up must be applied with great care in case of outer voltage control strategy.

In the end, the study made on CSI and the ones relating on optimal control for IPM machines were related in a final work, reported in Chapter 5, which presented a new extended MTPA-FW control technique for a CSI. The results of the proposed control technique implemented with CSI were compared with a more traditional VSI topology. The FW control for the CSI was implemented to obtain the maximum exploitation of the system for a typical constant power region profile; thanks to the CSI the base speed can be increased by modifying dynamically in the control loop the overlap time, in order to exploit the CSI intrinsic capability to boost in voltage, so a new control model is proposed. The extended speed above the base speed was obtained combining the intrinsic boosting capability of the CSI with a flux weakening control strategy. This combined control strategy allows to obtain high speed region without MTPV, which, on the other side, is mandatory with the traditional VSI topology when high speed values are desired, incrementing the complexity of the motor control.

The comparison was made considering a 13.8 kW liquid cooled IPM machine for light electric vehicle. In order to simplify the analysis, the magnetic saturation effect is not considered, so the inductance on d and q axis are kept constant. In the comparison also the pre-stage losses for the CSI are considered and the additional losses in the motor related to the current ripple for the VSI.

Thanks to the new extended MTPA-FW control mode of the CSI and its boost capability the benefits obtained are:

- A wide spee range is obtained without the implementation of a complex MTPV strategy.
- The overall torque (and power) obtained is maximized in the entire speed range taken into account.

- The current given as an input to the motor have almost null ripple, so the PWM losses which generally affects the total output power are very low compared to the one traditionally obtained with the VSI topology.
- The harmonic content in both voltages and currents is lower. This, in turn, decreases the dv/dt stress on the insulation systems, as well as reducing losses and torque ripple.

Even if the CSI converter is slightly less efficient compared to the VSI, the overall system efficiency, considering also the motor losses and performance, supports the proposed topology.

Bibliography

[1] R. A. Torres, H. Dai, W. Lee, T. M. Jahns, and B. Sarlioglu, «Development of current-source-inverter-based integrated motor drives using wide-bandgap power switches», in *2019 IEEE 15th Brazilian Power Electronics Conference and 5th IEEE Southern Power Electronics Conference (COBEP/SPEC)*, 2019, pp. 1–6. DOI: `10.1109/COBEP/SPEC44138.2019.9065675`.

[2] M. Mohr and F. Fuchs, «Comparison of three phase current source inverters and voltage source inverters linked with dc to dc boost converters for fuel cell generation systems», in *2005 European Conference on Power Electronics and Applications*, 2005, 10 pp.–P.10. DOI: `10.1109/EPE.2005.219458`.

[3] S. Woolaghan and N. Schofield, «Current source inverters for pm machine control», in *2009 IEEE International Electric Machines and Drives Conference*, 2009.

[4] G.-J. Su, L. Tang, and Z. Wu, «Extended constant-torque and constant-power speed range control of permanent magnet machine using a current source inverter», in *2009 IEEE Vehicle Power and Propulsion Conference*, 2009, pp. 109–115. DOI: `10.1109/VPPC.2009.5289863`.

[5] E. Lorenzani, F. Immovilli, C. Bianchini, and A. Bellini, «Performance analysis of a modified current source inverter for photovoltaic microinverter applications», in *IECON 2013 - 39th Annual Conference of the IEEE Industrial Electronics Society*, 2013, pp. 1809–1814. DOI: `10.1109/IECON.2013.6699406`.

[6] E. Lorenzani, F. Immovilli, G. Migliazza, M. Frigieri, C. Bianchini, and M. Davoli, «Csi7: A modified three-phase current-source inverter for modular photovoltaic applications», *IEEE Transactions on Industrial Electronics*, vol. 64, no. 7, pp. 5449–5459, 2017. DOI: `10.1109/TIE.2017.2674595`.

[7] B. Sahan, S. Araujo, C. Noding, and P. Zacharias, «Comparative evaluation of three-phase current source inverters for grid interfacing of distributed and renewable energy systems», *IEEE Trans. Power Electron.*, vol. 26, no. 8, pp. 2304–2318, Aug. 2011, ISSN: 0885-8993. DOI: `10.1109/TPEL.2010.2096827`.

[8] D. Meneses, O. Garcia, P. Alou, J. Oliver, R. Prieto, and J. Cobos, «Single-stage grid-connected forward microinverter with constant off-time boundary mode control», in *IEEE APEC 2012*, 2012, pp. 568–574. DOI: `10.1109/APEC.2012.6165876`.

[9] A. Ristow, M. Begovic, A. Pregelj, and A. Rohatgi, «Development of a methodology for improving photovoltaic inverter reliability», *IEEE Trans. Ind. Electron.*, vol. 55, no. 7, pp. 2581–2592, Jul. 2008, ISSN: 0278-0046. DOI: `10.1109/TIE.2008.924017`.

[10] N. Lekgamheng and Y. Kumsuwan, «Power analysis of single-phase grid-connected photovoltaic systems based on two-stage current source converters», in *IEEE ECTI-CON 2012*, 2012, pp. 1–4. DOI: `10.1109/ECTICon.2012.6254121`.

[11] A. Kavimandan and S. Das, «Control and protection strategy for a three-phase single-stage boost type grid-connected current source inverter for pv applications», in *2013 IEEE International Conference on Industrial Technology (ICIT)*, 2013, pp. 1722–1727. DOI: `10.1109/ICIT.2013.6505935`.

[12] B. Mirafzal, M. Saghaleini, and A. Kaviani, «An svpwm-based switching pattern for stand-alone and grid-connected three-phase single-stage boost inverters», *IEEE Trans. Power Electron.*, vol. 26, no. 4, pp. 1102–1111, Apr. 2011, ISSN: 0885-8993. DOI: `10.1109/TPEL.2010.2089806`.

[13] P. Dash and M. Kazerani, «Dynamic modeling and performance analysis of a grid-connected current-source inverter-based photovoltaic system», *IEEE Trans. Sustain. Energy*, vol. 2, no. 4, pp. 443–450, 2011, ISSN: 1949-3029. DOI: `10.1109/TSTE.2011.2149551`.

[14] S. Anand, S. Gundlapalli, and B. Fernandes, «Transformer-less grid feeding current source inverter for solar photovoltaic system», *IEEE Trans. Ind. Electron.*, vol. 61, no. 10, pp. 5334–5344, Oct. 2014, ISSN: 0278-0046. DOI: `10.1109/TIE.2014.2300038`.

[15] B. Sahan, A. Vergara, N. Henze, A. Engler, and P. Zacharias, «A single-stage pv module integrated converter based on a low-power current-source inverter», *IEEE Trans. Ind. Electron.*, vol. 55, no. 7, pp. 2602–2609, 2008, ISSN: 0278-0046. DOI: `10.1109/TIE.2008.924160`.

[16] F. Gao, P. C. Loh, F. Blaabjerg, and D. Vilathgamuwa, «Five-level current-source inverters with buck-boost and inductive-current balancing capabilities», *IEEE Trans. Ind. Electron.*, vol. 57, no. 8, pp. 2613–2622, Aug. 2010, ISSN: 0278-0046. DOI: `10.1109/TIE.2009.2030208`.

[17] P. Cossutta, M. Aguirre, A. Cao, S. Raffo, and M. Valla, «Single-stage fuel cell to grid interface with multilevel current-source inverters», *IEEE Trans. Ind. Electron.*, vol. 62, no. 8, pp. 5256–5264, Aug. 2015, ISSN: 0278-0046. DOI: `10.1109/TIE.2015.2434800`.

[18] M. Aguirre, L. Calvino, and M. Valla, «Multilevel current-source inverter with fpga control», *IEEE Trans. Ind. Electron.*, vol. 60, no. 1, pp. 3–10, Jan. 2013, ISSN: 0278-0046. DOI: `10.1109/TIE.2012.2185014`.

[19] A. Bendre, I. Wallace, J. Nord, and G. Venkataramanan, «A current source pwm inverter with actively commutated scrs», *IEEE Transactions on Power Electronics*, vol. 17, no. 4, pp. 461–468, Jul. 2002, ISSN: 0885-8993. DOI: `10.1109/TPEL.2002.800999`.

[20] X. Guo, D. Xu, and B. Wu, «Four-leg current source inverter with a new space vector modulation for common-mode voltage suppression», *IEEE Trans. Ind. Electron.*, vol. PP, no. 99, pp. 1–1, 2015, ISSN: 0278-0046. DOI: `10.1109/TIE.2015.2417127`.

[21] S. Anand, S. Gundlapalli, and B. Fernandes, «Transformer-less grid feeding current source inverter for solar photovoltaic system», *IEEE Trans. Ind. Electron.*, vol. 61, no. 10, pp. 5334–5344, Oct. 2014, ISSN: 0278-0046. DOI: `10.1109/TIE.2014.2300038`.

[22] E. Lorenzani, F. Immovilli, C. Bianchini, and A. Bellini, «Performance analysis of a modified current source inverter for photovoltaic microinverter applications», in *IEEE IECON 2013*, Nov. 2013, pp. 1809–1814. DOI: `10.1109/IECON.2013.6699406`.

[23] W. Wang, F. Gao, and S. Rui, «Operation and modulation of h7 current source inverter with hybrid sic and si semiconductor switches», in *IEEE ICPE-ECCE Asia)*, Jun. 2015, pp. 135–141. DOI: `10.1109/ICPE.2015.7167777`.

[24] M. Mohr and F. Fuchs, «Comparison of three phase current source inverters and voltage source inverters linked with dc to dc boost converters for fuel cell generation systems», in *EPE*, 2005, 10 pp.–P.10. DOI: `10.1109/EPE.2005.219458`.

[25] D. C. Pham, S. Huang, and K. Huang, «Modeling and simulation of current source inverters with space vector modulation», in *International Conference on Electrical Machines and Systems (ICEMS)*, 2010, pp. 320–325.

[26] J. Espinoza and G. Joos, «Current-source converter on-line pattern generator switching frequency minimization», *IEEE Trans. Ind. Electron.*, vol. 44, no. 2, pp. 198–206, 1997, ISSN: 0278-0046. DOI: `10.1109/41.564158`.

[27] T. Halkosaari and H. Tuusa, «Optimal vector modulation of a pwm current source converter according to minimal switching losses», in *IEEE 31st Annual Power Electronics Specialists Conference*, vol. 1, 2000, 127–132 vol.1. DOI: `10.1109/PESC.2000.878821`.

[28] D. Zmood and D. Holmes, «Improved voltage regulation for current-source inverters», *IEEE Trans. Ind. Appl.*, vol. 37, no. 4, pp. 1028–1036, 2001, ISSN: 0093-9994. DOI: `10.1109/28.936393`.

[29] A. Morsy, S. Ahmed, P. Enjeti, and A. Massoud, «An active damping technique for a current source inverter employing a virtual negative inductance», in *IEEE APEC 2015*, 2010, pp. 63–67. DOI: `10.1109/APEC.2010.5433694`.

[30] G. Buticchi, D. Barater, E. Lorenzani, and G. Franceschini, «Digital control of actual grid-connected converters for ground leakage current reduction in pv transformerless systems», *IEEE Trans. Ind. Informat.*, vol. 8, no. 3, pp. 563–572, Aug. 2012, ISSN: 1551-3203. DOI: `10.1109/TII.2012.2192284`.

[31] Z. Yang, F. Shang, I. P. Brown, and M. Krishnamurthy, «Comparative study of interior permanent magnet, induction, and switched reluctance motor drives for ev and hev applications», *IEEE Transactions on Transportation Electrification*, vol. 1, no. 3, pp. 245–254, 2015. DOI: `10.1109/TTE.2015.2470092`.

[32] G. Pellegrino, A. Vagati, P. Guglielmi, and B. Boazzo, «Performance comparison between surface-mounted and interior pm motor drives for electric vehicle application», *IEEE Transactions on Industrial Electronics*, vol. 59, no. 2, pp. 803–811, 2012. DOI: `10.1109/TIE.2011.2151825`.

[33] E. A. Grunditz and T. Thiringer, «Performance analysis of current bevs based on a comprehensive review of specifications», *IEEE Transactions on Transportation Electrification*, vol. 2, no. 3, pp. 270–289, 2016. DOI: `10.1109/TTE.2016.2571783`.

[34] B. Bilgin, P. Magne, P. Malysz, *et al.*, «Making the case for electrified transportation», *IEEE Transactions on Transportation Electrification*, vol. 1, no. 1, pp. 4–17, 2015. DOI: `10.1109/TTE.2015.2437338`.

[35] B. Sarlioglu and C. T. Morris, «More electric aircraft: Review, challenges, and opportunities for commercial transport aircraft», *IEEE Transactions on Transportation Electrification*, vol. 1, no. 1, pp. 54–64, 2015. DOI: `10.1109/TTE.2015.2426499`.

[36] G. Sulligoi, A. Vicenzutti, and R. Menis, «All-electric ship design: From electrical propulsion to integrated electrical and electronic power systems», *IEEE Transactions on Transportation Electrification*, vol. 2, no. 4, pp. 507–521, 2016. DOI: `10.1109/TTE.2016.2598078`.

[37] T. M. Jahns, G. B. Kliman, and T. W. Neumann, «Interior permanent-magnet synchronous motors for adjustable-speed drives», *IEEE Transactions on Industry Applications*, vol. IA-22, no. 4, pp. 738–747, 1986. DOI: `10.1109/TIA.1986.4504786`.

[38] S. Morimoto, Y. Takeda, T. Hirasa, and K. Taniguchi, «Expansion of operating limits for permanent magnet motor by current vector control considering inverter capacity», *IEEE Transactions on Industry Applications*, vol. 26, no. 5, pp. 866–871, 1990. DOI: `10.1109/28.60058`.

[39] N. Bianchi and T. M. Jahns, «Design, analysis, and control of interior pm synchronous machines», *IEEE Industry Applications Society*, 1 (Chapter 8), 2004.

[40] N. Bianchi, *Electrical Machine Analysis Using Finite Elements.* Taylor & Francis, 2005.

[41] B. Stumberger, G. Stumberger, D. Dolinar, A. Hamler, and M. Trlep, «Evaluation of saturation and cross-magnetization effects in interior permanent-magnet synchronous motor», *IEEE Transactions on Industry Applications*, vol. 39, no. 5, pp. 1264–1271, 2003. DOI: `10.1109/TIA.2003.816538`.

[42] P. Guglielmi, M. Pastorelli, and A. Vagati, «Cross-saturation effects in ipm motors and related impact on sensorless control», *IEEE Transactions on Industry Applications*, vol. 42, no. 6, pp. 1516–1522, 2006. DOI: `10.1109/TIA.2006.882646`.

[43] T. Miller, M. Popescu, C. Cossar, and M. McGilp, «Performance estimation of interior permanent-magnet brushless motors using the voltage-driven flux-mmf diagram», *IEEE Transactions on Magnetics*, vol. 42, no. 7, pp. 1867–1872, 2006. DOI: `10.1109/TMAG.2006.874512`.

[44] R. Bojoi, A. Cavagnino, M. Cossale, and S. Vaschetto, «Methodology for the ipm motor magnetic model computation based on finite element analysis», in *IECON 2014 - 40th Annual Conference of the IEEE Industrial Electronics Society*, 2014, pp. 722–728. DOI: `10.1109/IECON.2014.7048580`.

[45] S. Li, D. Han, and B. Sarlioglu, «Modeling of interior permanent magnet machine considering saturation, cross coupling, spatial harmonics, and temperature effects», *IEEE Transactions on Transportation Electrification*, vol. 3, no. 3, pp. 682–693, 2017. DOI: `10.1109/TTE.2017.2679212`.

[46] X. Chen, J. Wang, and A. Griffo, «A high-fidelity and computationally efficient electrothermally coupled model for interior permanent-magnet machines in electric vehicle traction applications», *IEEE Transactions on Transportation Electrification*, vol. 1, no. 4, pp. 336–347, 2015. DOI: `10.1109/TTE.2015.2478257`.

[47] X. Chen, J. Wang, B. Sen, P. Lazari, and T. Sun, «A high-fidelity and computationally efficient model for interior permanent-magnet machines considering the magnetic saturation, spatial harmonics, and iron loss effect», *IEEE Transactions on Industrial Electronics*, vol. 62, no. 7, pp. 4044–4055, 2015. DOI: `10.1109/TIE.2014.2388200`.

[48] Z. Li and H. Li, «Mtpa control of pmsm system considering saturation and cross-coupling», in *2012 15th International Conference on Electrical Machines and Systems (ICEMS)*, 2012, pp. 1–5.

[49] S. Li, B. Sarlioglu, S. Jurkovic, N. Patel, and P. Savagian, «Analysis of temperature effects on performance of interior permanent magnet machines», in *2016 IEEE Energy Conversion Congress and Exposition (ECCE)*, 2016, pp. 1–8. DOI: `10.1109/ECCE.2016.7855214`.

[50] A. Consoli, G. Scarcella, G. Scelba, S. Sindoni, and A. Testa, «Steady-state and transient analysis of maximum torque per ampere control for ipmsms», in *2008 IEEE Industry Applications Society Annual Meeting*, 2008, pp. 1–8. DOI: `10.1109/08IAS.2008.218`.

[51] C. Mademlis and V. Agelidis, «On considering magnetic saturation with maximum torque to current control in interior permanent magnet synchronous motor drives», in *2002 IEEE Power Engineering Society Winter Meeting. Conference Proceedings (Cat. No.02CH37309)*, vol. 2, 2002, 1234 vol.2-. DOI: `10.1109/PESW.2002.985209`.

[52] E. Armando, P. Guglielmi, G. Pellegrino, M. Pastorelli, and A. Vagati, «Accurate modeling and performance analysis of ipm-pmasr motors», *IEEE Transactions on Industry Applications*, vol. 45, no. 1, pp. 123–130, 2009. DOI: `10.1109/TIA.2008.2009493`.

[53] M. Hadžiselimović, G. Štumberger, B. Štumberger, and I. Zagradišnik, «Magnetically nonlinear dynamic model of synchronous motor with permanent magnets», *Journal of Magnetism and Magnetic Materials*, vol. 316, no. 2, e257–e260, 2007, ISSN: 0304-8853. DOI: `https://doi.org/10.1016/j.jmmm.2007.02.114`.

[54] N. Bianchi and S. Bolognani, «Magnetic models of saturated interior permanent magnet motors based on finite element analysis», in *Conference Record of 1998 IEEE Industry Applications Conference. Thirty-Third IAS Annual Meeting (Cat. No.98CH36242)*, vol. 1, 1998, 27–34 vol.1. DOI: `10.1109/IAS.1998.732255`.

[55] C. Lopez-Torres, G. Bacco, N. Bianchi, A. G. Espinosa, and L. Romeral, «A parallel analytical computation of synchronous reluctance machine», in *2018 XIII International Conference on Electrical Machines (ICEM)*, 2018, pp. 25–31. DOI: `10.1109/ICELMACH.2018.8507210`.

[56] K. D. Hoang and H. K. A. Aorith, «Online control of ipmsm drives for traction applications considering machine parameter and inverter nonlinearities», *IEEE Transactions on Transportation Electrification*, vol. 1, no. 4, pp. 312–325, 2015. DOI: `10.1109/TTE.2015.2477469`.

[57] Y. Yan, J. Zhu, H. Lu, Y. Guo, and S. Wang, «Study of a pmsm model incorporating structural and saturation saliencies», in *2005 International Conference on Power Electronics and Drives Systems*, vol. 1, 2005, pp. 575–580. DOI: `10.1109/PEDS.2005.1619752`.

[58] Y. Yan, J. Zhu, Y. Guo, and H. Lu, «Modeling and simulation of direct torque controlled pmsm drive system incorporating structural and saturation saliencies», in *Conference Record of the 2006 IEEE Industry Applications Conference Forty-First IAS Annual Meeting*, vol. 1, 2006, pp. 76–83. DOI: `10.1109/IAS.2006.256487`.

[59] Z. Li and H. Li, «Mtpa control of pmsm system considering saturation and cross-coupling», in *2012 15th International Conference on Electrical Machines and Systems (ICEMS)*, 2012, pp. 1–5.

[60] Z. Liu, G. Feng, and Y. Han, «Extended-kalman-filter-based magnet flux linkage and inductance estimation for pmsm considering magnetic saturation», in *2021 36th Youth Academic Annual Conference of Chinese Association of Automation (YAC)*, 2021, pp. 430–435. DOI: `10.1109/YAC53711.2021.9486499`.

[61] G. Park, G. Kim, and B.-G. Gu, «Sensorless pmsm drive inductance estimation based on a data-driven approach», *Electronics*, vol. 10, no. 7, 2021, ISSN: 2079-9292. DOI: `10.3390/electronics10070791`. [Online]. Available: `https://www.mdpi.com/2079-9292/10/7/791`.

[62] H. Wu, W. Zhao, G. Zhu, and M. Li, «Optimal design and control of a spoke-type ipm motor with asymmetric flux barriers to improve torque density», *Symmetry*, vol. 14, no. 9, 2022, ISSN: 2073-8994. DOI: `10.3390/sym14091788`. [Online]. Available: `https://www.mdpi.com/2073-8994/14/9/1788`.

[63] D. G. Dorrell, «On the use of the frozen permeability method for torque separation in synchronous machines invited oral poster», in *2016 International Conference of Asian Union of Magnetics Societies (ICAUMS)*, 2016, pp. 1–4. DOI: `10.1109/ICAUMS.2016.8479892`.

[64] J. Chen, J. Li, R. Qu, and M. Ge, «Magnet-frozen-permeability fea and dc-biased measurement for machine inductance: Application on a variable-flux pm machine», *IEEE Transactions on Industrial Electronics*, vol. 65, no. 6, pp. 4599–4607, 2018. DOI: `10.1109/TIE.2017.2772165`.

[65] J. Neumann, C. Hénaux, M. Fadel, D. Prieto, E. Fournier, and M. T. Yamdeu, «Improved dq model and analytical parameters determination of a permanent magnet assisted synchronous reluctance motor (pma-synrm) under saturation using frozen permeability method», in *2020 International Conference on Electrical Machines (ICEM)*, vol. 1, 2020, pp. 481–487. DOI: `10.1109/ICEM49940.2020.9270983`.

[66] D. Shuto, Y. Takahashi, and K. Fujiwara, «Frozen permeability method for magnetic field analysis of permanent magnet motors considering hysteretic property», *IEEE Transactions on Magnetics*, vol. 55, no. 6, pp. 1–4, 2019. DOI: `10.1109/TMAG.2019.2896956`.

[67] D. Shuto, Y. Takahashi, and K. Fujiwara, «Frozen permeability method for magnetic field analysis of permanent magnet motors considering hysteretic property», *IEEE Transactions on Magnetics*, vol. 55, no. 6, pp. 1–4, 2019. DOI: `10.1109/TMAG.2019.2896956`.

[68] D. Meeker, «Finite element method magnetic», *User's Manual*, 2018.

[69] A. Fratta, A. Vagati, and F. Villata, «Design criteria of an ipm machine suitable for field–weakened operation», *Proc. of International Conference on Electric Machines, ICEM*, pp. 1059–064, 1990.

[70] D. Lu and N. C. Kar, «A review of flux-weakening control in permanent magnet synchronous machines», in *2010 IEEE Vehicle Power and Propulsion Conference*, 2010, pp. 1–6. DOI: `10.1109/VPPC.2010.5728986`.

[71] S. Bolognani, S. Calligaro, R. Petrella, and F. Pogni, «Flux-weakening in ipm motor drives: Comparison of state-of-art algorithms and a novel proposal for controller design», in *Proceedings of the 2011 14th European Conference on Power Electronics and Applications*, 2011, pp. 1–11.

[72] A. Vagati, M. Pastorelli, and G. Franceschini, «High-performance control of synchronous reluctance motors», *IEEE Transactions on Industry Applications*, vol. 33, no. 4, pp. 983–991, 1997. DOI: `10.1109/28.605740`.

[73] T. M. Jahns, «Flux-weakening regime operation of an interior permanent-magnet synchronous motor drive», *IEEE Transactions on Industry Applications*, vol. IA-23, no. 4, pp. 681–689, 1987. DOI: `10.1109/TIA.1987.4504966`.

[74] N. Bianchi, S. Bolognani, and M. Zigliotto, «High-performance pm synchronous motor drive for an electrical scooter», *IEEE Transactions on Industry Applications*, vol. 37, no. 5, pp. 1348–1355, 2001. DOI: `10.1109/28.952510`.

[75] L. Sepulchre, M. Fadel, M. Pietrzak-David, and G. Porte, «Mtpv flux-weakening strategy for pmsm high speed drive», *IEEE Transactions on Industry Applications*, vol. 54, no. 6, pp. 6081–6089, 2018. DOI: `10.1109/TIA.2018.2856841`.

[76] R. Krishnan, «Control and operation of pm synchronous motor drives in the field-weakening region», in *Proceedings of IECON '93 - 19th Annual Conference of IEEE Industrial Electronics*, 1993, 745–750 vol.2. DOI: `10.1109/IECON.1993.338988`.

[77] S. Morimoto, Y. Takeda, T. Hirasa, and K. Taniguchi, «Expansion of operating limits for permanent magnet motor by current vector control considering inverter capacity», *IEEE Transactions on Industry Applications*, vol. 26, no. 5, pp. 866–871, 1990. DOI: `10.1109/28.60058`.

[78] S. Morimoto, Y. Tong, Y. Takeda, and T. Hirasa, «Loss minimization control of permanent magnet synchronous motor drives», *IEEE Transactions on Industrial Electronics*, vol. 41, no. 5, pp. 511–517, 1994. DOI: `10.1109/41.315269`.

[79] C. Bianchini, G. Bisceglie, A. Torreggiani, *et al.*, «Effects of the magnetic model of interior permanent magnet machine on mtpa, flux weakening and mtpv evaluation», *Machines*, vol. 11, no. 1, 2023, ISSN: 2075-1702. DOI: `10.3390/machines11010077`. [Online]. Available: `https://www.mdpi.com/2075-1702/11/1/77`.

[80] G. Migliazza, G. Buticchi, E. Carfagna, *et al.*, «Dc current control for a single-stage current source inverter in motor drive application», *IEEE Transactions on Power Electronics*, vol. 36, no. 3, pp. 3367–3376, 2021. DOI: `10.1109/TPEL.2020.3013301`.

[81] G. Migliazza, E. Carfagna, G. Buticchi, F. Immovilli, and E. Lorenzani, «Extended speed range control for a current source inverter variable speed drive», in *IECON 2021 – 47th Annual Conference of the IEEE Industrial Electronics Society*, 2021, pp. 1–6. DOI: `10.1109/IECON48115.2021.9589501`.

[82] D. Benatti, G. Migliazza, E. Carfagna, F. Immovilli, and E. Lorenzani, «Novel single-stage current source inverter: Extension to low-speed region in motor drive applications», *IEEE Transactions on Industrial Electronics*, pp. 1–11, 2023. DOI: `10.1109/TIE.2023.3335461`.

[83] Y. Zhang and Y. W. Li, «Investigation and suppression of harmonics interaction in high-power pwm current-source motor drives», *IEEE Transactions on Power Electronics*, vol. 30, no. 2, pp. 668–679, 2015. DOI: `10.1109/TPEL.2014.2310955`.

[84] Y. Xu, Z. Wang, Y. Shen, J. He, and G. Buticchi, «A csi-fed pmsm drive system with single-stage operation for extended constant-torque range», *IEEE Transactions on Industrial Electronics*, pp. 1–13, 2023. DOI: `10.1109/TIE.2023.3342297`.

[85] E. Lorenzani, F. Immovilli, C. Bianchini, and A. Bellini, «Extended speed range control for a current source inverter variable speed drive», in *IECON 2013 – 39th Annual Conference of the IEEE Industrial Electronics Society*, 2013, pp. 1809–1814.

[86] Plexim, *The simulation platform for power electronic systems - user manual version 4.8.1*, 2024.

[87] X. Li, J. Jiang, A. Q. Huang, *et al.*, «A sic power mosfet loss model suitable for high-frequency applications», *IEEE Transactions on Industrial Electronics*, vol. 64, no. 10, pp. 8268–8276, 2017. DOI: `10.1109/TIE.2017.2703910`.

[88] D. Christen and J. Biela, «Analytical switching loss modeling based on datasheet parameters for mosfets in a half-bridge», *IEEE Transactions on Power Electronics*, vol. 34, no. 4, pp. 3700–3710, 2019. DOI: `10.1109/TPEL.2018.2851068`.

[89] Vishay, «Vs-100bgq100 schottky rectifier, 100 a», Vishay, Tech. Rep., 2011.